NORTHWESTERN UNIVERSITY

Effect of Water on Thermoelasticity of Majoritic Garnet: Implications for the Seismic Structure at the Top of the Lower Mantle

A DISSERTATION

SUBMITTED TO THE GRADUATE SCHOOL
IN PARIAL FULLFILLMENT OF THE REQUIREMENTS

for the degree

DOCTOR OF PHILOSOPHY

Field of Earth and Planetary Sciences

By

John Daniel Lazarz

EVANSTON, ILLINOIS

June 2018

Abstract

Effect of Water on Thermoelasticity of Majoritic Garnet: Implications for the Seismic Structure at the Top of the Lower Mantle

John Daniel Lazarz

High-pressure and high-temperature laboratory experiments on the physical properties of mantle minerals provide a window into the Earth's interior chemistry and geodynamics. The measurement of material density, compressibility, and elasticity at high P-T conditions provides thermoelastic parameters necessary to model seismic velocities in the Earth's mantle at regional and global scales. In the first study, I determined the influence of hydration on thermoelasticity of majoritic garnet, an important silicate phase in the mantle transition zone (MTZ, 410-660 km depth). The MTZ is thought to potentially contain a large geochemical reservoir of H_2O, bound in the crystal structures of nominally anhydrous minerals as hydroxyl (OH^-) defects. My results show little or no effect of hydration on seismic velocities in or below the MTZ, suggesting that low-velocity anomalies recently observed below the transition zone beneath North America by Schmandt et al. (2014) and others are caused by dehydration melting of garnet as it transitions to bridgmanite at ~780 km depth. In the second study I perform a high-pressure synchrotron X-ray diffraction study of clinoenstatite ($Mg_2Si_2O_6$) up to 45 GPa to determine its structure and compressibility. From 9.5 to 35.5 GPa I observed the high-pressure clinoenstatite (HPCEN) phase and measured its P-V equation of state and structural evolution over an expanded pressure range relevant to pyroxene metatstability. At 45 GPa, I observed a phase transition to a new monoclinic form of $Mg_2Si_2O_6$, called HPCEN2. Observation of HPCEN2 in $Mg_2Si_2O_6$ is the third apex of the pyroxene quadrilateral to adopt this structure type at high-pressure, which has also been observed in $Fe_2Si_2O_6$ (Pakhomova et al. 2017) and in $MgCaSi_2O_6$ (Plonka et al., 2012;

Hu et al., 2016). In the third study I developed an optical microscope at Los Alamos National Laboratory to quantify the tensor of refractive indices (i.e. the indicatrix) in molecular crystals, and applied the new setup to determining the indicatrix and chromatic dispersion of acetaminophen (p-hydroxyacetanilide form I, commonly known as Tylenol®) as well as the orientation of the optical indicatrix in a monoclinic basis. Results indicate the optical indicatrix of acetaminophen form 1 is optically negative and biaxial. The results will ultimately be applied towards determining the full elastic tensor of acetaminophen from ongoing Brillouin spectroscopy experiments. Knowledge of the elastic tensor of molecular crystals such as acetaminophen will improve models of mixtures of pharmaceuticals with binders under compression, potentially reducing the amount of binder necessary to produce tablets (Anderson, 2008; Toms et al., 2008; Ong et al., 2010). Chapter 5 presents development of a 2-dimensional X-ray diffraction system in the Northwestern University High-Pressure Science Laboratory. Built onto an existing 4-circle Huber diffractometer, addition of the area detector system expands the capabilities of the instrument to include powder diffraction, rapid determination of crystal orientation matrices, and X-ray diffraction studies of minerals and materials at simultaneous high-pressure and temperature conditions.

Acknowledgements

I would like to express my sincere gratitude to my thesis advisors Steve Jacobsen, Craig Bina, and Brad Sageman. Thank you Steve, for giving me the chance to explore and learn. Thank you Craig, for your patience and expertise. Brad, thank you for your support and flexibility.

I would also like to thank my fellow graduate students Michelle Wenz and Hannah Bausch for their support, encouragement, and entertainment. Michelle, thank you for your camaraderie and boundless enthusiasm. Hannah, thank you for putting up with my ranting explanations and lengthy stories.

My endless thanks to past graduate students who have since graduated and embarked on their own journeys: Josh Townsend and Laurel Childress. Josh, your yearning for understanding and limitless drive serves as an inspiration and example for me every day. Thank you for the lifelong friendship and guidance. Laurel, thank you for fostering a wonderful environment and strong community.

Mr. Jonathan Lauff and Mrs. Emily Binder, thank you for teaching me the importance of goals and dedication. Your emphasis on the value of delayed gratification and importance of self-motivation taught me to be a better and more resilient person. Your seemingly endless patience and love for teaching taught me compassion and inspired my love of education.

I extend my eternal gratitude to my family and especially my parents Nancy Lazarz and John A. Lazarz for fostering my curiosity and supporting my dreams. Your passion for science and education inspired my career and taught me to value truth. Katie, thank you for always being a friend and ally.

Lastly, I would like to thank Courtney. Thank you for being by my side in both the sun and the rain. Your boundless support and dedication is appreciated beyond words.

Table of Contents

List of Figures

List of Tables

Chapter 1

Thesis Overview

1.1 Introduction

Understanding the evolution of planet Earth to its current state, unique and habitable, is a central goal of geophysical research. The ability to predict and understand the dynamic nature of Earth's outer most layer, the crust, is a relatively recent breakthrough in the development of plate tectonics theory in the 1960's, nearly half a century after quantum mechanics was established.The mechanics of Earth's dynamic system is ultimately controlled by material properties, which are in turn controlled by the atoms and bonds in those materials – back at the quantum scale. Humans realized early on that material properties play a dominant role in larger-scale characteristics. Metal was chosen over stone for its toughness and pliability, ceramics were chosen over wood for their thermal resilience and hardness. The material properties, at the atomic level, are what ultimately lead to these large-scale material characteristics and behaviors. The same material property relationship exists within planets. The mineralogical composition, and the material properties of the individual minerals which sum to the aggregate composition, lead to the bulk properties of the Earth. The study of geophysics is the pursuit of this relationship between material properties, structure, and evolution of the Earth. My thesis in mineral physics connects properties controlled at the atomic scale, to geophysical-scale observables.

Chapter 2 focuses on the impact of hydration on the elastic properties of majoritic garnets at high pressures and high temperatures. The results are used to interpret the anomalous seismic structure of the top of the lower mantle (660-800 km depth), where partial melting has been invoked to explain the cause of low-velocity anomalies. Garnets may compose up to ~35% of the overall composition at these depths and therefor play an important role in bulk properties of the mantle (e.g. Xu et al., 2008). Chapter 3 presents an investigation into the compression behavior of clinoenstatite ($Mg_2Si_2O_6$), another important upper-mantle mineral, and discovers a newly found structural transition at high-pressure (45 GPa). Observation of the new $Mg_2Si_2O_6$ phase completes the third apex of the pyroxene quadrilateral wherein the Ca-poor clinoenstatite end member is found, facilitating a broader view of clinopyroxene crystal chemistry at conditions relevant to metastability in the Earth's mantle along cold subduction geotherms. Chapter 4 broadens the horizons of this dissertation with an investigation into the optical properties of the molecular crystal acetaminophen (p-hydroxyacetanilide form I). The quantification of optical dispersion within acetaminophen is an essential step towards the complete understanding of the materials elastic tensor with relevance to pharmacology and energetic materials. The connection between minerals in rock and pharmaceutical crystals in tables derives from the need to model multi-phase aggregates under compression. The techniques developed and optimized in the work presented in Chapter 4 were integral to the completion of work performed in Chapter 2. The final chapter, Chapter 5, presents a developmental aspect of my thesis, wherein I added a two-dimensional area detector into the X-ray diffraction system in the mineral physics laboratory. This work involved both physical integration of mechanical systems as well as software control and implementation of mathematical mapping of the 2D system into the 3D geometry of the X-ray goniometer. The new instrumentation expands diffraction methods in the high-pressure science lab to include high-pressure and high-temperature powder X-ray diffraction as well as rapid determination of orientation matricies of single crystals for diffraction experiments using the point detector for equation of state work.

1.2 Chapter 2

In Chapter 2, entitled *Thermoelasticity of Hydrous Majoritic Garnet and Implications for Water at the Top of the Lower Mantle*, I present the thermal and elastic parameters of majoritic garnet up to 18 GPa and 300 °C. These results are used to interpret anomalous seismic structures between 660 km and 800 km depth, which have been reportedly caused by dehydration melting (Schmandt et al. 2014). Majoritic garnet is a primary component of the transition zone and has stability within the upper 200 km of the of the lower mantle where it is the only mineral with the potential to store large quantities of water, potentially up to ~2200 wt ppm H_2O (Thomas et al., 2015). I quantify the impact of hydration on majoritic garnet elasticity and assess the implications for negative velocity gradients at ~750 km depth beneath western North America, which have been previously attributed to the dehydration of rinwoodite (Schmandt et al. 2014). In this work, I show that the cause of the anomaly is more likely due to dehydration of majoritic garnet.

Garnets are characterized by the general formula $X_3^{VIII}Y_2^{VI}Si^{IV}{}_3O_{12}$, with several end member variants. The X site is most commonly occupied by divalent cations (Ca^{2+}, Fe^{2+}, Mg^{2+}, Mn^{2+}) and the Y site is the host for trivalent cations (Al^{3+}, Fe^{3+}, Cr^{3+}). Primary end members considered in this study include pyrope (Py, $Mg_3Al_2Si_3O_{12}$), almandine (Alm, $Fe_3Al_2Si_3O_{12}$), and grossular (Gr, $Ca_3Al_2Si_3O_{12}$), although several others exist. All garnets are either cubic or strongly pseudocubic. While inspecting the Coorara meteorite Smith and Mason (1970) found garnet with a silicon excess (greater than 3 atoms per formula unit). This garnet showed partial occupancy of the octahedral site (Y) by excess Si and Mg, this garnet solid solution was deemed majorite (Mj, $Mg_3(MgSi)Si_3O_{12} = Mg_4Si_4O_{12}$). Later, in 1985, Moore and Gurney found terrestrial majorite in kimberlitic diamonds. With increasing substitution into the octahedral site of Si and Mg the cubic structure distorts, due to ordering of Mg and Si on the octahedral sites, becoming progressively more tetragonal and is stable between 16 and 23 GPa at temperatures above 1600 °C (Angel et al., 1998; Wang et al., 1993; Ohtani et al., 1991; Kato and Kumazawa, 1985).

Beginning above 400 km depth, Ca-poor orthopyroxene ($(Mg,Fe)SiO_3$) and Ca-rich clinopyroxene ($Ca(Mg,Fe)Si_2O_6$) begin to dissolve into garnet, forming a majorite-garnet solid solution. As the transformation progresses silicon is incorporated into the octahedral site via a coupled substitution of tetravalent Si^{4+} and one divalent cation (M^{2+}) replacing two trivalent cations following the relationship: $2M^{3+} = Si^{4+} + M^{2+}$ (Ringwood, 1967; Ringwood and Major, 1971). The complete majoritic garnet chemical composition progressively changes with depth due to increased dissolution of pyroxene with increasing pressure, completing between 450 and 520 km depth, resulting in complex crystal chemistry (Irifune and Ringwood, 1993; Gasparik, 1989; Kanzaki, 1987; Akaogi and Akimoto et al., 1977). The increased dissolution of pyroxene into garnet to form garnet-majorite solid solution with increasing pressure also results in increased elastic moduli and seismic velocities (Jeanloz, 1981; Bina and Wood, 1984). The full crystal chemical formula for the solid solution majoritic garnet is $(Mg,Fe,Ca)_3\{[(Al,Cr)_2],[Si(Mg,Fe)]\}Si_3O_{12}$.

While majoritic garnets can incorporate many different cations into the cubic and octahedral sites as substitutions, they can also incorporate water though charge-coupled chemical substitutions. Garnets have also been shown to be able to incorporate H^+ into the structure as hydroxyl point groups through defect mechanisms. Hydration commonly occurs through the hydrogarnet substitution where SiO_4 is replaced by OH_4 on the tetrahedral site or via substitution of silicon by trivalent aluminum and a proton in the tetrahedral sites or vacancies in octahedral and dodecahedral sites (Mookherjee and Karato, 2010; McCammon et al., 2004; Katayama et al., 2003; Bolfan-Casanova et al., 2000; Rossman and Aines, 1991). Natural garnets have been shown to contain a maximum water content of several hundreds of wt ppm H_2O (Beran and

Libowitzky, 2006; Beran et al., 1993) while synthetic garnets have been reported to contain up to ~2200 wt ppm H_2O (Thomas et al., 2015; Katayama et al., 2003; Bolfan-Casanova et al., 2000).

The first direct evidence for water in the Earth's upper mantle was reported in 2014 when Pearson et al. found ~1.4 wt% H_2O dissolved in a ringwoodite diamond inclusion. Concurrently, Schmandt et al. (2014) observed large, regional-scale low-velocity anomalies at 700-800 km depth beneath western North America, attributing the observed negative velocity gradients to the release of water from ringwoodite as it transitions to the lower-mantle assemblage, a process known as dehydration melting.

Below 660 km depth, the primary mineralogical components include majoritic garnet, bridgmanite $(Mg,Fe)SiO_3$, and ferropericlase, $(Mg,Fe)O$, in proportions of about X, Y, and Z%, respectively. At 660 km depth, ringwoodite disproportionates into bridgmanite plus ferroepericlase while the garnet component gradually dissolves into Ca-perovskite, $CasiO_3$, and bridgmanite (Wood and Rubie, 1996). By 780 km depth all of the remaining garnet has broken down. The dehydration melting reported by Schmandt et al. (2014) was inferred from the observation of a negative shear wave velocity anomaly beginning at ~730 km depth and ending at ~750 km depth. In this chapter I propose an alternate explanation, wherein the negative shear velocity anomalies observed by Schmandt et al. (2014) are attributed to dehydration of majoritic garnet. Garnets is the only phase capable of having much H_2O between 660 km and 800 km depth and thus most likely acts as the major hydrogen sink at the top of the lower mantle. While the velocities of majoritic garnet are not impacted by hydration, as shown by the experimental measurements of this thesis, I propose the negative velocity anomalies at ~750 km depth are due to the dehydration melting of majortic garnet.

1.3 Chapter 3

In Chapter 3, entitled *High-Pressure Phase Transition of Clinoenstatite*, I present volumetric compression data for Ca-poor clinoenstatite (end-member $Mg_2Si_2O_6$) between 9.5 and 35.5 GPa, culminating in observation of a new phase transition at ~45 GPa, which may have relevance to metastable pyroxenes in the Earth's mantle. Pyroxenes, characterized by chains of corner-sharing SiO_4 tetrahedra extending along the crystallographic c-axis direction and interwoven with MO_6 octahedra, are described as either orthopyroxenes (opx), clinopyroxenes (cpx), or protopyroxenes (ppx). Two distinct octahedral sites exist, M1 and M2, where the M2 octahedra is slightly distorted. The octahedral basal plane triangle can point in either the +c or –c direction, referred to as +/- tilt. The opx or cpx classification is dictated by the stacking between layers with these different tilt directions. Ca-rich clinopyroxenes crystallize in *C2/c* space groups while Ca-poor clinopyroxenes crystalize in $P2_1/c$. All pyroxenes are described in relation to layers approximately parallel to (100) consisting of alternating tetrahedra and octahedra. Varying symmetries among pyroxenes result from different chain kink geometries or stacking sequences of the octahedral layers and tetrahedral chains. The two, S or O-rotated, variations of the Si tetrahedral chain are described by their relative rotation of the tetrahedra triangular face to the octahedra basal plane triangle. The triangular faces of the S-rotated chain are oriented in the same direction of the triangular octahedral basal plane while in the O-rotated chains the octahedral and tetrahedral triangular faces have opposite directions. This S or O configuration is controlled by the O3-O3-O3 bond angle. Low-pressure clinoenstatite (LPCEN) $MgSiO_3$ consists of alternating O-S-O Si tetrahedra chains and transforms at high pressure to high pressure clinoenstatite (HPCEN) consisting of O-O-O Si tetrahedra chain arrangements.

The pyroxene quadrilateral between M cations Mg, Fe, and Ca consists of end member minerals: enstatite (En, $Mg_2Si_2O_6$), ferrosilite (Fs, $Fe_2Si_2O_6$), diopside (Di, $MgCaSi_2O_6$), and hedenbergite (Hd, $CaFeSi_2O_6$) (Morimoto et al. 1989). The Ca-bearing members of the quadrilateral crystallize with monoclinic symmetry known as clinopyroxenes. The Ca-poor clinopyroxenes crystallize in the $P2_1/c$ space group. The compression behavior of clinopyroxenes has been well characterized up to approximately 25 GPa with much of the work focused on Ca-rich cpx (Irifune et al., 1989; Tribaudino et al., 2001; Li and Neuville, 2010). It has been shown that $P2_1/c$ clinopyroxenes reversibly transform to $C2/c$ upon increased pressure, temperature, and M2 site cation size (Arlt and Angel, 2000). The critical pressure for this transition is exceedingly compositionally dependent taking place at 6.5 GPa and 1.7 GPa for clinoenstatite and clinoferrosilite, respectively (Tribaudino et al., 2001). The strong compositional dependence of phase transitions in pyroxenes is motivation for a more complete understanding of compression mechanisms within the broad pyroxene family.

A second high-pressure phase *with* $P2_1/c$ symmetry has previously been observed in two pyroxenes including diopside ($CaMgSi_2O_6$) at ~50 GPa (Plonka et al. 2012, Hu et al. 2016) and clinoferrosilite ($FeSiO_3$) at 30-36 GPa (Pakhomova et al. 2017). Here we report a continuation of the trend with the observation of the high-pressure clinoenstatite $C2/c$ – $P2_1/c$ phase transition. We observe a phase transition to a new phase at ~45 GPa from the previously known HPCEN (space group $C2/c$) to the new HPCEN2 (space group $P2_1/c$) phase. The pressure-compositional dependence of the HPCEN to HPCEN2 transition has implications for understanding potential pyroxene metastability relative to majorite along cold subduction geotherms and may impact models of slab dynamics (Hogrefe et al., 1994).

1.4 Chapter 4

In Chapter 4, entitled *Optical Properties of Acetaminophen and Assessment of Structure-Property Effects of Impurities by Refractometry*, I measure the chromatic dispersion of acetaminophen or p-hydroxyacetanilide (PHA form I), also known as paracetamol, and determine the impact of synthetic impurity p-acetoxyacetanilide (PAA) on its optical properties. Determination of the optical properties of acetaminophen is the first major step to quantification of its complete elastic tensor, which will ultimately be used to model the compression behavior of acetaminophen mixed with various binders in the tablet manufacturing process.

Acetaminophen is among the most common and prototypical over-the-counter pharmaceuticals used worldwide as an effective analgesic and antipyretic (Anderson, 2008; Toms et al., 2008; Ong et al., 2010). While commonly available and used, little is known about the optical properties and elasticity of acetaminophen. Form I acetaminophen crystallizes with a structure displaying monoclinic ($P2_1/n$) symmetry. As a result, minimal symmetry constraints can be placed on the elastic tensor in order to reduce the number of unique components. The primary technique for the determination of the elastic tensor for materials such as acetaminophen, Brillouin spectroscopy, requires knowledge of the complete optical indicatrix, or second-rank tensor of principal refractive indices. The low symmetry, difficulty of synthesis, and fragility of acetaminophen has until now made it too difficult to fully determine the elastic and optical properties of acetaminophen form I. In this chapter I present the complete optical indicatrix as well as experimental methods for the measurement of the optical indicatrix for low symmetry crystals. I show that the optical technique used in this chapter has the potential for rapid screening of molecular crystals and detection of 100s of ppm quantities of impurities.

1.5 Chapter 5

In Chapter 5, entitled *Development of 2-D X-ray Diffraction Techniques for Rapid Single-Crystal Analysis*, I present the development and implementation of a 2-D X-ray diffraction system on the 4-circle Huber diffractometer. These new capabilities allow for rapid orientation of single crystals, 2-D X-ray diffraction, powder X-ray diffraction, and rapid sample screening.

Chapter 2

Thermoelasticity of Hydrous Majoritic Garnet and Implications for Water at the Top of the Lower Mantle

This chapter is being prepared for journal submission as:

Thermoelasticity of Hydrous Majoritic Garnet and Implications for Water at the Top of the Lower Mantle

John D. Lazarz[1], Michelle D. Wenz[1], Sergey N. Tkachev[2], Dongzhou Zhang[3], Craig R. Bina[1], and Steven D. Jacobsen[1]

[1]Department of Earth and Planetary Sciences, Northwestern University, Evanston, IL 60208, USA
[2]GSECARS University of Chicago, Advanced Photon Source, Argonne National Laboratory, Argonne, IL 60439, USA
[3]Hawaii Institute of Geophysics and Planetology, School of Ocean and Earth Science and Technology, University of Hawai'i at Manoa, Honolulu, HI 96822, USA

2.1 Abstract

Here we combine in-situ X-ray diffraction and Brillouin spectroscopy measurements to determine the elastic constants of majoritic garnet under high pressure and temperature conditions up to 20 GPa and 300 °C. Two mid-range majoritic compositions were studied, one having ~900 ppm H_2O and the other having ~200 ppm H_2O in order to assess the potential influence of hydration on the elastic properties. I found that hydration has little or no effect on the velocities of majoritic garnet at high P-T and may therefore represent the dominant sink for hydrogen below the transition zone. The negative shear velocity anomalies beneath western North America observed by Schmandt et al. (2014) may be explained by the dehydration melting of majoritic garnet as it dissolves into the Ca-perovskite and bridgmanite phase, which cannot contain water.

2.1 Introduction

2.1 Introduction

The Earth's mantle is composed of nominally anhydrous minerals such as olivine, pyroxene, garnet, and their high-pressure polymorphs. Many of these minerals, while nominally anhydrous, are capable of containing several weight % (wt%) water (Smyth et al., 1987; Kohlstedt et al., 1996; Bolfan-Casanova, 2005). Mid-ocean ridge basalts have long been known to contain 0.005-0.02 wt% water, evidence for small amounts of water in the Earth's upper mantle (Saal et al., 2002). The first direct evidence of large quantities of water deep in the Earth's mantle was discovered in 2014 when Pearson et al. found ~1.4 wt% H_2O dissolved in a ringwoodite diamond inclusion. The incorporation of water as hydrogen defects in nominally anhydrous minerals can have large impacts on the minerals thermoelastic parameters (Jacobsen et al., 2010; Mao et al., 2012, Fan et al., 2017), which may be responsible for anomalous velocities seen in seismic profiles (Sinogeikin and Bass, 2002; Pamato et al., 2016).

Basaltic magmas provide the only direct evidence of the mantle's bulk composition. In 1976 Ringwood devised a synthetic primitive mantle rock, which when melted yields a typical basaltic magma and leaves behind a residual refractory peridotite. The synthetic rock, known as pyrolite, is composed of one part basalt and 3 parts dunite. The mineralogy of pyrolite can be summarized as 57 wt% olivine, 17 wt% orthopyroxene, 12 wt% clinopyroxene, and 14% garnet (Ringwood, 1976). The Si- and Al-poor component of pyrolite is olivine. At 410 km depth olivine $(Mg,Fe)_2SiO_4$ undergoes a phase transition to the high-pressure polymorph wadsleyite causing a sharp seismic discontinuity. The 410 km discontinuity marks the top of the mantle transition zone (TZ). At 520 km depth wadsleyite undergoes a phase transition and transforms to ringwoodite, resulting in a weaker and sporadically observed discontinuity (Shearer, 1990). Ringwoodite finally breaks down to bridgmanite $(Mg,Fe)(Si,Al)O_3$ and ferropericlase $(Mg,Fe)O$

at 660 km resulting in another sharp seismic discontinuity and marking the bottom of the TZ. The Si- and Al-rich portion of the pyrolite model consists of orthopyroxene (opx), clinopyroxene (cpx), and garnet. Upon compression, opx and cpx begin to dissolve into garnet-producing majoritic garnet, $(Mg,Fe)_4Si_4O_{12}$, where Mg, Fe, and Si substitute onto the octahedral site normally occupied by Al. At 18 GPa, Ca-silicate perovskite ($CaSiO_3$) begins to exsolve from garnet. At 660 km depth, garnet begins to dissolve into bridgmanite $(Mg,Fe)SiO_3$.

Compositional models of the Earth's interior are iteratively developed through the comparison of mineral physics models and seismological reference models such as the Preliminary Reference Earth Model (PREM) and AK135 (Dziewonski and Anderson, 1981; Kennett et al., 1995). Seismic wave velocities are sensitive to the thermoelastic parameters of the minerals they travel though. In elastically isotropic materials, the average compressional, V_P, and shear, V_S, wave velocities can be computed from the adiabatic bulk modulus, K_S, shear modulus, G, and density according to:

$$V_P = \sqrt{\frac{K_S + (4/3)G}{\rho}} \quad [2.1]$$

$$V_S = \sqrt{\frac{G}{\rho}} \quad [2.2]$$

Determination of elastic properties for minerals relevant to the Earth's interior is therefore essential to the interpretation of seismological models.

Seismic studies has revealed localized regions of low velocity, or low velocity zones (LVZs) at depths between 730 km and 800 km (Schmandt et al., 2014; Liu et al., 2016; Zhang et al., 2018; Liu et al., 2018). Two primary explanations for the low velocities observed in these regions have been posed 1) melting caused by the dehydration of hydrous material transported from the transition zone and 2) partial melt produced by the dehydration of metallic iron

(Schmandt et al., 2014; Liu et al., 2016). We investigate a third potential explanation in which the reduction in velocity is caused by locally hydrous garnet at the top of the lower mantle.

Within the mantle, the hydration of garnet will have the strongest impact on seismic velocities at depths where water will be partitioned into the garnet as opposed to nominally anhydrous phases such as olivine. Water-storage capacity of the primary mineral phases in the lower mantle, bridgmanite and ferropericlase, have been determined to be ~100 wt ppm H_2O (Bolfan-Casanova, 2005; Panero et al., 2015). Precise determination of water-storage capacities for lower mantle minerals is ongoing, however, studies suggest garnet can store a minimum of several hundred ppm H_2O by weight (Katayama et al., 2003; Bolfan-Casanova et al., 2005). Significant amount of water transported below the transition zone in the garnet phase would therefore not partition into bridgmanite or ferropericlase. From this, we draw two primary conclusions. Firstly, garnet is most likely to be hydrous below the transition zone at the top of the lower mantle. The impact of water on garnet elastic parameters would then have the largest impact between 660 km and 800 km depth. Secondly, the decomposition of garnet at the top of the lower mantle could cause a large release of water there, triggering dehydration melting and resulting in LVZs. The observation of LVZs at the depths where we expect dehydration melting, due to the dehydration of garnet, is motivation for this study.

2.2 Experimental Methods

2.2.1 Sample preparation

Synthesis of majoritic garnet single crystals used in this study was described previously (Thomas et al. 2015). In summary, single-crystal samples were synthesized with and without water at 18 GPa and 1800 °C in a rotating multi-anvil press. Pure oxide mixtures of MgO, FeO,

SiO_2, Al_2O_3, and Cr_2O_3 were loaded into iron-doped platinum capsules and sealed by cold welding. Before sealing the hydrous sample run (MA384) 0.5 μL bidistilled H_2O was added. Trace amounts of water were not removed from run MA382 before sealing. Isotropic single-crystals were selected from each MA384 and MA382 run for analysis. Final chemical compositions were determined by Thomas et al. (2015) using microprobe analysis. Measurement of H in both samples was performed using secondary-ion mass spectroscopy (SIMS). Sample compositions and water content are listed Table 2.1, as well as two published compositions for comparison.

Table 2.1: Sample compositions and water content.

Sample	Composition	Mineral Formula	H_2O (wt ppm)	Source
MA384	$Py_{76}Alm_{18}Mj_6$	$(Mg_{2.5}Fe^{2+}{}_{0.59})(Si_{0.06}Al_{1.76}Cr_{0.08}Fe^{3+}{}_{0.02})[SiO_4]_3$	881(62)	This Study
MA382	$Py_{54}Alm_{38}Mj_8$	$(Mg_{1.80}Fe^{2+}{}_{1.27})(Si_{0.08}Al_{1.62}Cr_{0.2}Fe^{3+}{}_{0.03})[SiO_4]_3$	241(125)	This Study
pamato_mj	$Py_{76}Mj_{24}$	$Mg_{3.24}Al_{1.53}Si_{3.23}O_{12}$	20	Pamato et al. (2016)
pamato_fe-mj	$Py_{78}Alm_6Mj_{16}$	$Mg_{3.01}Fe_{0.17}Al_{1.68}Si_{3.15}O_{12}$	-	Pamato et al. (2016)

2.2.2 High-pressure X-ray diffraction

Initial X-ray measurements were used to select high-quality majoritic garnet single-crystals for further analysis using single-crystal X-ray diffraction on a custom-built Huber four-circle diffractometer with sealed-tube Mo Kα radiation and a crystal-detector distance of ~40 cm. Samples selected from run MA384 and MA382 run products were mounted on glass fibers. A total of 28 reflections were centered for each single-crystal sample using the method of 8-position centering (King and Finger, 1979), where each unique *hkl* is centered with rocking curves (ω scans) in four equivalent positions, both in positive 2θ and negative 2θ positions, resulting in eight rocking curves for each *hkl*. Rocking curves were fit to pseudo-Voigt functions of Kα_1 and Kα_2 as a function of 2θ using the program Single (Angel and Finger, 2011). High intensity reflections and sharp peak profiles (~0.06°) were used as signs of acceptable crystal quality.

In situ (high-pressure) single-crystal X-ray diffraction (XRD) experiments were carried out at GSECARS, Sector 13 experimental station 13BM-C of the Advanced Photon Source (APS), Argonne National Laboratory (ANL). Diamond anvil cell (DAC) XRD measurements spanned the pressure range 0.0 to 28 GPa. A rhenium metal gasket with initial thickness of 250 μm was pre-indented to ~40 μm using 300 μm culet diamond anvils. Two 30 μm diameter single crystals were loaded into the sample chamber along with two ruby spheres. Differential stresses within the sample chamber were minimized by loading neon as a pressure medium using the GSECARS/COMPRES gas loading system (Rivers et al. 2008). Pressure was determined using the ruby fluorescence method (Mao et al. 1986). Data collections were performed with an access angle of 75°, two detector positions 0° and 20° 2θ, an X-ray wavelength of 0.434 Å, 15x15 μm X-ray spot, and 1 second exposure time on a Rayonix MAR 165 CCD. Diffraction images were analyzed using GSE_ADA and RSV software packages (Dera, 2007).

High-pressure and high-temperature experiments were performed at a combination of GSECARS, Sector 13 experimental station 13BM-C and 13BM-D. In both cases, BX-90 cells were resistively heated to a maximum of 500 °C using a platinum resistive heater. Data collections were performed with access angles of ~75°. Collections performed at 13BM-C used an X-ray wavelength of 0.434 Å and at 13BM-D 0.3344 Å. Exposures were collected as wide scans covering the entire access angle with exposure times of 1 s per degree. Diffraction images were integrated in Dioptas and analyzed using GSAS-II (Prescher et al., 2015; Toby et al., 2013).

2.2.3 Pressure determination

One of the largest contributors to uncertainty in high-pressure diamond anvil cell experiments is the measurement of pressure inside of the DAC. Two primary methods are used for determining pressure, the use of an internal diffraction standard and fluorescence measurements. Internal diffraction standards such as platinum or quartz can be used in conditions where ample room is available within the DAC, X-ray diffraction is available, diffraction patterns have minimal overlap with the sample, and a well known equation of state with which to convert measured unit-cell volumes to pressures is known for the given experimental conditions (i.e. temperature) (Angel et al. 1997; Dewaele et al. 2008). When possible, internal diffraction standards provide a method for high-precision pressure determination with pressure uncertainties as low as 0.009 GPa at 9 GPa (Angel et al. 1997).

The most common pressure determination technique is to measure the pressure dependent fluorescence shift for optical pressure gauges such as ruby (Cr^{3+} doped α-Al_2O_3). The characteristic ruby fluorescence signal consists of a doublet with two bands centered at 694.2 nm and 692.8 nm, R_1 line and R_2 line respectively, at 1 bar. The ruby doublet can be fitted to the sum of Gaussian and Lorentzian curves (Munro et al. 1985). As pressure is increased the doublet shifts towards higher wavelength (Piermarini et al. 1975, Mao et al. 1986). The relationship between the R_1 wavelength shift and pressure has been well described by Mao et al. (1986):

$$P = A/B\,\{[1 + (\Delta\lambda/\lambda_o)]^B - 1\} \qquad [2.3]$$

where *P* is pressure in megabars, λ is wavelength of the R_1 line, A = 19.04, and B = 7.665 for most common pressure medium such as Neon or Argon but 10.32(7) for soft pressure medium such as helium (Jacobsen et al. 2008).

The use of an optical pressure gauge is advantageous due to the minimal space requirements of a few microns, often-negligible X-ray diffraction contribution, speed, and offline (no X-rays) use. Uncertainties in pressure determined from ruby fluorescence are often ~0.01 GPa. Special care must be taken when ruby is used as a pressure calibrant due to its temperature sensitivity where a 5-6 °C temperature shift gives the same shift as a 0.1 GPa pressure change (Wood et al. 1980, Vos and Schouten et al. 1991). The temperature sensitivity of ruby does not, however, completely negate the effectiveness of ruby at moderate temperatures. When precise temperature is known the contribution to shift in wavelength due to temperature can be accounted for and corrected (Vos and Schouten et al. 1991). The R_1 and R_2 peaks begin to merge as temperature increases causing the R_1 peak to become unfittable beyond ~400 °C , marking the maximum temperature for which ruby fluorescence can effectively be used to determine pressure.

2.2.4 High-pressure high-temperature Brillouin spectroscopy

Brillouin spectroscopy is a technique used for the determination of a material's full elastic tensor, a requirement for the calculation of bulk elastic properties. The energy shift resulting from Brillouin scattering is due to the energy exchange between interacting photons and phonons when photons inelastically scatter from the excitation or destruction of acoustic phonons in a material. Given a known input photon energy, the measured energy difference between the elastically and inelasticly scattered photons can be related to the energy of the involved phonons and therefore interatomic potentials of the material (Polian, 2003).

The relationship between the energy shift of photons and energy of interacting phonons holds because energy and momentum are conserved. This conservation can be described with the relations:

$$\hbar\Omega = \pm\hbar(\omega_i - \omega_s) \qquad [2.4]$$

$$\vec{q} = \pm(\overrightarrow{k_\iota} - \overrightarrow{k_s}) \qquad [2.5]$$

where ω_i, ω_s, and k_i, and k_s are incident and scattered light wavenumbers and wavevectors respectively. While the phonon wavenumber and wavevector are Ω and q, respectively. Equation 2.4 is the result of the application of the conservation of energy to the system of the incident photon, the scattered photon, and the interacting phonon. The application of the conservation of momentum to the system results in Equation 2.5, a simple expression summarizing that the phonon wavevector is a linear combination of the incident and scattered wavevectors.

Several Brillouin scattering experimental geometries exist for which the wavevector is easily defined: 90° scattering ($q = [2^{1/2}n]/\lambda$), backscattering ($q = 2n/\lambda$), and platelet geometry ($q = [2\sin(\theta/2)]/\lambda$). For high-pressure experiments the most convenient geometry is platelet geometry (Figure 2.1). In platelet geometry the wavevector is defined by the internal scattering angle and incident photon wavelength.

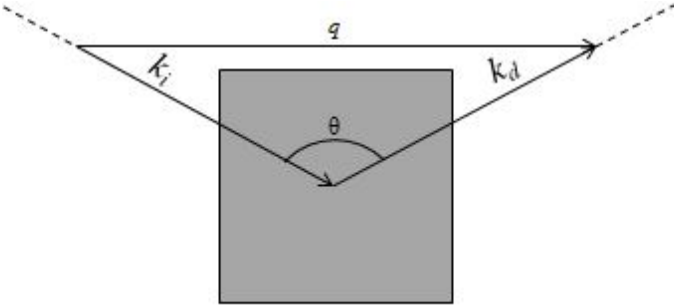

Figure 2.1: The most common Brillouin spectroscopy geometries are: 90 degree scattering where $q = [2^{1/2}n]/\lambda$, backscattering where $q = 2n/\lambda$, and platelet geometry where $q = [2\sin(\theta/2)]/\lambda$. Platelet geometry (above) is convenient for high pressure experiments because the index of refraction, n, does not need to be known. In all geometries, incident wavelength, λ, must be known. (Speziale et al., 2014)

The velocity, V, of the acoustic waves can then be measured using Equation 2.6.

$$V = \frac{\Omega}{q} \qquad [2.6]$$

Using Equation 2.6, it is possible to determine the sound velocity through a material.

Single crystals with diameters of ~75 μm were selected for the Brillouin measurements. Samples were prepared by double polishing to ~18-20 μm thickness with an optically perfect finish. Rhenium gaskets with initial starting thickness of 250 μm were pre-compressed to ~35 μm. The samples were loaded into BX-90 diamond anvil cells equipped with 400 μm diameter culet diamonds and a platinum resistive heater. The assembled cells were loaded with neon as a quasi-hydrostatic pressure medium using the GSECARS/COMPRES gas loading system (Rivers et al. 2008). Pressure was determined using a combination of the ruby fluorescence method (Mao et al. 1986) and a platinum equation of state (Dewaele et al., 2008). Brillouin spectroscopy measurements were performed at GSECARS 13BM-D using a 532 nm laser and six-pass

Sandercock-type piezoelectrically scanning tandem Fabry-Pérot interferometer TFP-1 in the platelet geometry with a scattering angle of 50 ° (Sinogeikin et al., 2006). When available, *in situ* X-ray measurements were taken using 0.3344 Å X-rays. Data collections were performed with access angles of ~75°. Exposures were collected as wide scans covering the entire access angle with exposure times of 1 second/degree. Diffraction images were integrated in Dioptas and analyzed using GSAS-II (Prescher et al., 2015; Toby et al., 2013).

2.3 Results and Discussion

2.3.1 P-V Equation of State

Single-crystal X-ray diffraction experiments performed between 0 and 27 GPa show a continuous stable cubic phase within the pressure range for both MA384 and MA382 compositions. The cubic phase was observed at 14 pressure points for each sample and successfully indexed using the cubic Ia-3d space group. Progression of the unit cell parameters with pressure can be found in Table 2.2.

The measured volumes of MA384 and MA382 (Table 2) were fitted to a third-order Birch-Murnaghan (BM3) equation of state. Both MA384 and MA382 reference volumes (V_0) were refined during the least-squares fitting procedure. Fitting was performed using the Burnman Python library (Cottaar et al. 2014). The BM3 equation of state fitted to the more hydrous of the two samples, MA384, data set has parameters V_0 = 1513.4(7) Å^3, K_{T0} = 164(4) GPa, and K_{T0}’ = 5.9(4). While the BM3 equation of state fitted to MA382 has parameters V_0 = 1512.9(7) Å^3, K_{T0} = 164(3) GPa, and K_{T0}’ = 5.6(3). The optimized-fits are shown in Figure 2.2.

Table 2.2-1: Majorite garnet sample MA384 P-V-T data. The sample maintains *Ia-3d* space group symmetry throughout the compression range.

MA384 (*Ia-3d*)

P (GPa)	T (K)	a (Å)	V (Å^3)
0.0001	298	11.4824(2)	1513.92(5)
1.21(6)	298	11.4531(2)	1502.34(5)
3.9(2)	298	11.3958(2)	1479.91(5)
5.6(3)	298	11.3608(3)	1466.31(6)
7.7(4)	298	11.3203(2)	1450.68(5)
9.6(5)	298	11.2945(2)	1440.78(5)
11.6(6)	298	11.2558(2)	1426.03(5)
15.3(8)	298	11.2021(2)	1405.71(5)
17.1(9)	298	11.1715(2)	1394.25(5)
19.0(9)	298	11.1458(3)	1384.63(6)
22(1)	298	11.1092(3)	1371.05(6)
23(1)	298	11.0859(3)	1362.43(6)
26(1)	298	11.0559(4)	1351.38(8)
28(1)	298	11.0316(3)	1342.51(7)
0.54(6)	423	11.483(5)	1514(2)
2.1(2)	423	11.451(5)	1501(2)
3.6(3)	423	11.411(5)	1485(2)
3.8(3)	423	11.405(5)	1483(2)
4.9(4)	423	11.391(5)	1478(2)
6.4(4)	423	11.355(5)	1464(2)
8.5(4)	423	11.327(5)	1453(2)
10.2(5)	423	11.295(5)	1440(2)
12.2(4)	423	11.258(5)	1426(2)
14.6(5)	423	11.219(5)	1412(2)
16.5(8)	423	11.183(5)	1398(2)
1.17(8)	573	11.485(5)	1514(2)
2.4(3)	573	11.454(5)	1502(2)
3.9(3)	573	11.423(5)	1490(2)
4.7(4)	573	11.393(5)	1478(2)
6.4(4)	573	11.361(5)	1466(2)
7.9(4)	573	11.350(5)	1462(2)
10.9(9)	573	11.287(5)	1437(2)
13.5(6)	573	11.253(5)	1424(2)
14.5(5)	573	11.232(5)	1417(2)
16.2(8)	573	11.210(5)	1408(2)

Table 2.2-2: Majorite garnet sample MA382 P-V-T data. The sample maintains *Ia-3d* space group symmetry throughout the compression range.

MA382 (*Ia-3d*)

P (GPa)	T (K)	a (Å)	V (Å^3)
0.0001	298	11.4796(3)	1512.8(7)
1.21(6)	298	11.4524(3)	1502.05(6)
3.9(2)	298	11.3951(3)	1479.65(7)
5.6(3)	298	11.3596(3)	1465.86(6)
7.7(4)	298	11.3184(3)	1449.94(6)
9.6(5)	298	11.2894(3)	1438.85(6)
11.6(6)	298	11.2516(3)	1424.42(6)
15.3(8)	298	11.1968(3)	1403.72(6)
17.1(9)	298	11.1664(3)	1392.34(6)
19.0(9)	298	11.1400(3)	1382.47(5)
22(1)	298	11.1027(3)	1368.64(5)
23(1)	298	11.0772(3)	1359.24(6)
26(1)	298	11.0495(3)	1349.05(7)
28(1)	298	11.0232(3)	1339.45(8)
8.95	423	11.305(5)	1444(2)
0.54	423	11.484(5)	1514(2)
2.12	423	11.439(5)	1496(2)
3.62	423	11.415(5)	1487(2)
4.89	423	11.387(5)	1476(2)
7.3	423	11.347(5)	1460(2)
6.105	423	11.355(5)	1464(2)
3.97	423	11.402(5)	1482(2)
16.36	423	11.185(5)	1399(2)
1.17	573	11.471(5)	1509(2)
2.39	573	11.456(5)	1503(2)
3.94	573	11.417(5)	1488(2)
4.95	573	11.401(5)	1481(2)
7.95	573	11.337(5)	1457(2)
4.54	573	11.405(5)	1483(2)
6.23	573	11.374(5)	1471(2)
8.29	573	11.329(5)	1453(2)
12.71	573	11.253(5)	1425(2)
17.16	573	11.188(5)	1400(2)

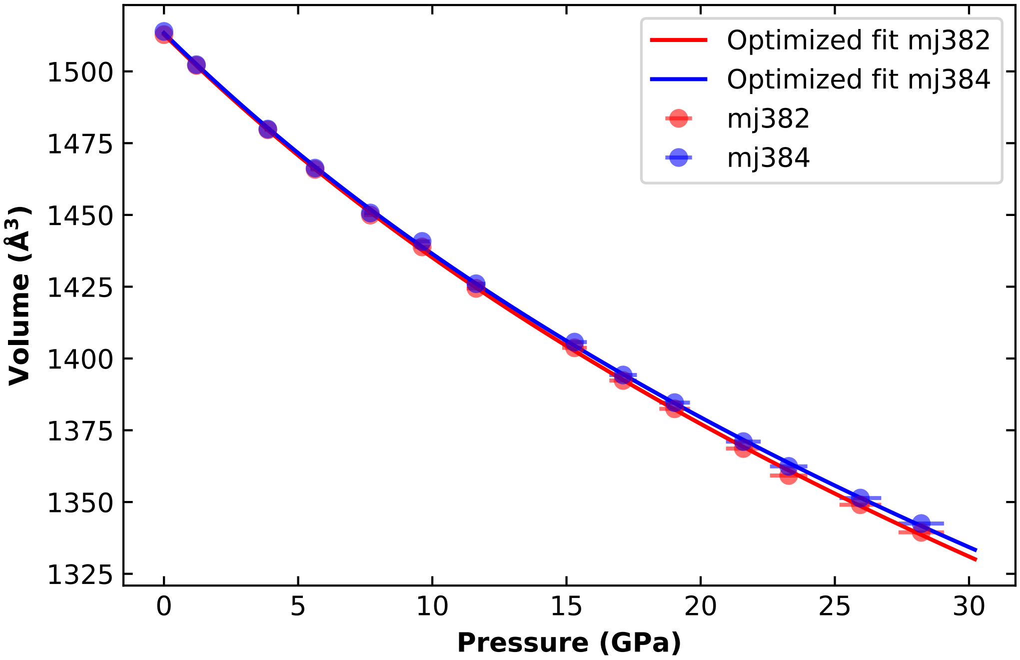

Figure 2.2: Comparison of variation in unit-cell volume as a function of pressure in majoritic garnet hydrous sample MA384 and relatively anhydrous sample MA382. Volumes are fit to a third-order Birch-Murnaghan equation of state (optimized fit).

The normalized stress, $F_E = P/3f_E(1+2f_E)^{5/2}$ and Eulerian finite strain, $f_E = [(V_0/V)^{2/3} - 1]/2$, are plotted in Figure 3, showing a positive linear inclination. As a result we selected the third-order truncation of the Birch-Murnaghan EoS. When K_{T0} and K_{T0}' are calculated from the intercepts and slopes of the F_E- f_E plots we obtain K_{T0} = 162(1) GPA and K_{T0}' = 5.1(8) for MA384 and K_{T0} = 164(1) GPA and K_{T0}' = 4.77(8) for MA382 which are both in good agreement with our optimized parameters. Uncertainties in our optimized equation of state parameters can be visualized using confidence ellipse plots (Figure 2.4). The elongated ellipses with a negative slope convey the negative correlation between the K_{T0} and K_{T0}' parameters. The first derivative of the bulk modulus, K_{T0}', shows a positive correlation with initial volume, V_0. Within uncertainty, the optimized equations of state for both samples MA384 and MA382 are identical. A comparison of normalized lattice parameters further emphasizes the similarity in elastic parameters K_{T0} and K_{T0}' between the two samples (Figure 2.5). This result is relatively unsurprising as reported elastic parameters for majorite-pyrope end member garnets tend to not vary widely outside of uncertainty, as a function of composition, as seen in Table 2.3.

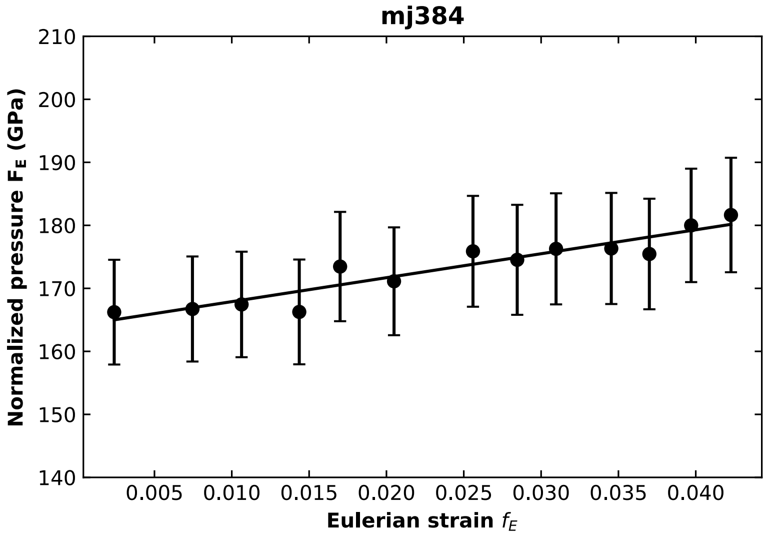

Figure 2.3: Normalized stress $F_E = P/3f_E(1+2f_E)^{5/2}$, vs. Eulerian finite strain, $f_E = [(V_0/V)^{2/3} - 1]/2$, plot shows a positive slope indicating a third-order Birch-Murnaghan equation of state should be used to fit the data.

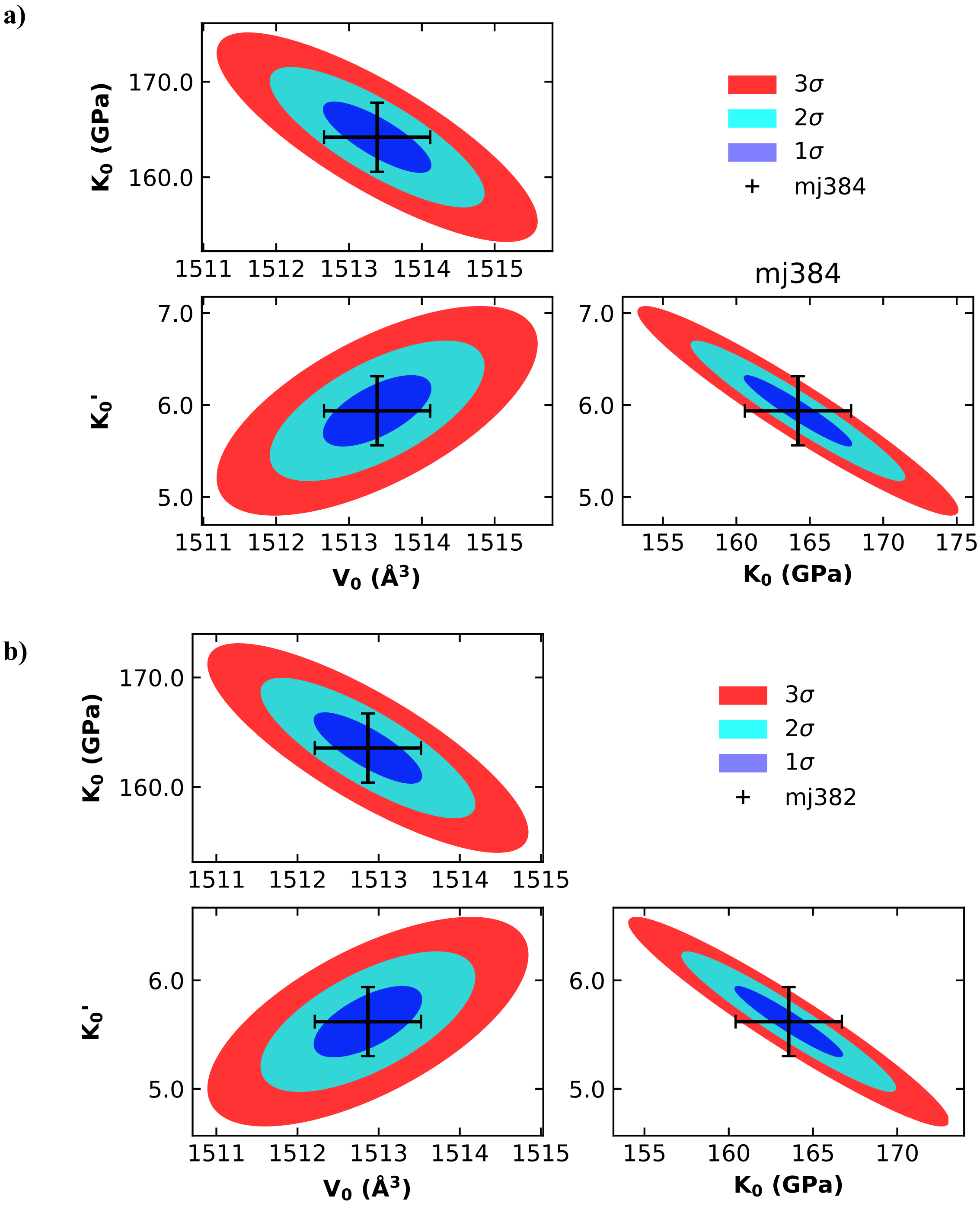

Figure 2.4: Confidence ellipse plots for sample a) MA384 and b) MA382. When overlaid the figures are nearly indistinguishable.

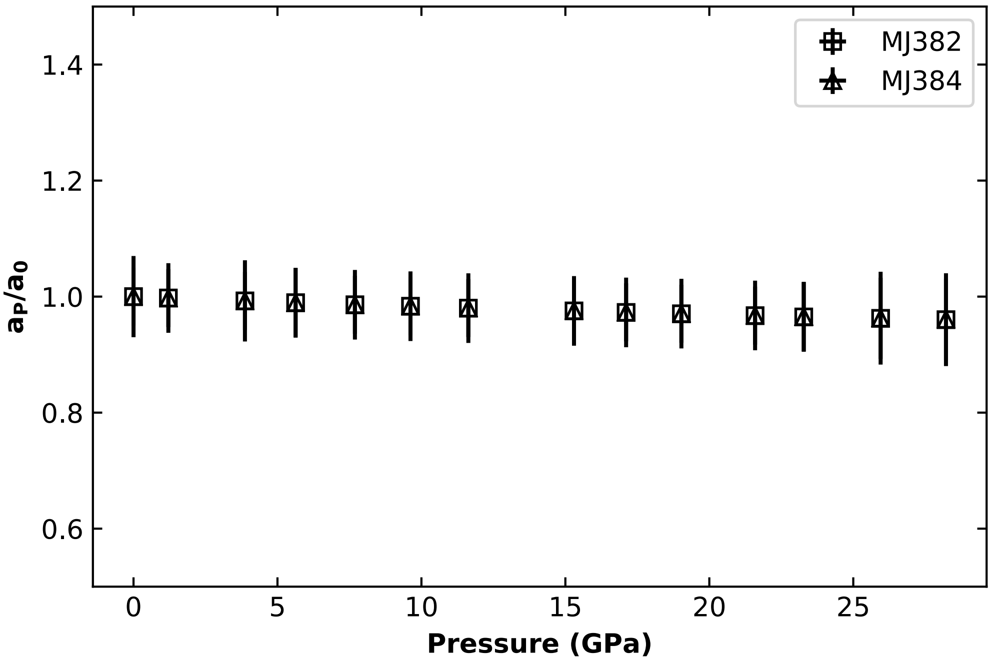

Figure 2.5: Normalized lattice parameter *a* for majoritic garnet samples MA384 and MA382. Within error, lattice parameters as a function of pressure are identical.

Table 2.3: Comparison of bulk modulus, pressure derivative, and isothermal temperature derivative of garnets

Source	Composition	V_0	K_T	dK_T/dP	K_s	dK_s/dP	dK_s/dT	G	dG/dP	dG/dT	Method
MA384	$Py_{76}Alm_{18}Mj_6$	1513.4(7)	164(4)	5.9(4)	162(3)	4.5(3)	-0.010(40)	88(3)	1.3(3)	-0.002(1)	Single crystal-XRD
MA382	$Py_{54}Alm_{38}Mj_8$	1512.9(7)	164(3)	5.6(3)	175(4)	5.8(4)	-0.020(50)	95(3)	0.7(3)	-0.01(7)	Single crystal-XRD
Pamato et al. (2016)	$Py_{76}Mj_{24}$	1506.8(7)	166(2)	4.7(2)	168(2)	4.7(2)	-0.014(15)	91.8(7)	1.40(5)	-0.0104(3)	Single crystal-XRD
Pamato et al. (2016)	$Py_{78}Alm_6Mj_{16}$	1506.8(2)	172(1)	4.1(1)	172(1)	4.2(1)	-0.014	93.0(6)	1.30(5)	-0.008(4)	Single crystal-XRD
Lu et al. (2013)	$Py_{68}Alm_{24}Gr_5Sp_1$	-	-	-	168(2)	4.4(1)	-0.023(4)	92(1)	1.28(1)	-0.0051(11)	Single crystal-XRD
D. Fan et al. (2017)	Py_{100} (Hy)	1505.38(27)	162(1)	4.9(2)	-	-	-0.018(4)	-	-	-	Powder-XRD
D. Fan et al. (2017)	Py_{100} (Hy)	1505.22(28)	168(1)	4^a	-	-	-0.017(5)	-	-	-	Powder-XRD
Sinogeikin and Bass (2002b)	Py_{100}	-	169(2)	-	171(2)	-	-0.019(3)	94(2)	-	-0.009(1)	Single crystal-XRD
Zou et al. (2012)	Py_{100}	1500.4(15)	167(3)	4.6^a	-	-	-0.021(9)	-	-	-	Powder-XRD
Du et al. (2015)	Py_{100}	1503.2	169.2(2)	4.4^a	-	-	-	-	-	-	Powder-XRD
Zhang et al. (1998)	Py_{100}	1502.9(3)	171(2)	4.4(2)	-	-	-	-	-	-	Single crystal-XRD
Du et al. (2015)	Py_{100}	1503.2	169.2(2)	4.4^a	-	-	-	-	-	-	Powder-XRD
∂Levien et al. (1979)	Py_{100}	1503.4(5)	175(1)	4.5(2)	-	-	-	-	-	-	Single crystal-XRD
Conrad et al. (1999)	Py_{100}	-	-	-	171	3.22	-	92	1.4	-	Single crystal
Sinogeikin and Bass (2000)	Py_{100}	-	-	-	171(3)	4.1(3)	-	94(2)	1.3(2)	-	Single crystal
Sinogeikin and Bass (2002a)	$Py_{50}Mj_{50}$	-	-	-	167(3)	4.2(3)	-	90(2)	1.4(2)	-	Polycrystalline
Sinogeikin and Bass (2002b)	$Py_{50}Mj_{50}$	-	165.2(20)	-	167(3)	-	-0.0145(20)	90(2)	-	-0.0082(10)	Polycrystalline
Sinogeikin and Bass (2002a)	Mj_{100}	-	-	-	166(3)	4.2(3)	-	85(2)	1.4(2)	-	Single crystal
Ridgen et al. (1994)	$Py_{62}Mj_{38}$	-	-	-	169(6)	5.3(2)	-	89(5)	2.0(1)	-	UI
Liu et al. (2000)	$Py_{62}Mj_{38}$	-	-	-	171(5)	6.2(5)	-	90(1)	1.9(2)	-	UI
Liu et al. (2000)	$Py_{50}Mj_{50}$	-	-	-	170(5)	6.4(5)	-	89(1)	2.1(2)	-	UI
Gwanmesia et al. (1998)	Mj_{100}	-	-	-	167(3)	6.7(4)	-	88(2)	1.9(1)	-	UI
Gwanmesia et al. (2006)	Py_{100}	1502.5	-	-	171(2)	3.9(3)	-0.0180(20)	91(1)	1.7(2)	-0.0100(10)	UI
Chen et al. (1999)	Py_{100}	-	-	-	171(2)	5.3(4)	-	92(1)	1.6(2)	-	UI

Hy: hydrous; UI: Ultrasonic interferometry; ^{a} fixed during fitting

When K_{T0} for both samples are compared, over the studied pressure range, the bulk moduli begin to deviate with increasing pressure (Figure 2.6). This is attributed to the 1% larger K_{T0}' of MA384 over that of MA382. The difference becomes more significant when extrapolated to 27 GPa.

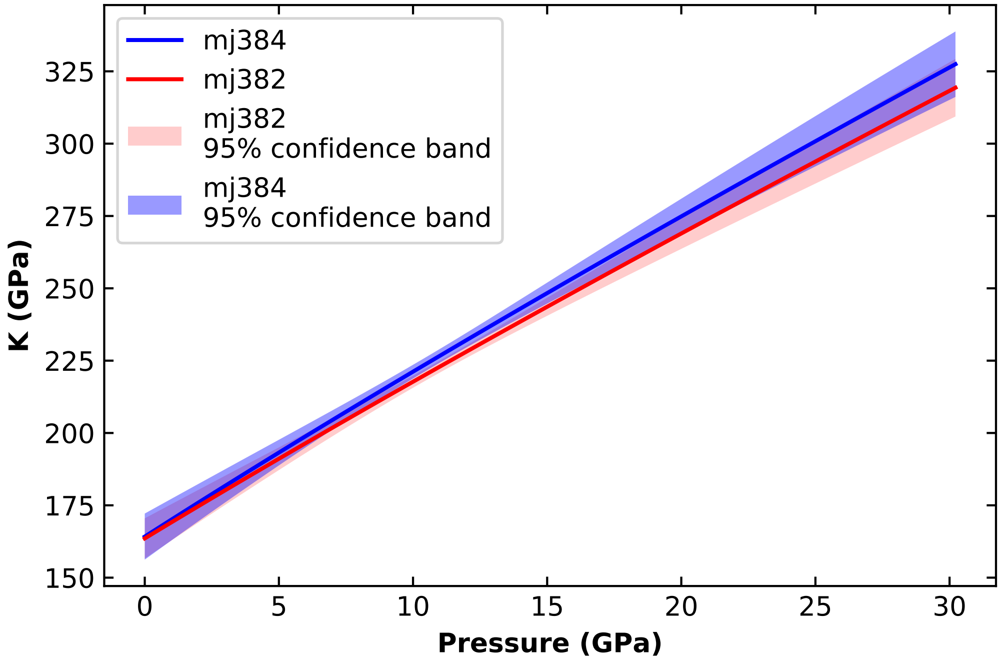

Figure 2.6: Comparison of isothermal bulk modulus (K) as a function of pressure for samples MA384 and MA382. Within error, K over the observed pressure range is identical between the two samples.

Both samples show slightly larger refined volumes than that of previously reported majoritic garnets (Table 2.3). The increased volume of ~0.5% is small yet significantly larger than our uncertainty. This increased volume is most likely a result of the varied composition from those of other reported majoritic garnets.

Imperfections in sample and detector alignment, hydrostaticity of the pressure medium, errors in calibration etc. normally make it exceptionally challenging to compare absolute values of measured parameters as opposed to relative values. The simultaneous compression of both samples within a single diamond anvil cell and simultaneous X-ray measurements provides the most direct comparison of compositional effect on equation of state parameters to date. This experimental design negates the impact of experimental uncertainties between experiments.

2.3.2 P-V-T Equation of State

Single-crystal X-ray diffraction measurements were made at three temperatures 298 K, 423 K, and 573 K. Throughout the investigated P-T range, both compositions maintain the *Ia-3d* cubic structure. After fitting room temperature data, we next fit the thermal equation of state parameters up to 27 GPa and 573 K using EoSFit7c (Angel et al. 2014). For sample MA384, data from six experiments and for sample MA382 six experiments were merged to complete the high-pressure and high-temperature data sets. P-V-T data are given in Table 2.2. During fitting V_0, K_{T0}, and K_{T0}' were fixed to refined parameters from the room temperature BM3 equations of state. The measured unit-cell volumes as a function of pressure as well as the isotherms calculated with thermoelastic parameters derived from current fits are plotted in Figure 2.7. The thermoelastic parameters $(\partial K_{T0}/\partial T)_P$, α_T, K_0, and K_{T0}' obtained for sample MA384 derived in this study from a high-temperature BM3 equation of state are: $(\partial K_{T0}/\partial T)_P = -0.01(40)$ GPa/K, $\alpha_T = 2.5(2) \times 10^{-5}$ K^{-1}, $K_0 = 164(4)$ GPa, and $K_{T0}' = 5.9(4)$. Thermoelastic parameters fit in this study for sample MA382 are: $(\partial K_{T0}/\partial T)_P = -0.02(5)$ GPa/K, $\alpha_T = 2.5(3) \times 10^{-5}$ K^{-1}, $K_0 = 164(3)$ GPa, and $K_{T0}' = 5.6(3)$. Both K_0 and K_{T0}' were fit in the isothermal experiment. The results here indicate the compositional difference between MA384 and MA382 has no impact on their thermoelastic parameters within error.

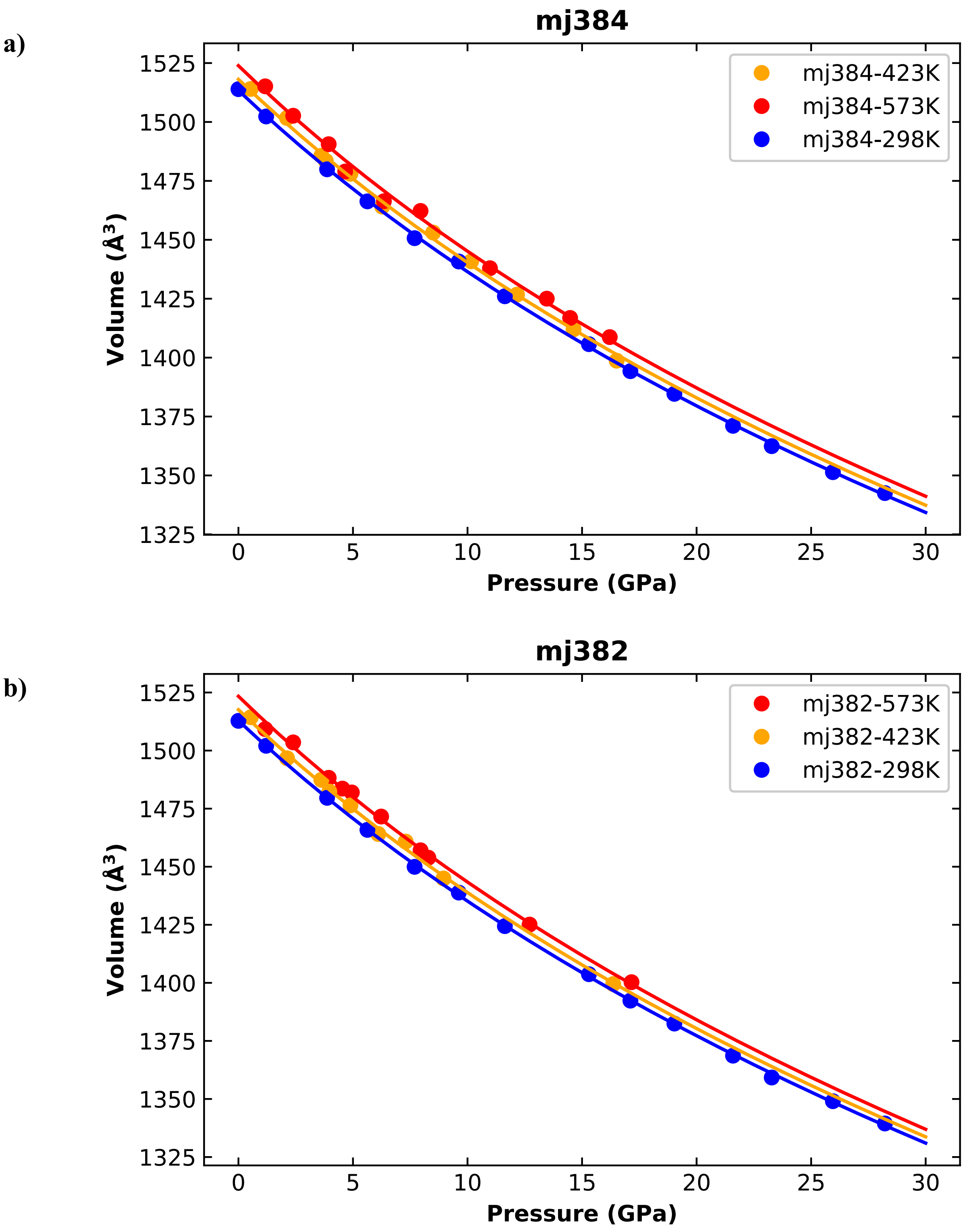

Figure 2.7-1: Unit-cell volume as a function of pressure and temperature for majoritic garnet samples a) MA384 and b) MA382 and fit isotherms. Volumes are fit to high-temperature third-order Birch-Murnaghan equations of state

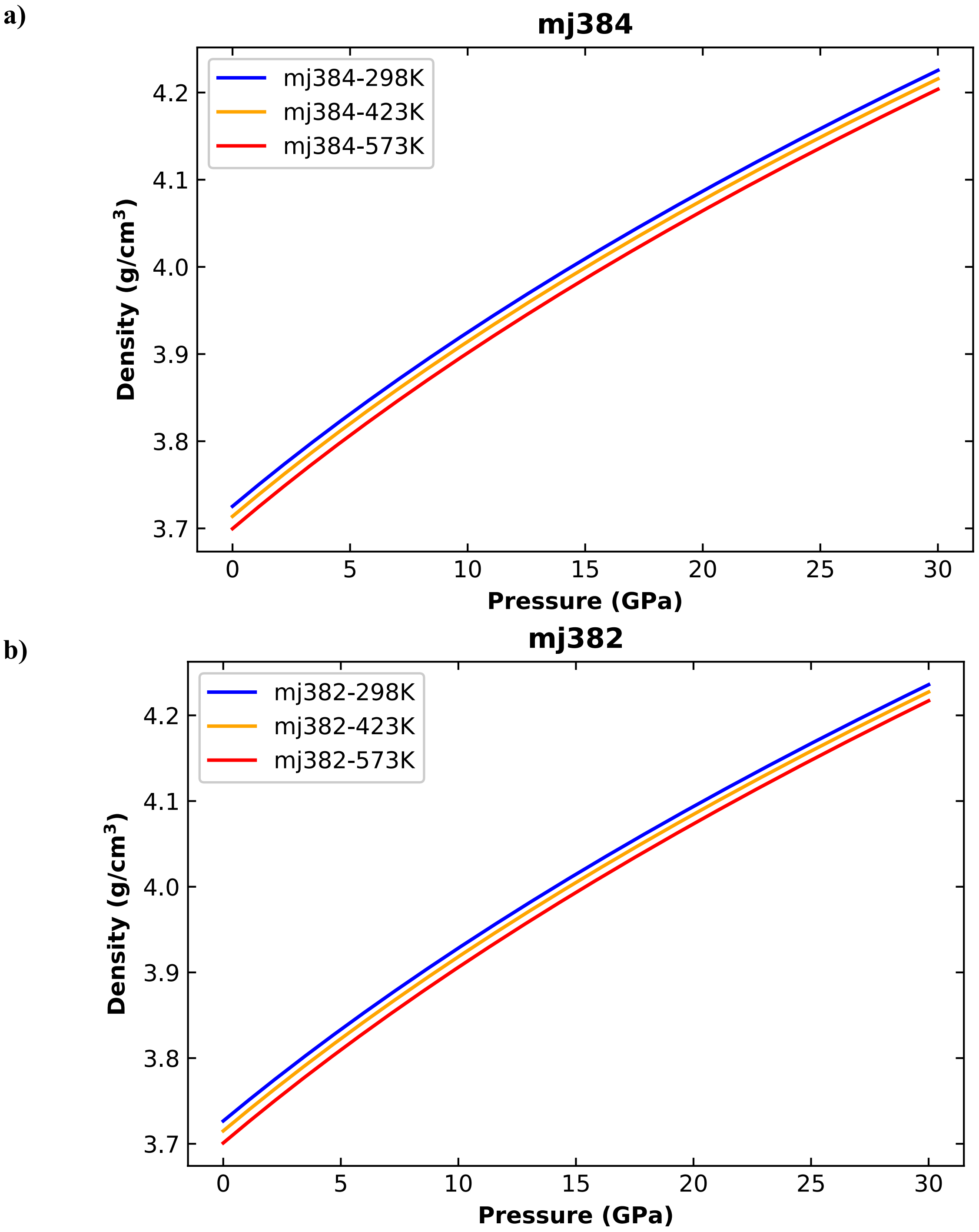

Figure 2.7-2: Calculated densities of sample a) MA384 and b) MA382 as a function of pressure. Densities were calculated from optimized fits to high-temperature third-order Birch-Murnaghan equations of state reported above.

2.3.3 Elasticity

Stress and strain in a crystal of arbitrary symmetry according to Hooke's law:

$$\sigma_{ij} = c_{ijkl}\varepsilon_{kl} \qquad [2.7]$$

where σ_{ij} is the stress tensor, ε_{kl} is the strain tensor, and c_{ijkl} is the fourth rank elastic stiffness tensor. The elastic stiffness tensor contains 81 independent components. The stress and strain tensors are symmetric due to the assumption of static equilibrium; this reduces the 81 components of the elastic stiffness tensor to 36. The number of independent components can further be reduced given that the change in energy per unit volume of a body resulting from a set of strains is given by the summation $1/2 \sum_{ijkl} c_{ijkl}\varepsilon_{ij}\varepsilon_{kl}$ over all of the strain and tensor components (Angel et al., 2009). This summation implies the equality $c_{klij} = c_{ijkl}$ (Nye, 1957). This reduces the number of independent components from 36 to 21. The application of crystal symmetry can further reduce the number of independent components. In a cubic system, the independent components become C_{11}, C_{12}, and C_{44}.

Elastic moduli for polycrystalline samples can be derived from single-crystal moduli of the aggregate components. The aggregate elastic parameters lie between two limits named the Voigt and Reuss bounds. The arithmetic average of the two bounds, known as the Voigt-Reuss-Hill average, is commonly used (Hill, 1951).

The Voigt bound is defined as (Voigt, 1928):

$$X_V = \sum_i v_i X_i \qquad [2.8]$$

where v_i is the volume fraction and X_i is the bulk or shear modulus for the *i*th phase. The Voigt bound assumes constant strain across all phases and serves at the upper bound for the bulk or shear modulus for a polycrystalline material. The Reuss bound is defined as (Reuss, 1929):

$$X_R = \left(\sum_i \frac{v_i}{X_i}\right)^{-1} \quad [2.9]$$

where X_i is the bulk or shear modulus for the *i*th phase. The Reuss average assumes constant stress across all phases, serving as the lower bound for the bulk or shear modulus for a polycrystalline material. The Voigt-Reuss-Hill average defined as:

$$X_{VRH} = \frac{1}{2}(X_V + X_R) \quad [2.10]$$

2.3.4 Elasticity of Majoritic Garnet

High P-T Brillouin spectra were collected up to 17 GPa and 573 K. An example Brillouin spectrum is shown in Figure 8. Four peaks from the sample can be seen corresponding to the high velocity longitudinal modes V_{P1}, V_{P2}, and the low velocity shear modes V_{S1}, V_{S2}. Majoritic garnets show no shear wave splitting due to their high degree of elastic isotropy. The acoustic velocities of MA384 measured in different crystallographic directions as a function of χ at room temperature and pressure are shown in Figure 9. With changing crystallographic direction no velocity difference can be seen within error. The elastic anisotropy of the majoritic garnet is negligible and persists at higher pressures and temperatures. The observed low degree of elastic anisotropy is consistent with other published observations (Pamato et al. 2016; Sinogeikin and Bass, 2000; Murakami et al., 2008; Lu et al., 2013).

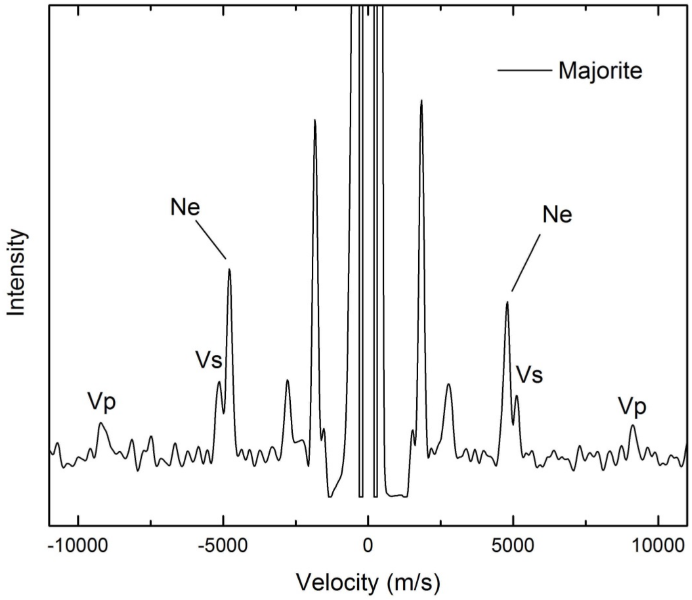

Figure 2.8: Example Brillouin spectrum of majoritic garnet sample.

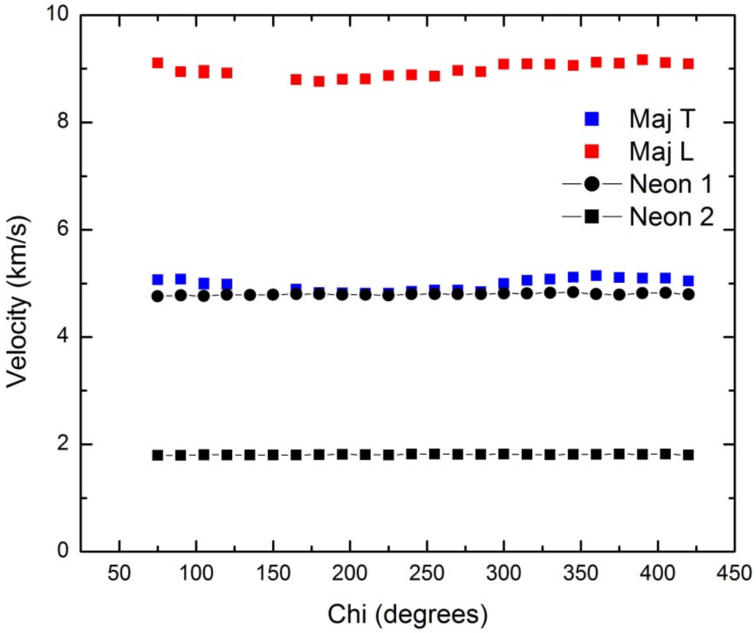

Figure 2.9: Transverse (T) and longitudinal (L) wave velocities as a function of crystallographic direction Chi for sample MA384.

Measured velocities, V_P or V_S, are a function of the wave propagation direction and polarization, elastic moduli C_{ijkl}, and the density, ρ, of a material, according to the Christoffel Equation:

$$|c_{ijkl}n_j n_i - \rho V_{P,S}{}^2 \delta_{ik}| = 0 \qquad [2.11]$$

where δ_{ik} is the Kronecker delta. n_i are the direction cosines of the phonon propagation direction and is described by three Euler angles (θ, χ, φ). For low symmetry and highly anisotropic materials the Christoffel Equation can be used to solve for the complete elastic tensor, C_{ijkl}, by fitting the measured acoustic velocities and orientations using non-linear least squares methods. However for high symmetry and negligible anisotropy materials such as majoritic garnet, the elastic constants can be obtained by averaging the measured acoustic velocities over several non-symmetric directions (Sinogeikin and Bass, 2000, Lu et al., 2013). In this study, aggregate V_p and V_s were obtained by averaging all longitudinal and transverse velocity measurements at each pressure and temperature. Single-crystal elastic moduli were then calculated from aggregate velocities and related to aggregate moduli through:

$$C_{11} = K + {}^{4}/_{3}\, G = \rho V_p^2 \qquad [2.12]$$

$$C_{44} = G = \rho V_s^2 \qquad [2.13]$$

$$C_{12} = K - {}^{2}/_{3}\, G = \rho\left(V_p^2 - V_s^2\right) \qquad [2.14]$$

Relations 2.12-14 assume the equality:

$$2C_{44} = C_{11} - C_{12} \qquad [2.15]$$

Equation 2.15 implies elastic isotropy of the sample, a well-established assumption for majoritic garnets as discussed previously.

The elastic properties of both samples are summarized in Table 2.4.

The bulk, K_s, and shear, G, moduli as a function of pressure and calculated single-crystal elastic moduli for majoritic garnets are reported in Figure 2.10 and Figure 2.11, respectively. For comparison, previously published data of dry majoritic garnets with compositions $Mg_{3.24}Al_{1.53}Si_{3.23}O_{12}$ [$Py_{76}Mj_{24}$] (pamato_mj) and $Mg_{3.01}Fe_{0.17}Al_{1.68}Si_{3.15}O_{12}$ [$Py_{78}Alm_6Mj_{16}$] (pamato_fe-mj) are shown (Pamato et al., 2016).

Pressure derivative of the bulk modulus, $(\partial Ks/\partial P)_T$, and shear modulus, $(\partial G/\partial P)_T$, at constant temperature were obtained by fitting elastic moduli, K_s and G, as a function of density using a BM3 equation of state:

$$Ks = (1+2f)^{5/2}\left\{Ks_o + \left[Ks_o\left(\frac{\partial Ks}{\partial P}\right)_T - 5Ks_o\right]f + \frac{27}{2}\left[Ks_o\left(\frac{\partial Ks}{\partial P}\right)_T - 4Ks_o\right]f^2\right\} \quad [2.16]$$

$$G = (1+2f)^{5/2}\left\{G_o + \left[3Ks_o\left(\frac{\partial G}{\partial P}\right)_T - 5G_o\right]f\right\} \quad [2.17]$$

$$f = \frac{1}{2}\left[\left(\frac{\rho}{\rho_o}\right)^{2/3} - 1\right] \quad [2.18]$$

where f is the Eulerian strain, ρ is the density at given pressure, and ρ_o is the density at ambient pressure. At ambient temperature, densities were calculated from 298K BM3 equation of state.

Temperature derivatives of the elastic moduli at high pressure were determined by fitting a high-temperature form of the third-order Birch-Murnaghan equation of state (Duffy and Wang, 1998).

$$Ks(T) = Ks_o(T_o) + \left(\frac{\partial Ks}{\partial T}\right)_P (T - T_o) \quad [2.19]$$

$$G(T) = G_o(T_o) + \left(\frac{\partial G}{\partial T}\right)_P (T - T_o) \quad [2.20]$$

where T_0 is the reference temperature (298 K). High-temperature volumes and densities were calculated from our isothermal BM3 equation of state. The relationship between K_S, K_T is discussed in Section 2.3.5.

For MA384 the adiabatic bulk modulus and shear modulus were $Ks_0 = 162(3)$ GPa and $G_0 = 88(3)$ GPa with corresponding pressure derivatives $(\partial K_S/\partial P)_T = 4.5(3)$ and $(\partial G/\partial P)_T = 1.3(3)$. The temperature derivatives at constant pressure for MA384 are $(\partial K_S/\partial T)_P = -0.010(40)$ GPa/K and $(\partial G/\partial T)_P = -0.002(1)$ GPa/K. For MA382 the adiabatic bulk modulus and shear modulus were $Ks_0 = 175(4)$ GPa and $G_0 = 95(3)$ GPa with corresponding pressure derivatives $(\partial K_S/\partial P)_T = 5.8(4)$ and $(\partial G/\partial P)_T = 0.7(3)$. The temperature derivatives for MA382 are $(\partial K_S/\partial T)_P = -0.020(50)$ GPa/K and $(\partial G/\partial T)_P = -0.01(7)$ GPa/K. Large errors observed in temperature derivatives most likely result from the merging of data from several experiments to complete the high-temperature data set.

a)

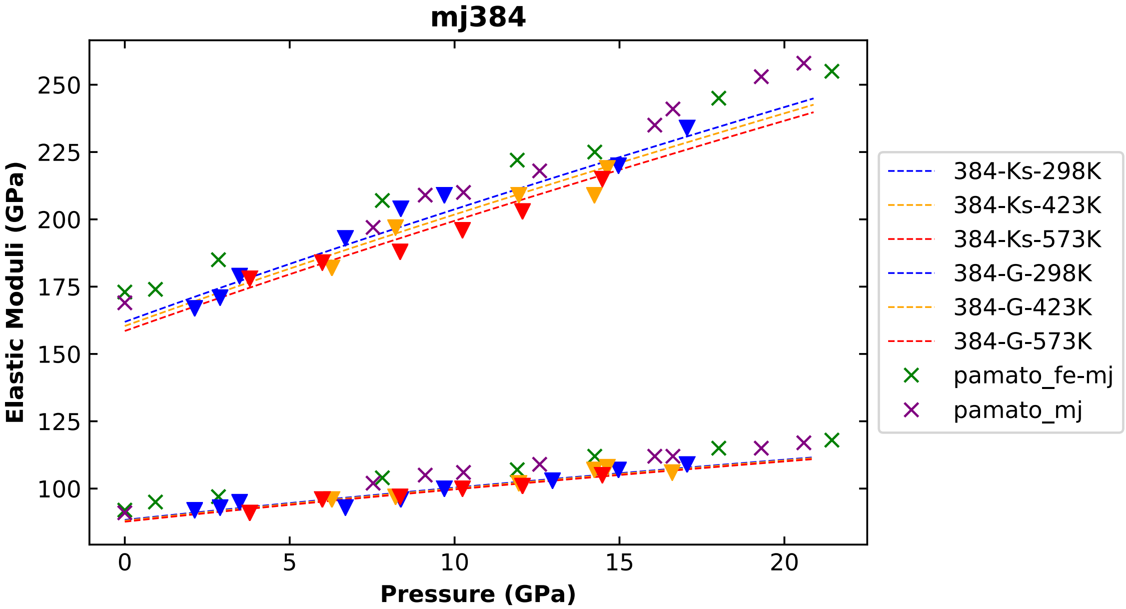

b)

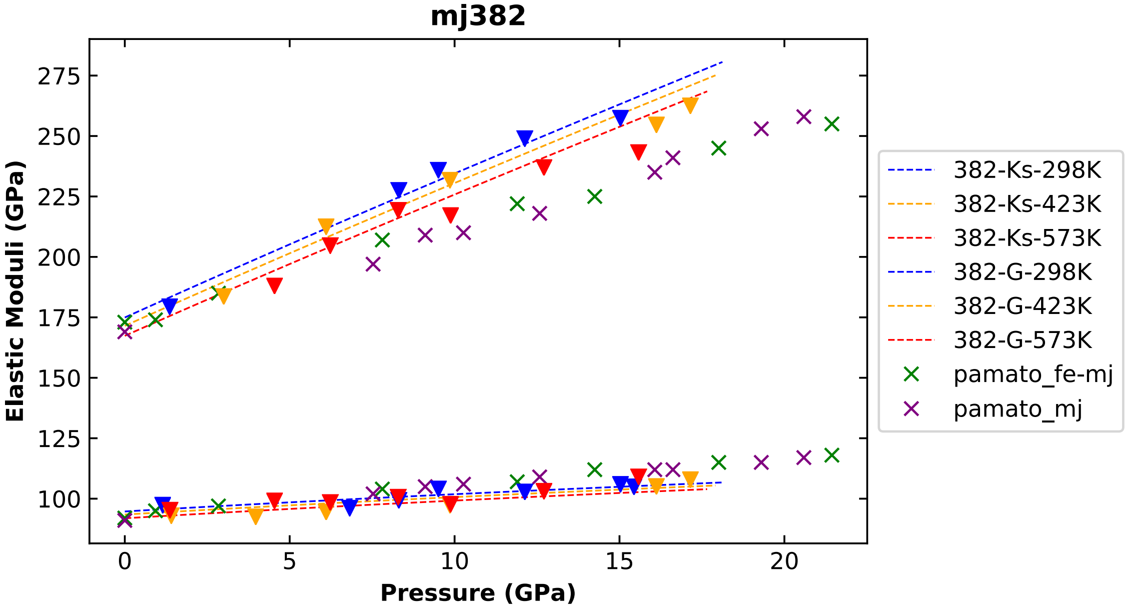

Figure 2.10: Calculated adiabatic bulk modulus (Ks) and shear modulus (G) for samples a) MA384 and b) MA382 majoritic garnet samples from Pamato et al. (2016). Calculated parameters have ben fit to a high-temperature form of the third-order Birch-Murnaghan equation of state (dashed lines).

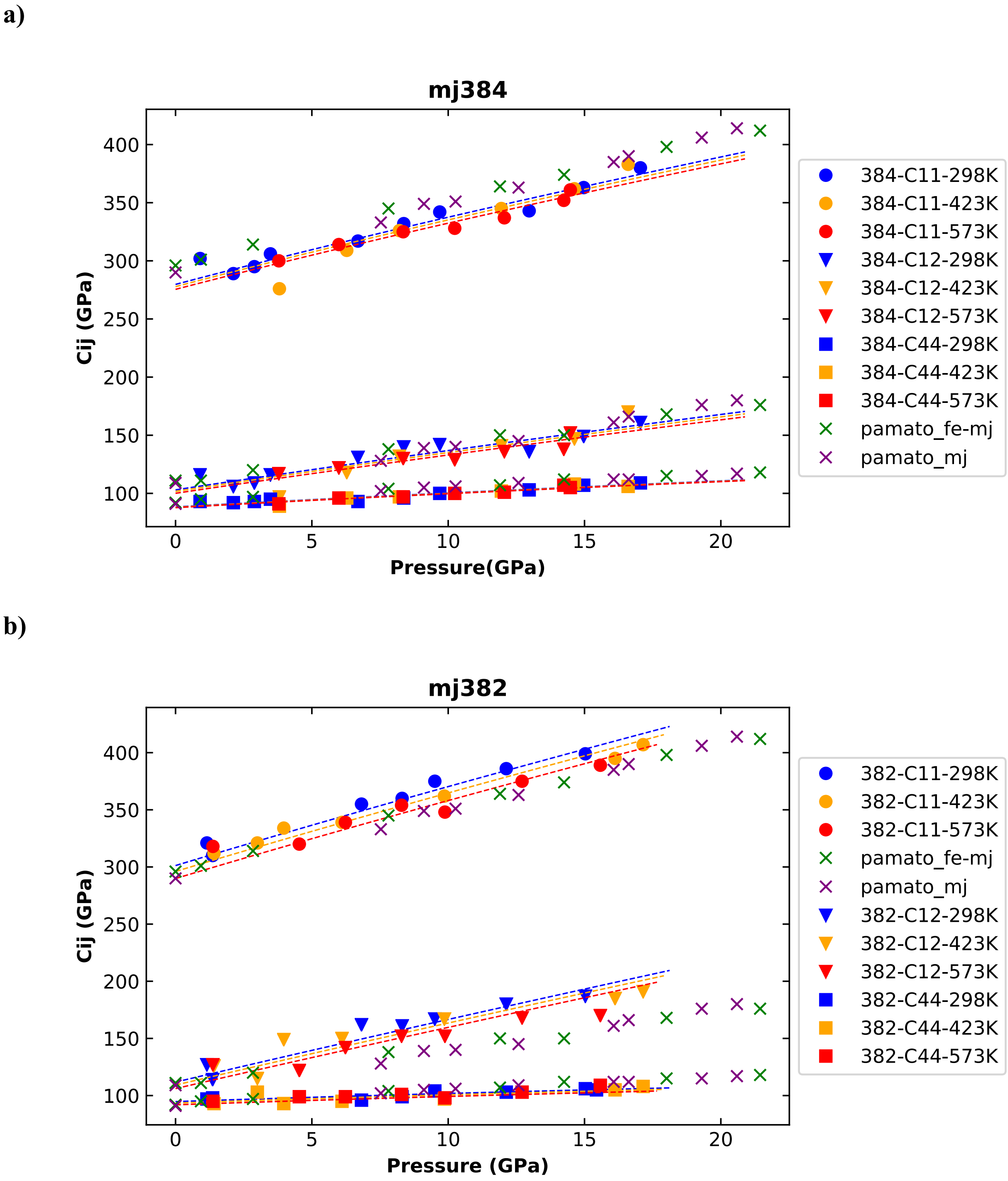

Figure 2.11: Calculated elastic moduli of samples a) MA384 and b) MA382 as compared with majoritic garnet samples from Pamato et al. (2016).

Table 2.4-1: Sample MA384 velocities and elastic parameters.

P (Gpa)	T (K)	Vs (km/s)	Vp (km/s)	ρ (g/cm^3)	C11 (GPa)	C12 (GPa)	C44 (GPa)	Ks (GPa)	G (GPa)
0.9	298	4978	8977	3.746	302	116	93	178	93
8.37	298	4960	9232	3.896	332	140	96	204	96
9.69	298	5050	9346	3.919	342	142	100	209	100
2.12	298	4931	8758	3.772	289	106	92	167	92
2.89	298	4954	8826	3.788	295	109	93	171	93
3.48	298	5001	8971	3.801	306	116	95	179	95
6.69	298	4903	9057	3.864	317	131	93	193	93
12.97	298	5097	9285	3.976	343	136	103	205	103
14.97	298	5168	9513	4.009	363	149	107	220	107
17.05	298	5198	9694	4.042	380	161	109	234	109
8.21	423	4998	9167	3.882	326	132	97	197	97
3.81	423	4853	8527	3.796	276	97	89	157	89
6.28	423	4986	8969	3.845	309	118	96	182	96
11.95	423	5084	9346	3.948	345	141	102	209	102
14.63	423	5193	9523	3.993	362	147	108	219	108
16.6	423	5136	9749	4.025	383	170	106	241	106
14.24	423	5185	9395	3.987	352	138	107	209	107
3.79	573	4916	8899	3.782	300	117	91	178	91
5.99	573	4998	9054	3.826	314	122	96	186	96
8.35	573	5017	9160	3.871	325	130	97	195	97
10.24	573	5049	9170	3.906	328	129	100	196	100
12.06	573	5060	9256	3.937	337	136	101	203	101
14.48	573	5128	9532	3.978	361	152	105	222	105
17.62	573	5128	9922	4.028	397	185	106	255	106

Table 2.4-2: Sample MA382 velocities and elastic parameters.

P (Gpa)	T (K)	Vs (km/s)	Vp (km/s)	ρ (g/cm^3)	C11 (GPa)	C12 (GPa)	C44 (GPa)	Ks (GPa)	G (GPa)
1.15	298	4954	8998	3.969	321	127	97	191	97
1.36	298	4954	8825	3.974	310	114	98	179	98
6.82	298	4847	9309	4.093	355	162	96	226	96
9.51	298	5011	9507	4.146	375	167	104	236	104
8.31	298	4910	9346	4.123	360	161	99	228	99
12.13	298	4952	9594	4.195	386	180	103	249	103
15.03	298	4996	9690	4.247	399	187	106	257	106
15.44	298	4968	-	4.254	-	-	105	-	105
1.41	423	4845	8876	3.963	312	126	93	188	93
3.0	423	5079	8962	4.000	321	115	103	184	103
3.97	423	4798	9113	4.021	334	149	93	211	93
6.105	423	4822	9125	4.067	339	150	95	213	95
9.86	423	4849	9344	4.142	362	167	97	232	97
16.12	423	4970	9632	4.256	395	185	105	255	105
17.15	423	5026	9753	4.274	407	191	108	263	108
1.37	573	4914	8976	3.948	318	127	95	191	95
4.54	573	4967	8926	4.020	320	122	99	188	99
6.23	573	4928	9146	4.056	339	142	99	205	99
8.29	573	4957	9289	4.098	354	152	101	219	101
9.88	573	4866	9174	4.130	348	152	98	217	98
12.71	573	4966	9463	4.183	375	168	103	237	103
15.58	573	5076	9581	4.234	389	170	109	243	109

2.3.5 Comparison to Literature

Thermoelastic parameters and their pressure derivatives for majoritic garnets MA384 ($Py_{76}Alm_{18}Mj_6$) and MA382 ($Py_{54}Alm_{38}Mj_8$) are summarized in Table 2.5 along with literature data for garnets along the majorite-pyrope solid solution. The adiabatic bulk modulus (K_S), shear modulus (G), as well as the isothermal bulk modulus (K_T) are in good agreement with previously reported values (Pamato et al., 2016; Sinogeikin and Bass et al., 2002; Liu et al., 2000). Elastic parameters K_S, K_T, and G are also summarized in Figure 2.12 as a function of pyrope content for comparison with literature data. Within error, our measured elastic parameters agree with compositionally similar garnets. While $(\partial K_T/\partial P)_T$ is relatively large when compared to previously reported values thermoelastic parameter derivatives, $(\partial G/\partial P)_T$, $(\partial Ks/\partial T)_P$, and $(\partial G/\partial T)_P$ agree well (Pamato et al., 2016; Sinogeikin and Bass, 2000).

Direct comparison of elastic parameters is made difficult by large compositional variations among reported garnets along the pyrope-majorite solid solution. However, general observations can be made when reported values are viewed in composition space (Figure 2.12). Also, Pamato et al. (2016) measured samples of majoritic garnet with roughly similar pyrope content allowing for a more direct comparison. Pamato's samples differ in composition due to different sample synthesis conditions from those of MA384 and MA382. Sample MA384 shows a softening of all elastic parameters K_S, K_T, and G when compared to literature values of dry garnets. Pamato et al. (2016) reported measured values of K_S = 172(1) GPa and G = 93.0(6) GPa for an anhydrous sample with composition $Py_{78}Alm_6Mj_{16}$. Our hydrous sample, MA384, containing 881 wt ppm H_2O yielded K_S = 162(3) GPa and G = 88(3) GPa. Ignoring iron and chromium contributions, when compared to Pamato et al. (2016), we see a decrease of ~6% in elastic parameters from 881 wt ppm H_2O. D. Fan et al. (2017) measured a hydrous (~900 wt ppm

H_2O) sample of Py_{100} with K_T = 162(1) GPa noting a ~7% decrease in bulk modulus resulting from 900 wt ppm H_2O.

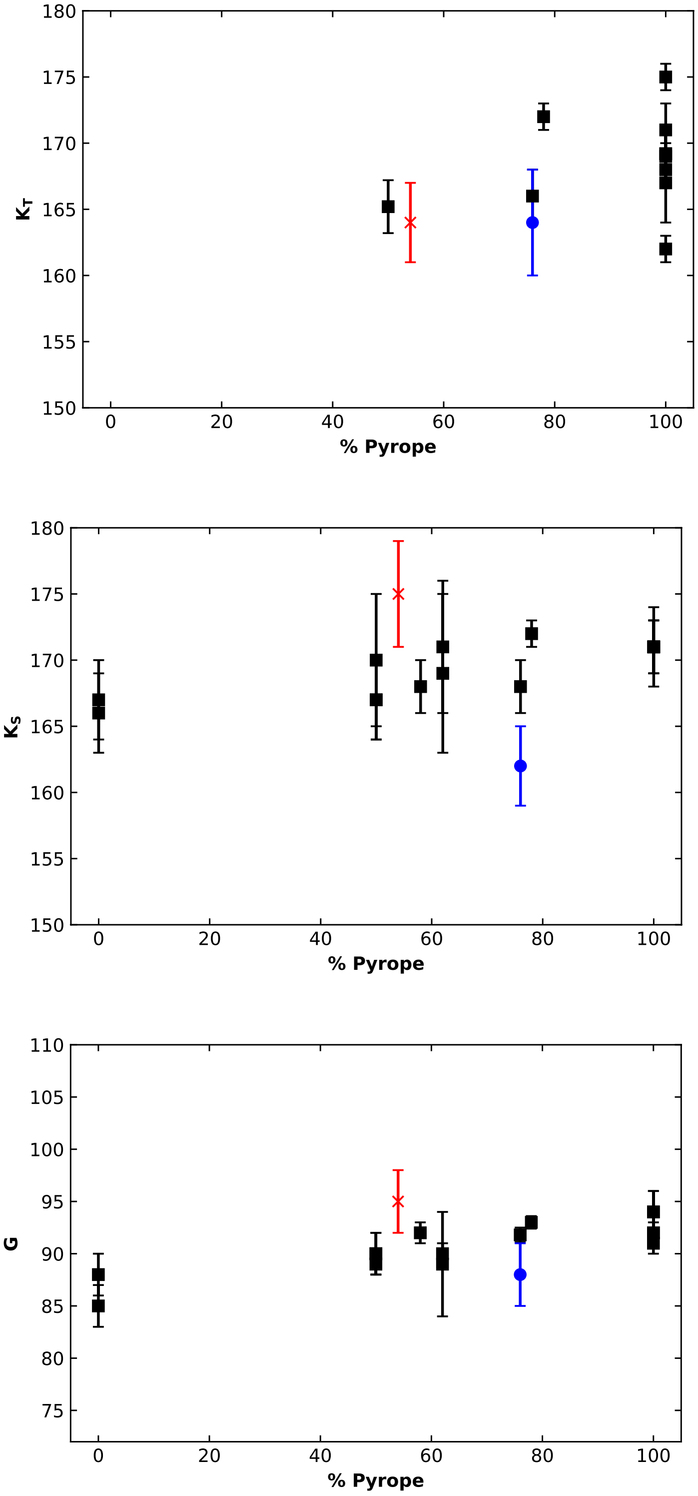

Figure 2.12: Comparison of garnet elastic parameter literature values from Table 2.3 with MA384 (*blue circle*) and MA382 (*red x*).

On comparison of elastic parameter derivatives the opposite trend becomes apparent. Pamato et al. (2016) reports a $(\partial K_T/\partial P)_T$ = 4.1(1), $(\partial K_S/\partial P)_T$ = 4.2(1), and $(\partial G/\partial P)_T$ = 1.30(5). Our MA384 sample showed $(\partial K_T/\partial P)_T$ = 5.9(4), $(\partial K_S/\partial P)_T$ = 4.5(3), and $(\partial G/\partial P)_T$ = 1.30(3). Our sample with 881 wt ppm water shows an increase in the adiabatic bulk modulus first derivative of ~7%. D. Fan et al. (2017) noticed a slight increase in the first derivative of the isothermal bulk modulus. No change is observed in $(\partial G/\partial P)_T$ with increasing hydration. The observed impact of water content on elastic properties, reducing K_0 and increasing K_{T0}', is also consistent with trends observed in olivine (Jacobsen 2006). Observation of trends in $(\partial Ks/\partial T)_P$ from our data would be speculative at best due to the large uncertainties. However, water appears to have little or no impact on $(\partial Ks/\partial T)_P$ when comparing dry and hydrous Py_{100} (Sinogeikin and Bass et al., 2002b; D. Fan et al., 2017).

Sample MA382 adiabatic bulk modulus is anomalously high compared to its independently measured isothermal bulk modulus. The adiabatic bulk modulus and isothermal bulk modulus are related by the thermodynamic relationship:

$$K_S = K_T(1 + \alpha\gamma T) \qquad [2.21]$$

Where α is the coefficient of thermal expansion, γ is the Grüneisen parameter. At ambient conditions typical values for garnet α and γ are ~$2.6\text{x}10^{-5}$ K^{-1} and ~1.1, respectively (Stixrude and Lithgow-Bertelloni, 2011, Wang et al., 1998). Adiabatic bulk modulus is then expected to be ~1-3% larger than the isothermal bulk modulus at ambient conditions. Our results show a difference of over 6% between K_{S0} and K_{T0}. The MA382 sample also shows a relatively large shear modulus G when compared to other garnets along the pyrope-majorite solid solution. The high Cr content of MA382 is unique and its impact on the elastic properties of MA382 requires further investigation.

Results presented here show a softening of the adiabatic elastic parameters and an increase in their first derivatives as a result of increased hydration. The impact of water on thermoelastic parameters is uncertain and could better be characterized with experiments reaching higher temperature, potentially up to 1500 K.

2.3.6 Lower Mantle Velocities

We determine the impact of hydrous majoritic garnet on mantle seismic velocity profiles by first determining the impact of water on bulk elastic properties of dry majoritic garnet. Exact determination the impact of OH defects on majoritic garnet elastic properties from data collected in this study is challenging due to the non-end member compositions. We address this by assembling a theoretical dry majoritic garnet with similar composition to use for comparison.

Elastic properties for a phase consisting of a solid solution composition can be determined by taking a weighted sum of the individual component elastic parameters. This calculation assumes the elastic parameters vary as a linear function of the end-member properties. This assumption does not hold for grossular-pyrope solid solutions where elastic parameters have been shown to vary wildly as a function of composition (Du et al., 2015). The grossular-pyrope system behaves non-linearly due to microstrain induced by the large cation radius mismatch of Ca^{2+} and Mg^{2+} (Haselton and Newton, 1980). Fortunately, Fe^{2+} and Mg^{2+} have far more similar radii and behave similarly on the garnet cubic X-site. Calculations performed by Erba et al. (2014) show garnets that do not contain Ca do tend to hold to the linear relationship between composition and elastic parameters. Given the composition of sample MA384, $Py_{76}Al_{18}Mj_6$, we assume the linear relationship in order to calculate bulk elastic parameters of our dry sample.

End member elastic parameters from Stixrude and Lithgow-Bertelloni (2011) were used to calculate the dry majoritic garnet elastic parameters. The Stixrude and Lithgo-Bertelloni (2011) majorite solid solution model does not allow Fe to enter the octahedral site. This results in complications when using their database to build majorite-rich garnet solid solutions for Fe-rich garnets. However, for our compositions the almandine/pyrope ratios are low and should not result in such problems. Calculated elastic properties for dry $Py_{76}Al_{18}Mj_6$ were: K_T = 171 GPa and G = 94 GPa. Direct comparison with elastic parameters for wet (881 wt ppm H_2O) yielded a decrease in K_T of 6.1% and G of 5.9%.

We assumed a pyrolite compositional model (Xu et al., 2008) and adjusted bulk modulus and shear moduli according to our results. Elastic parameter derivatives were left at the original Stixrude and Lithgow-Bertelloni (2011) values due to the large uncertainty in our results. Phase proportions were then calculated along a typical 1673 K adiabatic geotherm. All bulk mantle calculations were performed using the computer program HyMaTZ (Wang et al., *submitted*). Seismic velocities V_P and V_S were then calculated for a dry pyrolitic mantle and “wet” pyrolitic mantle, where “wet” refers to a pyrolitic mantle with hydrous garnet. Calculated velocity profiles can be seen in Figure 2.13.

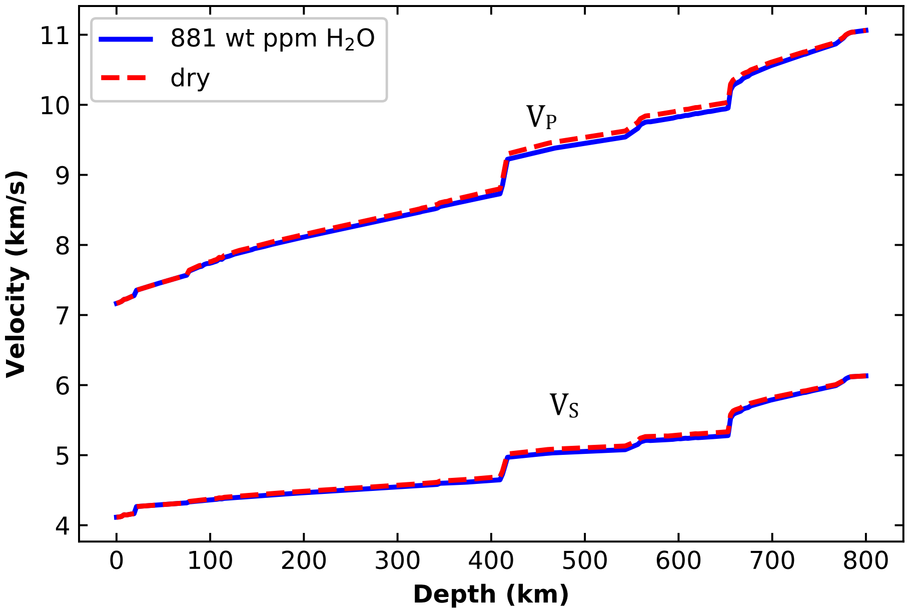

Figure 2.13: Mantle seismic velocity profiles calculated for dry pyrolite and pyrolite containting garnet with 881 wt ppm H_2O.

As anticipated, the addition of water to garnet in the mantle results in reduced velocities and an increased $\partial \mathrm{Velocity}/\partial \mathrm{Depth}$. The impact of hydrous garnet on seismic velocities is potentially the largest in the uppermost lower mantle (660 – 800 km depth) (Figure 2.14). At 660 km depth the addition of 881 wt ppm H_2O to garnet will produce a decrease in shear velocities of 0.86% when compared to a dry pyrolite mantle (Figure 2.15). If we extrapolate to a garnet containing a liberal estimate for the maximum H_2O storage capacity (~2000 wt ppm H_2O) we calculate a maximum shear velocity reduction of 1.8% compared to V_S in a dry pyrolite mantle.

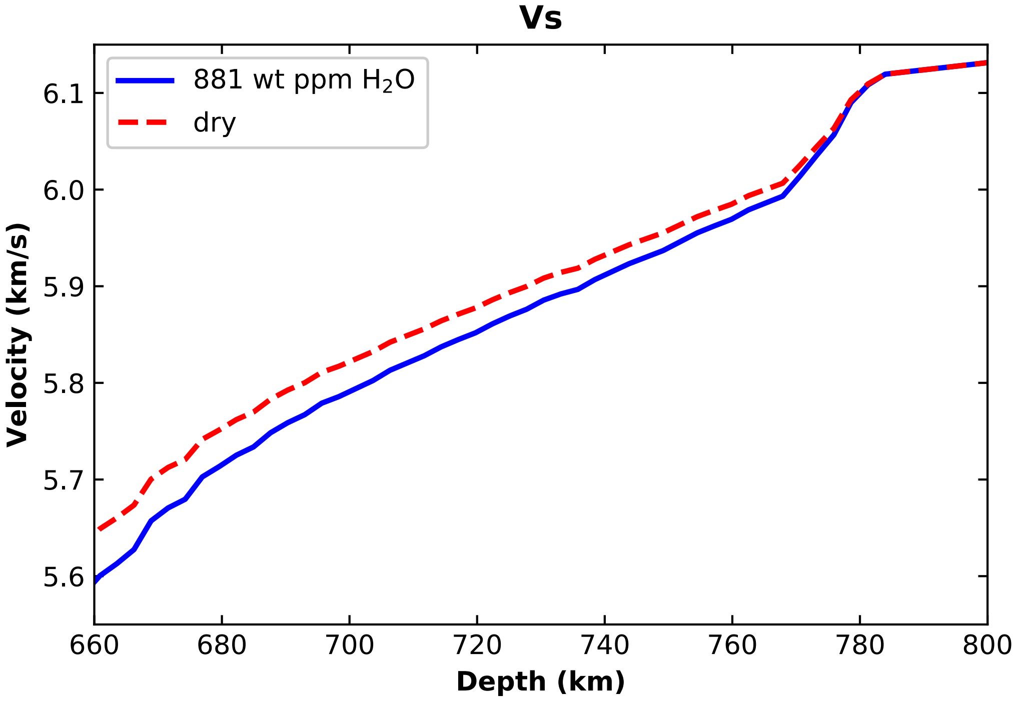

Figure 2.14: Shear velocity profile calculate for a dry pyrolite model (*red dashed line*) and pyrolite with garnet containing 881 ppm H_2O (*solid blue line*) in the upper lower mantle.

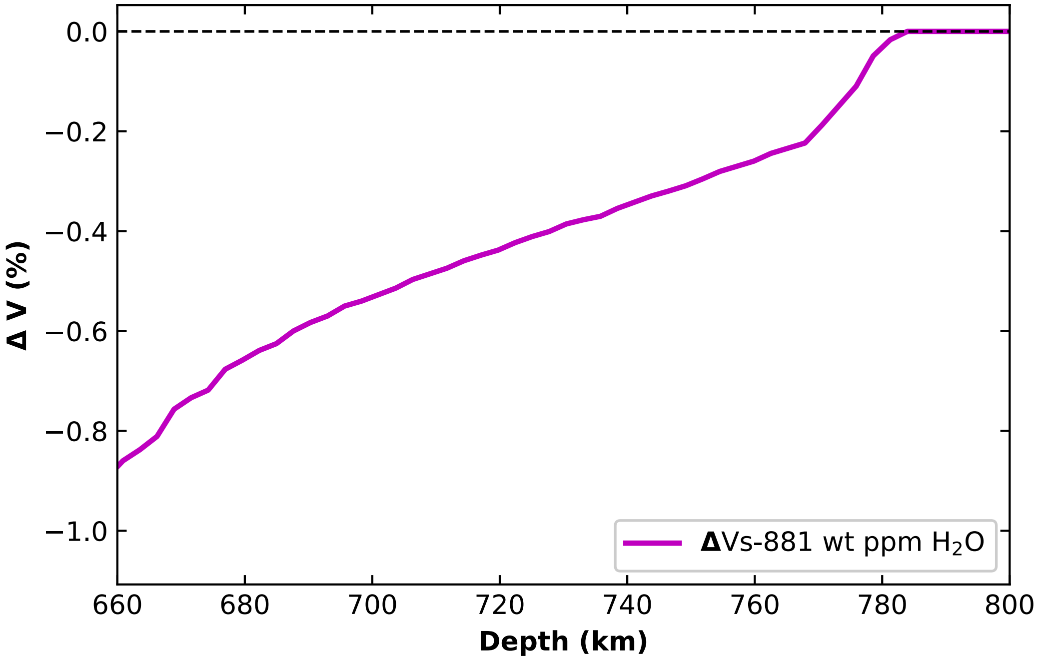

Figure 2.15: Plot of change in shear velocity between dry pyrolite and pyrolite with garnet containing 881 wt ppm H_2O (*purple line*). Black dashed line marks 0 velocity difference.

2.3.7 Implications for Seismic Structures

The reduction in shear velocity observed in LVZs below the 660 km discontinuity is too large to be a result of hydrous garnet alone. Schmandt et al. (2014) observed a LVZ beginning at ~730 km depth with a maximum ~2.5% V_S reduction at 750 km depth (Figure 2.16). The negative velocity gradient observed by Schmandt et al. (2014), as well as that produced by the addition of 881 wt ppm H_2O into garnet relative to dry pyrolite, can be seen in Figure 2.17. Our results show greater than 5000 wt ppm H_2O would be required to achieve the ~2.5% V_S reduction at 750 km depth observed by Schmandt et al. (2014). The addition of large amounts of water to garnet at these depths would also cause large LVZs directly beneath the 660 km discontinuity and cannot account for the separation of ~100 km between the discontinuity and observed LVZs (Schmandt et al., 2014; Liu et al., 2016; Zhang et al., 2018; Liu et al., 2018).

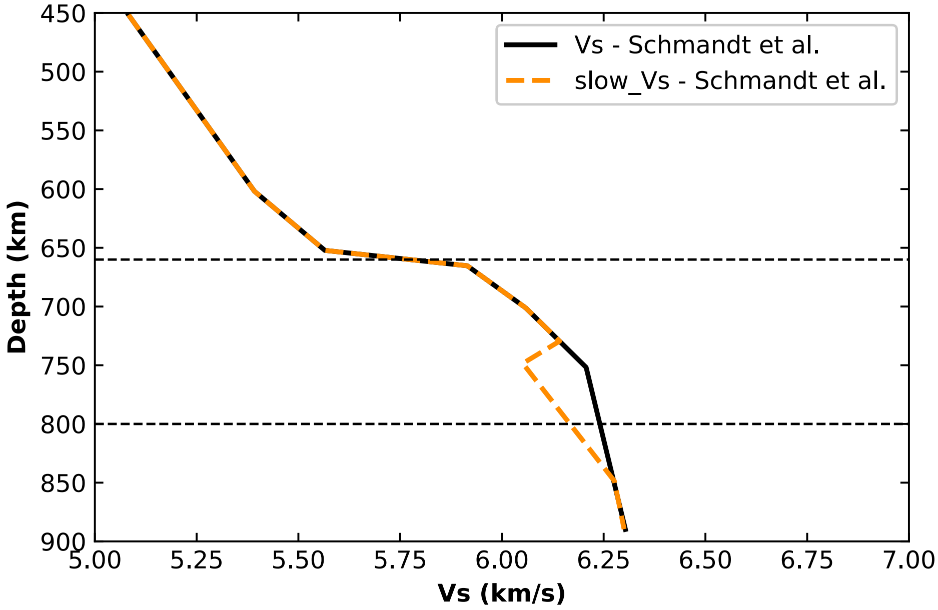

Figure 2.16: Shear velocity profiles observed by Schmandt et al. (2014). Modeled low velocity zone begins at 730 km depth with a maximum at 750 km depth. (*modified from Schmandt et al. (2014)*)

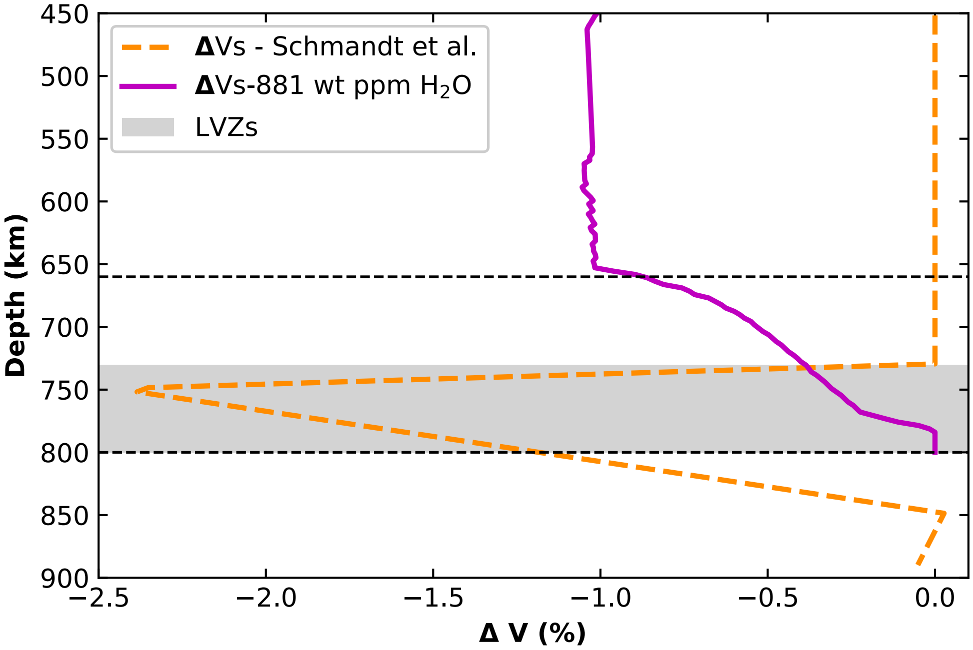

Figure 2.17: Change in shear velocity profiles observed by Schmandt et al. (2014) (*dashed orange line*) and reduction in velocity caused by 881 wt ppm H_2O in garnet (*purple line*). Black dashed lines denote the upper lower mantle (660 km-800 km). Grey region marks depths at which LVZs have been observed (Schmandt et al., 2014; Liu et al., 2016; Zhang et al., 2018; Liu et al., 2018).

Previous studies have suggested the LVZs are produced by dehydration melting induced by water transport out of the transition zone (Schmandt et al., 2014; Liu et al., 2016; Zhang et al. 2018). Our results support this conclusion and suggest garnet is the likely host for water below the TZ. With increasing pressure, water will likely partition from ringwoodite into garnet once ringwoodite decomposes into bridgmanite and ferropericlase. Relative phase proportions are plotted in Figure 2.18 for the relevant depths. At 660 km depth ringwoodite rapidly breaks down leaving garnet as the next most likely host for large amounts of water. In the pyrolite model, garnet then progressively decomposes into bridgmanite and Ca-perovskite and is completely absent below 780 km. If the decomposition of hydrous garnet results in the production of melt at depth, large velocity drops could result.

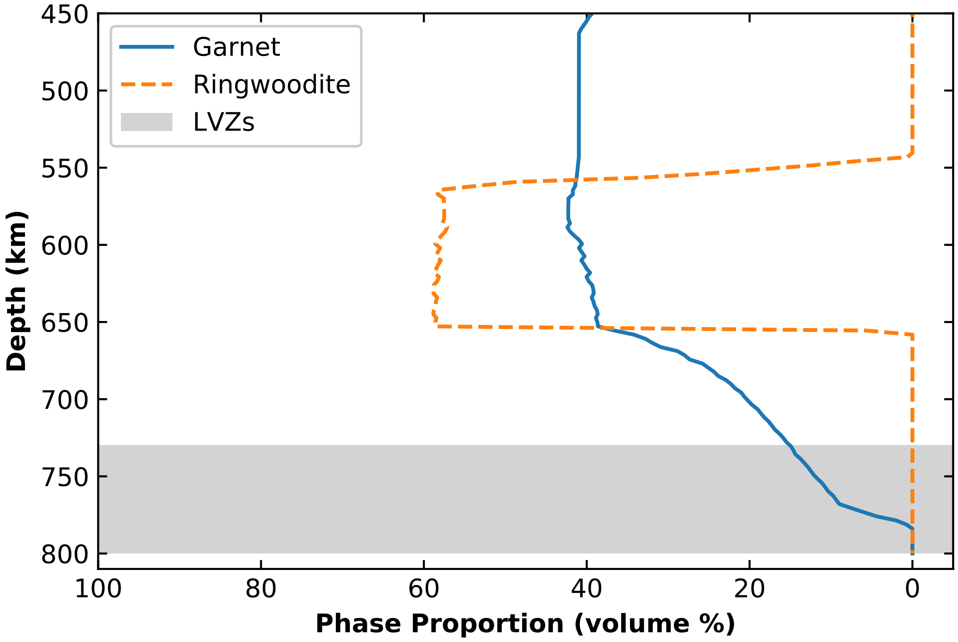

Figure 2.18: Phase proportions of garnet (*blue line*) and ringwoodite (*dashed orange line*) in the mantle. Grey region marks depths at which LVZs have been observed (Schmandt et al., 2014; Liu et al., 2016; Zhang et al., 2018; Liu et al., 2018). Ringwoodite decomposes at 660 km depth while garnet decomposes over the depth range 660 km to 780 km.

Water-storage capacity of the primary mineral phases in the lower mantle, bridgmanite and ferropericlase, have been determined to be ~100 wt ppm H_2O (Bolfan-Casanova, 2005, Panero et al., 2015). The transport of even a few hundred wt ppm of water into the upper lower mantle could cause partial melting if no other phases could incorporate a substantial amount of water. A small amount of melt has the potential to reduce the strength of grain-boundaries and cause a substantial velocity decrease (Yoshino et al., 2007; Hier-Majumder et al., 2014). Using estimates at 400 km depth, Schmandt et al. (2014) suggests 0.68 to 1% melt could explain a 2.6% shear velocity reduction (Hier-Majumder et al., 2011). Estimates of partial melt percentages at depths below 660 km for various quantities of water requires the knowledge of partition coefficients between minerals and melts at relevant P-T conditions. Unfortunately, these coefficients remain unmeasured for the hydrous peridotite system.

2.3.8 Conclusions

We have determined the impact of water on the thermoelastic parameters of majoritic garnet using high-pressure and high-temperature Brillouin spectroscopy. Results show water results in a reduction of bulk modulus and shear modulus at a rate of -0.01 GPa/wt ppm and -0.006 GPa/wt ppm respectively. The addition of hydrous garnet to a dry pyrolitic mantle reduces shear velocities by 0.2 %/wt ppm H_2O. Given the maximum water storage capacity of garnet of ~2000 wt ppm (Thomas et al., 2015), hydrous garnet cannot be the cause of LVZs below 660 km depth. We speculate the production of melt by the dehydration of garnets between 730 km and 800 km depth produces the low velocity structures observed immediately below the mantle transition zone. Alternatively, melt produced at 660 km upon dehydration of ringwoodite may sink until it is neutrally buoyant, which may be near ~750 km where the majoritic-garnet phase is completely replaced by bridgmanite. However, further information on the physical properties of hydrous melts at conditions of 660-800 km is required to further evaluate this alternative hypothesis.

Chapter 3

High-Pressure Phase Transition of Clinoenstatite

This chapter is being prepared for journal submission as:

High-pressure phase transition of clinoenstatite

John D. Lazarz[1], Przemyslaw Dera[2], Yi Hu[2,3], Yu Meng[4], Craig R. Bina[1],

and Steven D. Jacobsen[1]

[1]*Department of Earth and Planetary Sciences, Northwestern University, Evanston, IL 60208, USA*
[2]*Hawaii Institute of Geophysics and Planetology, School of Ocean and Earth Science and Technology, University of Hawai'i at Manoa, Honolulu, HI 96822, USA*
[3]*Department of Geology and Geophysics, School of Ocean and Earth Science and Technology, University of Hawai'i at Manoa, Honolulu, HI 96822, USA*
[4] *HPCAT, Advanced Photon Source, Argonne National Laboratory, Argonne, IL 60439, USA*

3.1 Abstract

Clinoenstatite ($Mg_2Si_2O_6$) undergoes a well-known phase transition from a low-pressure form (LPCEN, space group $P2_1/c$) to a high-pressure form (HPCEN, space group $C2/c$) at ~6 GPa. High-pressure structure refinements of HPCEN were carried out based on single-crystal X-ray diffraction experiments between 9.5 and 35.5 GPa to determine its *P-V* equation of state and structural evolution over an expanded pressure range relevant to pyroxene metatstability. A third-order Birch Murnaghan equation of state was fitted to the compression data resulting in V_0 = 406(1) Å^3, K_{T0} = 103(8) GPa, and K_{T0}' = 5.4(0.6). At ~45 GPa, a transition from HPCEN to a $P2_1/c$-structured polymorph (HPCEN2) was observed, which is clearly related to the $P2_1/c$ structure recently observed in diopside ($CaMgSi_2O_6$) at 50 GPa [Plonka et al. 2012] and in clinoferrosilite ($Fe_2Si_2O_6$) at ~30-36 GPa [Pakhomova et al. 2017]. Observation of HPCEN2 in $Mg_2Si_2O_6$ completes the third apex of the pyroxene quadrilateral wherein HPCEN2 is found, facilitating a broader view of clinopyroxene crystal chemistry at conditions relevant to metastability in the Earth's mantle along cold subduction geotherms.

3.2 Introduction

Pyroxenes are a major component of the Earth's crust and upper mantle, constituting around 25% by volume of the pyrolite model from 100-400 km depth (Ringwood 1977, Akaogi and Akimoto 1977). The components of both orthopyroxene $(Mg,Fe)SiO_3$ and clinopyroxene-$CaMgSi_2O_6$ are incorporated into pyrope and majoritic garnet at depths from 300-500 km, however under the colder conditions along subducting slabs it is possible for metastable pyroxenes to persist deep in the upper mantle (e.g. Hogrefe et al, 1994; Bina et al., 2001; Agrusta et al. 2014; Finkelstein et al. 2014, King et al, 2015). Pyroxenes penetrating the mantle to such depths could potentially undergo further phase transitions impacting subducting slab mineralogy and mantle dynamics. For example, van Mierlo et al. (2013) suggested later transformation to metastable akimotoite.

The major pyroxenes relevant to mafic-ultramafic rocks and the Earth's upper mantle are characterized by single chains of corner-sharing SiO_4 tetrahedra interconnected by MO_6 octahedra containing M cations Mg, Fe, or Ca forming the pyroxene compositional quadrilateral with end members enstatite (En, $Mg_2Si_2O_6$), ferrosilite (Fs, $Fe_2Si_2O_6$), diopside (Di, $MgCaSi_2O_6$), and hedenbergite (Hd, $CaFeSi_2O_6$) (Morimoto et al. 1989). Low-Ca pyroxenes along the En-Fs join are orthorhombic (Pbca), and hence known as orthopyroxenes, whereas Ca-bearing pyroxenes in the quadrilateral are monoclinic and hence called clinopyroxenes (cpx). Ca-rich cpx crystallize in *C2/c* while Ca-poor cpx crystalize in $P2_1/c$.

Orthoenstatite-$Mg_2Si_2O_6$ (OEN) is a major phase of peridotite and was found to transform to a monoclinic, high-pressure clinoenstatite (HPCEN) with space group *C2/c* along a phase boundary corresponding to ~200-250 km depth (e.g. Pacalo and Gasparik 1990 Angel et al. 1992), suggesting that the transformation might be associated with upper-mantle seismic discontinuities, namely the Lehman discontinuity or the X-discontinuity (e.g. Angel et al. 1992; Kung et al. 2004; Ferot et al. 2012; Deuss and Woodhouse 2004; Revenaugh and Jordan, 1991). In experiments, the HPCEN phase quenches to the monoclinic, low-pressure clinoenstatite (LPCEN) with space group $P2_1/c$, which is however rare in nature (e.g. Poldervaart and Hess 1951; Shiraki et al. 1980).

On compression, transformation from LPCEN to HPCEN at 300 K varies from ~6-8 GPa, dependent on Fe-content, water content, and stress (e.g. Ross and Reynard 1999; Jacobsen et al. 2010). With both OEN and LPCEN transforming to HPCEN at pressures below 10 GPa, it has been presumed that HPCEN is the stable phase of $(Mg,Fe)_2Si_2O_6$ below ~250 km depth. The physical properties of HPCEN are not very well known because it is not a quenchable phase, however in-situ sound velocity measurements by Kung et al. (2004) were used to determine its adiabatic bulk modulus, K_{S0} = 156.7(8) GPa and shear modulus, G_0 = 98.5(4). Previous volume-compression studies across the LPCEN-HPCEN transition have estimated the isothermal bulk modulus of HPCEN to be K_{T0} = 118 GPa (Jacobsen et al. 2010) and K_{T0} = 104(6) GPa (Angel and Hugh-Jones, 1994), but these studies relied on very few data points over a very limited pressure range of ~6-8 GPa.

We investigated the volume and structural compression behavior of HPCEN from single-crystal X-ray diffraction measurements at 10-35 GPa. At 45 GPa, we observed a new phase of $Mg_2Si_2O_6$ with space group $P2_1/c$. This phase, a second monoclinic high-pressure clinoenstatite (HPCEN2) is analogous to the same high-pressure clinopyroxene found in clinoferrosilite-$Fe_2Si_2O_6$ at 30-36 GPa (Pakhomova et al. 2017) and in diopside-$CaMgSi_2O_6$ at ~50 GPa (Plonka et al. 2012, Hu et al. 2016), providing further evidence that the HPCEN2 structure is common to phases in the pyroxene quadrilateral. The pressure-compositional dependence of the HPCEN to

HPCEN2 transition has implications for understanding potential pyroxene metastability along cold subduction geotherms and may impact models of slab dynamics.

3.3 Experimental Methods

3.3.1 High-pressure X-ray Diffraction

Synthesis of LPCen single crystals used in this study was described previously (Jacobsen et al. 2010). Briefly, powdered MgO and SiO_2 starting materials were mixed in 1:1 molar proportions and heated at 950 °C for six hours in a flux of V_2O_5, MoO_3, and Li_2CO_3 in molar proportions of 1:7:9. The run products consisted primarily of low-clinoenstatite with minor amounts of orthoenstatite and quartz. LPCen crystals were selected for diffraction experiments using Raman spectroscopy to confirm the presence of the 369 and 431 cm^{-1} vibrational bands, the distinguishing feature from orthoenstatite (Ulmer and Stalder, 2001).

In situ single-crystal X-ray diffraction (XRD) experiments were carried out at HPCAT, Sector 16 experimental station 16ID-B of the Advanced Photon Source (APS), Argonne National Laboratory (ANL). Diamond anvil cell XRD measurements spanned the pressure range 9.5 to 50 GPa. A rhenium metal gasket with initial thickness of 250 μm was pre-indented to ~40 μm using 300 μm culet Bohler-Almax type diamond anvils. Two 30 μm diameter single crystals were loaded into the sample chamber along with two ruby spheres. Differential stresses within the sample chamber were minimized by loading neon as a pressure medium using the GSECARS/COMPRES gas loading system (Rivers et al. 2008). Pressure was determined using the ruby fluorescence method (Mao et al. 1986).

High-pressure diffraction experiments were conducted at experimental station 16ID-B using a monochromatic X-ray beam with wavelength 0.351453 Å, focused with a Kirkpatrick-

Baez mirror system to a spot of 0.005 mm x 0.005 mm. MAR165 charge-coupled device (CCD) detector was placed roughly 170 mm away from the sample, and ambient LaB_6 powder was used to calibrate the distance and tilting of the detector. A total angular opening of the diamond cell of ± 33° was covered during the data collection. A series of step and wide-step ω-exposures were collected. Step scans involved 1° angular increments, while wide-step scans had 16.5° angular increments. The exposure time was at 1 sec/°. After collection of step and wide-step φ-exposures at the zero detector position, more wide-step ω-exposures were recorded with the detector translated perpendicular to the X-ray beam by 70 mm. Exposure time for the off-center detector position was at 2 sec/°.

Diffraction images were analyzed using GSE_ADA and RSV software packages (Dera 2007). Least-squares structure refinements were performed at every pressure point using SHELXL (Sheldrick, 2008).

3.3.2 Density Functional Theory Calculations

In order to obtain some thermodynamic interpretation of the three phases observed in the experiments, we performed a series of crystal structure optimizations and electronic structure calculations using density functional theory (DFT), as implemented in the Vienna Ab Initio Simulation Package (VASP) version 5.4(Kresse and Hafner 1993), controlled by MedeA interface, version 2.22.1. All density functional calculations used the Perdew-Burke-Ernzerhof (PBE) generalized gradient approximation (GGA)(Perdew et al. 1996). The projector augmented wave (PAW) method (Blöchl 1994) was used to treat the core states with a plane wave basis set. The Si 3s2/3p2, O 2s2/2p4 and Mg 3s2 electrons were treated explicitly using the PAW-PBE Si, O and Mg POTCARs, which are available in MedeA. The energy cutoff was set to be 520 eV. The k-point grids were generated using the Γ-centered scheme, with 2 k-points per Å, leading to

2 x 2 x 3 mesh. Temperature effects were not included in the DFT calculations. A similar DFT-based approach has been demonstrated to reasonably well reproduce the phase transition boundaries in the $MgSiO_3$ pyroxene system in earlier studies (Yu and Wentzcovitch, 2009).

3.4 Results and Discussion

Single crystal X-ray diffraction experiments performed between 9.5 and 50 GPa revealed two clinoenstatite phases. The first phase, observed at six pressure points spanning 9.5-35.5 GPa, was successfully indexed using the monoclinic *C2/c* space group. Progression of the unit-cell parameters with pressure (Table 3.1) shows a continuous decreasing trend up to 35.5 GPa. Refined lattice parameters agree well with the previously reported high-pressure clinoenstatite *C2/c* phase (Angel and Hugh-Jones 1994, Shinmei et al. 1999). At 45 GPa clinoenstatite underwent a sudden volume decrease indicating that a first-order phase change occurred between 41.34 and 45 GPa. Data quality from this single pressure point is too low for single-crystal structure refinement, however the lattice parameters and accompanying DFT calculations indicate the transition from HPCEN to HPCEN2 as in diopside (Plonka et al. 2012, Hu et al. 2016) and clinoferrosilite (Pakhomova et al. 2017). Structural evolution of clinoenstatite with pressure is shown in Figure 3.1.

Table 3.1: Lattice parameters of high-pressure clinoenstatite ($Mg_2Si_2O_6$, HPCEN) and HPCEN2 at various pressures.

P (GPa)	Space Group	*a* (Å)	*b* (Å)	*c* (Å)	β (°)	V (Å^3)
9.5(1)	*C2/c*	9.163(2)	8.587(1)	4.875(1)	101.325(1)	376.2(2)
10.4(1)	*C2/c*	9.144(2)	8.5452(9)	4.8807(9)	101.25(2)	374.1(2)
17.0(2)	*C2/c*	8.965(3)	8.443(1)	4.847(1)	100.91(3)	360.3(2)
24.4(2)	*C2/c*	8.871(2)	8.3397(9)	4.7940(9)	100.46(2)	348.8(2)
30.1(3)	*C2/c*	8.804(2)	8.244(1)	4.749(1)	100.31(2)	339.2(2)
35.5(7)	*C2/c*	8.739(3)	8.190(1)	4.714(1)	100.22(2)	332.1(2)

50.2(9)	$P2_1/c$	8.688(2)	7.828(2)	4.5840(9)	100.46(2)	306.6(1)

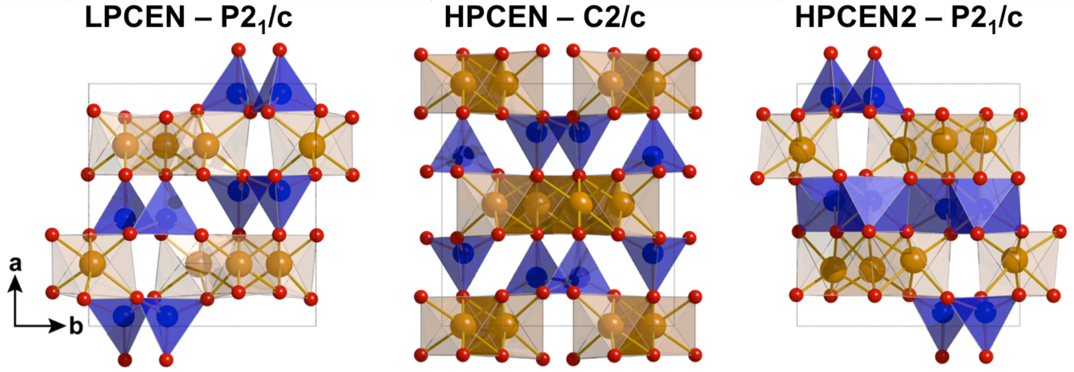

Figure 3.1: The three monoclinic structures of $Mg_2Si_2O_6$ (clinoenstatite): Left, low-pressure clinoenstatite (LPCEN) stable up to ~6 GPa. Middle, the unquenchable high-pressure clinoenstatite (HPCEN) stable at 6-45 GPa. Right, high-pressure clinoenstatite-2 (HPCEN2), observed at ~45 GPa in the current study. The edge-sharing Mg octrahedra are shown in yellow and corner-sharing silica tetrahedra are shown in blue. The HPCEN2 phase features edge-sharing octahedral Si, also shaded blue.

The lattice parameters of HPCEN as a function of pressure (Table 3.1) were fitted to a third-order Birch-Murnaghan equation of state. The HPCEN-*C2/c* reference volume (V_0) was refined during the least-squares fitting procedure because HPCEN-*C2/c* is unquenchable (Angel et al. 1992, Ross and Reynard 1999). Fitting was performed using the Burnman Python library (Cottaar et al. 2014). Our refined V_0 of 406 (1) Å^3 agrees well with previously reported values of 405 (2) Å^3 (Shinmei et al. 1999), 406(1) Å^3 (Angel and Hugh-Jones 1994), and 403.95 Å^3 (Jacobsen et al. 2010).

A merged P-V data set was used for equation of state fitting. Negative pressure extrapolation from 9.5 GPa to room pressure leads to large experimental uncertainties in equation of state parameters. As a result we have performed the fitting with a merged data set consisting of our 9.5-35.5 GPa compression data and Angel and Hugh-Jones (1994) HPCEN-*C2/c* compression data. A single third-order Birch-Murnaghan equation of state fitted to the merged data set has the parameters V_0 = 406(1) Å^3, K_{T0} = 103(8) GPa, and K_{T0}' = 5.4(6). The fitted HPCEN-*C2/c* phase equation of state and volume compression data can be seen in Figure 3.2. We selected the third-order truncation of the Birch-Murnaghan EoS, to fit our P-V data, based on the normalized stress, $F_E = P/3f_E(1+2f_E)^{5/2}$, vs. Eulerian finite strain, $f_E = [(V_0/V)^{2/3} - 1]/2$, positive linear inclination. From the intercept and slope of a linear fit to the F_E- f_E plot, Figure 3.3, we obtain K_{T0} = 103 GPa and K_{T0}' = 5.4, both in excellent agreement with the calculated fit. This result reinforces the conclusion that our data are well described by a third-order Birch-Murnaghan EoS.

A comparison of equation of state parameters for HPCen-*C2/c* with published data can be seen in Table 3.2. While reported values fall primarily within the estimated standard deviations of our results, when taking the covariance from the fit of our P-V data into account we notice the reported K_{T0}' from Angel and Hugh-Jones (1994) is inconsistent with our P-V data (Figure 3.4). This can be attributed to their fixing of K_{T0}' to 6.6, the K_{T0}' value obtained for their LPCen, during equation of state refinement. To a 3σ (99.7%) confidence level, published parameters agree well with our results.

Table 3.2: Equation of state parameters for high-pressure clinoenstatite (HPCEN).

P-range (GPa)	V_0 (Å^3)	K_{T0} (GPa)	K_{T0}' (GPa)	ρ_0 (g/cm^3)	Reference
9.5 - 35.5	406(1)	103(8)	5.4(6)	3.28(1)	This study
7.1 - 8.06	404	118	6.1	3.302	Jacobsen et al. (2010)
4.0 - 10.7	405(2)	106(17)	5(3)	3.292(14)	Shinmei et al. (1999)
5.3 - 8.0	406(1)	104(6)	6.6*	3.288(9)	Angel and Hugh-Jones (1994)

*Fixed during refinement.

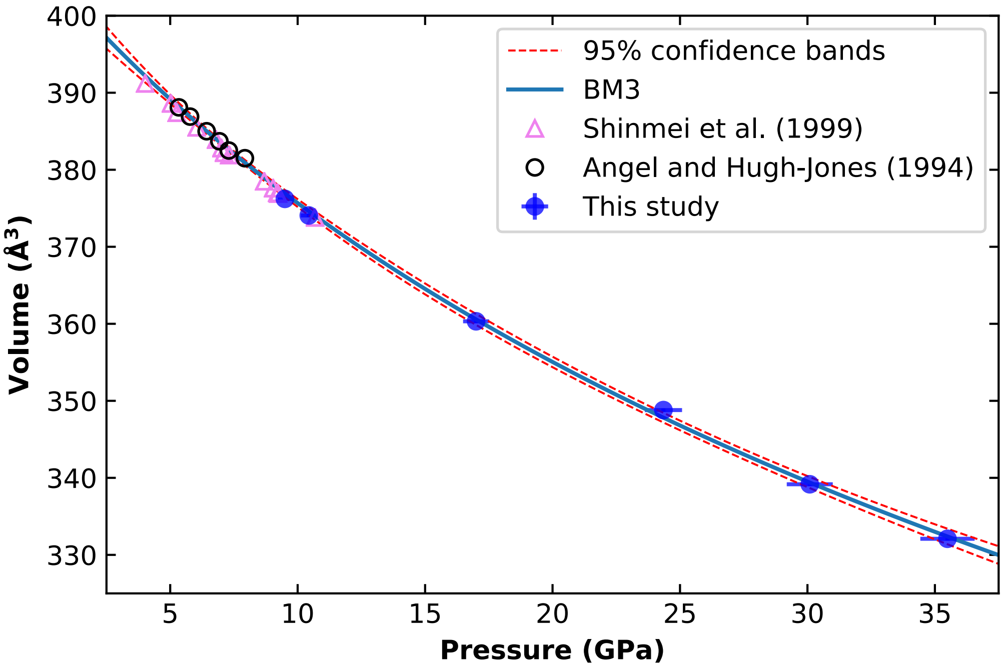

Figure 3.2: Comparison of variation in unit-cell volume as a function of pressure in anhydrous $MgSiO_3$ high-pressure clinoenstatite. Third-order Birch-Murnaghan equation of state for the solid blue curve is given in Table 3.2.

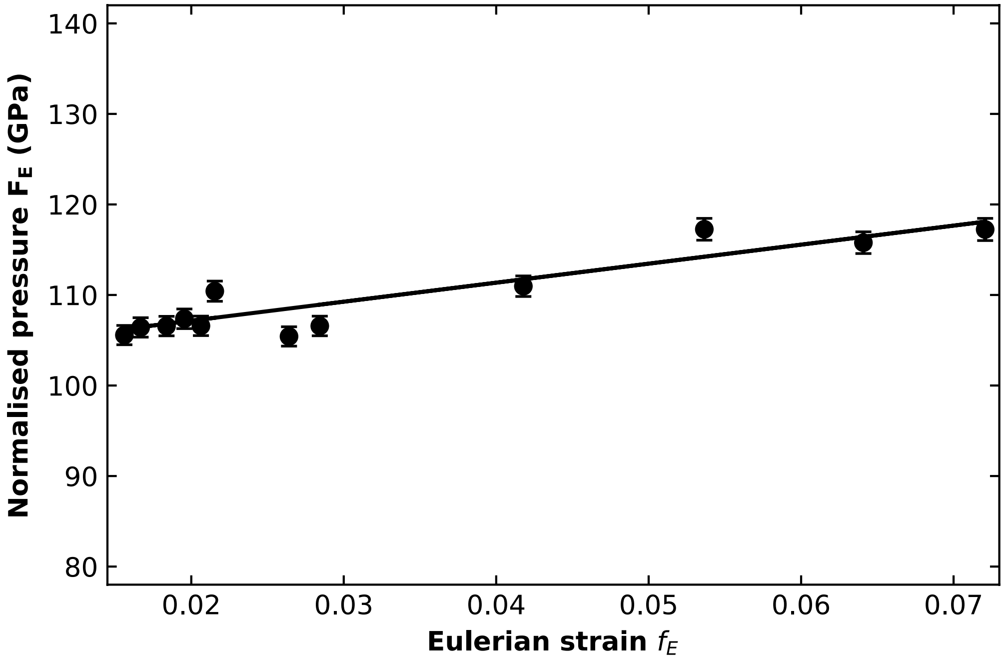

Figure 3.3: Normalized stress F_E vs. the Eulerian strain f_E for HPCEN

A strong indicator of a change in compression mechanism is anisotropy in axial compressibility. The variation in linear dimension, *l*, of a material can be expressed as linear compressibility, defined as $\beta_l = (-l)^{-1}(\delta l/\delta P)$. For linear parameters such as *a*, *b*, *c* we can assess their compressibility by treating the cube of each parameter as volume in a Birch-Murnaghan EoS fitting procedure (Angel et al. 2014). The choice of EoS order was again made based on the F_E - f_E plot. A horizontal linear fit to the F_E - f_E plot for all unit-cell parameters prompted our selection of a second-order Birch-Murnaghan equation of state, K_{T0}' = 4. For HPCEN-*C2/c*, our fitted linear moduli to *a*, *b*, *c*, and *a*sinβ are 99(3), 101(2), 158(7), and 115(4) GPa, respectively. Subsequent axial compressibility values are $\beta_a = 10.1(3) \times 10^{-3}$, $\beta_b = 9.9(2) \times 10^{-3}$, $\beta_c = 6.3(3) \times 10^{-3}$, $\beta_{a\sin\beta} = 8.7(3) \times 10^{-3}$ GPa^{-1}.

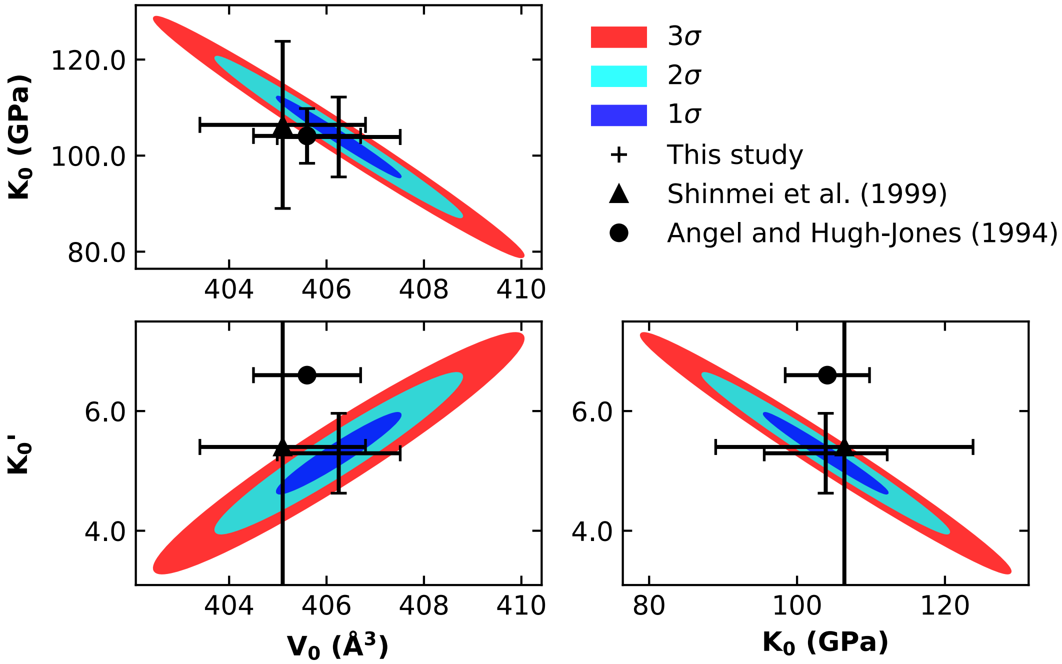

Figure 3.4: Confidence ellipse in isothermal equation of state parameters for third-order Birch-Murnaghan equation of state. Note that the limits of the error bars correspond to 1 estimated standard deviation (*esd*). Previously reported results match well with those reported here, except for the reported K_{T0}' from Angel and Hugh-Jones (1994). This is most likely a consequence of their fixing K_{T0}' to 6.6 during the fitting procedure.

Volume and axial compression of our HPCEN-*C2/c*, as compared to pyroxene phases belonging to the hedenbergite-diopside-ferrosilite-enstatite, $CaFeSi_2O_6$-$MgCaSi_2O_6$-$Fe_2Si_2O_6$-$Mg_2Si_2O_6$, quadrilateral system (Morimoto et al. 1989) are plotted in Figure 3.5. The evolution of HPCEN-*C2/c* lattice parameters with pressure differs slightly from that of other familial pyroxenes. Clinopyroxenes tend to follow the characteristic axial compressibility scheme $\beta_b > \beta_c \approx \beta_a > \beta_{a\sin\beta}$ (Angel and Hugh-Jones 1994; Nestola et al. 2004; Pakhomova et al. 2017; Tribaudino et al. 2001; Hu et al. 2015) however, our results show HPCEN-*C2/c* follows the axial compressibility scheme $\beta_a \approx \beta_b > \beta_{a\sin\beta} > \beta_c$.

Normalized unit-cell parameters of HPCEN-*C2/c* as a function of pressure calculated as X_P/X_0, where X_P = experimentally determined parameters *a*, *b*, *c*, and *a*sinβ at pressure point P and X_0 = values from EoS at ambient pressure, are shown in Figure 3.6. With an exception for a minor detour in the stiffness of *a* beginning around 12 GPa, each axial direction maintains a steady compression trend relative to the other parameters. In our observed compression scheme the decrease in volume between 9.5 and 35.5 GPa is due primarily to compression of the *a* and *b* axis while the stiffer *a*sinβ and *c* directions contract relatively little. The different anisotropy scheme of the HPCEN-*C2/c* phase with respect to other pyroxenes is a reflection of a change in compression mechanism.

Within the quadrilateral family, the *b* dimension is unique with the magnitudes remaining relatively clustered and showing similar compressibilitys throughout the observed pressure range. This observation breaks down for the other lattice parameters *a*, *c*, and β. Quadrilateral pyroxenes differ with lattice parameter *a* being the shortest of the group and stiffest direction for HPCEN-*C2/c*. Lattice parameters are also dispersed in magnitude for *c* and β.

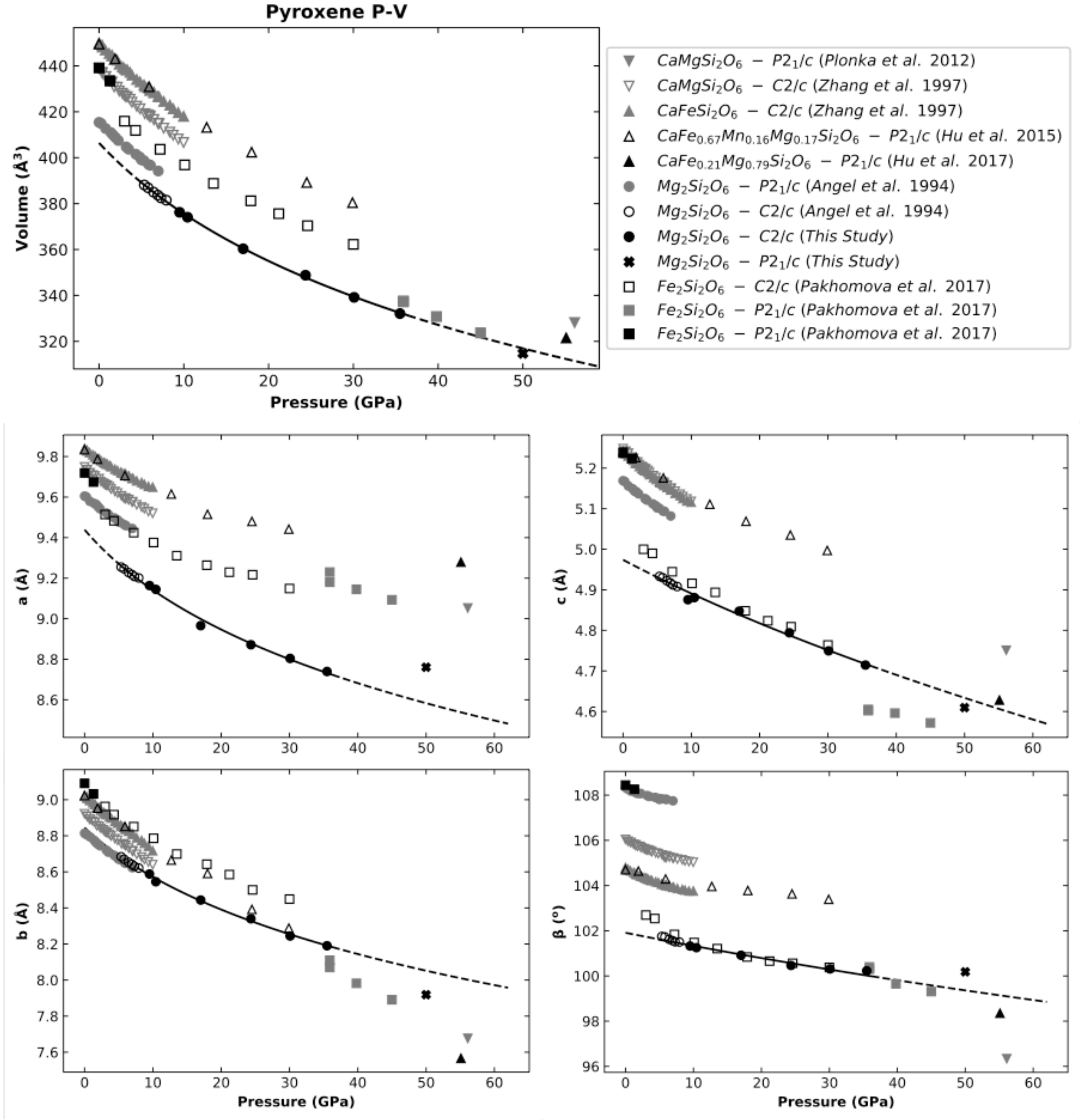

Figure 3.5: Compression data for phases within the hedenbergite-diopside-ferrosilite-enstatite quadrilateral. Solid line represents the Birch-Murnaghan EoS fits to the current experimental data for HPCEN, extrapolated beyond the data points with dashes.

Compression behavior of HPCEN-*C2/c* does not agree particularly well with any member of the quadrilateral, but agrees best with *C2/c*-clinoferrosilite. Over the observed pressure range evolution of *C2/c*-clinoferrosilite lattice parameters *c* and β agree remarkably well with those of HPCEN-*C2/c*.

3.5 HPCEN-*C2/c* High Pressure Structure Behavior

Refinement of structure data obtained from six pressure points between 9.5 and 35.5 GPa shows the crystal maintained a *C2/c* space group symmetry throughout the pressure range. The structure of the HPCEN-*C2/c* phase is composed of three distinct polyhedra: one Si1O_4 tetrahedron and two octahedra, Mg1O_6 and Mg2O_6. The Si1 site is bonded to four oxygen atoms: O1, O2, O3A, and O3B. The bridging O3 atoms connect strings of Si tetrahedral running parallel to the *c* crystallographic axis. The extremely kinked O-rotated Si tetrahedral chain is a distinguishing feature of the HPCEN-*C2/c* phase. The O3-O3-O3 bond angle, a measure of rotation of individual Si tetrahedral, displays a decreasing trend with increasing pressure as seen in Figure 3.7. As the *c* axis shortens with increasing pressure the Si tetrahedra rotate forcing the O3-O3-O3 angle to decrease by 2% over the observed pressure range as the chain becomes increasingly kinked. The Si tetrahedra are non-ideal, with Si1-O bond lengths ranging from 1.569(2) Å (Si1-O2) to 1.666(2) Å (Si1-O3B) at 9.5 GPa. Quadratic elongation and angular variation, measures of polyhedral ideality, are 1.0043 and 17.75°, respectively, at 9.5 GPa. The Mg1 atom, occupying the M1 site, sits at the center of the first of two MgO_6 octahedra. Mg1 forms 3 unique bonds with O: Mg1-O1A, Mg1-O1B, and Mg1-O2. The Mg-O1A bonds are the longest of the three with a length of 2.001(2) Å the Mg1-O1B and O2 bond lengths are 2.07(2) and 1.989(2) Å, respectively, at 9.5 GPa. The quadratic elongation and angular variation are 1.0059 and 19.18°. The M1 octahedra are edge-sharing along the O1B-O1B edge. Mg2 forms three unique bonds: Mg2-O1, Mg2-O2, and Mg2-O3. In the more distorted M2 octahedra the Mg2-O3 bond is the longest at 2.170(2) Å while Mg2-O1 = 2.068(2) Å and Mg2-O2 = 1.977(2) Å. The quadratic elongation and angular variation for the M2 site are 1.0097 and 25.82°.

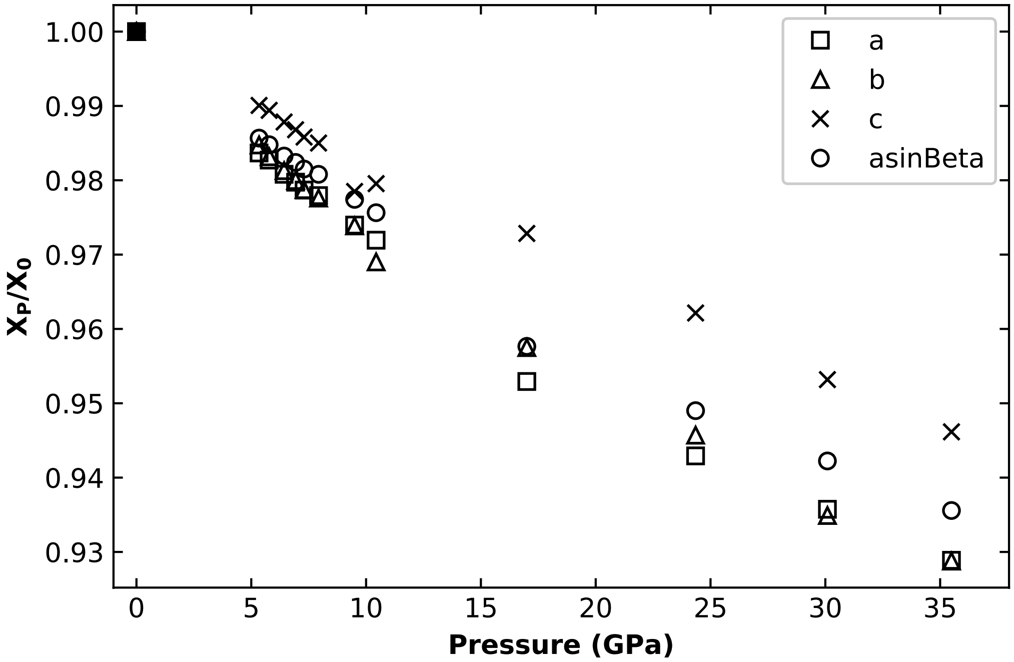

Figure 3.6: Normalized unit-cell parameters of HPCEN (*C2/c*).

The HPCEN-*C2/c* structure refinements show the SiO_4 tetrahedra remain relatively incompressible compared to the MgO_6 octahedra. Mg1 and Mg2 octahedra show a 13.8% and 15.9% volume reduction over the pressure range 9.5 to 35.5 GPa, respectively, while Si tetrahedra show only a 4.7% volume reduction. Octahedral and tetrahedral volumes as a function of pressure as well as polyhedral compressibility determined by a second-order Birch-Murnaghan equation of state can be seen in Figure 3.8. The HPCEN-2 polyhedra follow the $\beta_{Mg2} = 14.3(1) \times 10^{-3} > \beta_{M1} = 10.3(7) \times 10^{-3} > \beta_{Si1} = 2.0(5) \times 10^{-3}$ GPa^{-1} scheme.

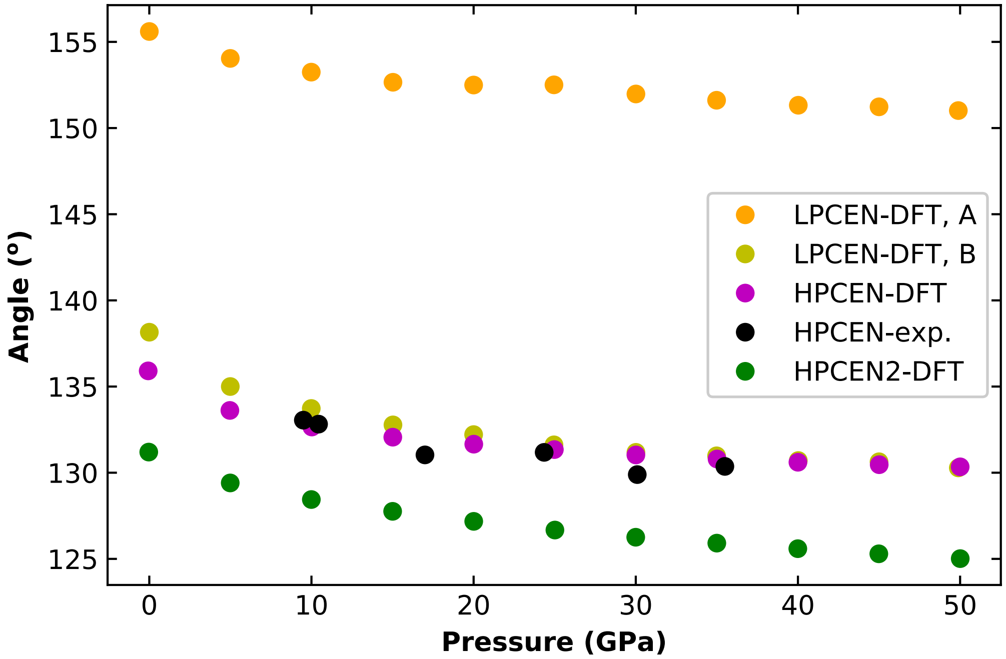

Figure 3.7: $Mg_2Si_2O_6$ O3-O3-O3 kinking angle as a function of pressure.

Within the relatively compressible Mg2 octahedra the Mg1-O2 is the most compressible with $\beta_{Mg1\text{-}O2} = 11.7(7) \times 10^{-3}$, $\beta_{Mg1\text{-}O1A} = 5.9(8) \times 10^{-3}$ GPa^{-1}, and the edge-sharing Mg1-O1B is the stiffest bond $\beta_{Mg1\text{-}O1B} = 5.7(9) \times 10^{-3}$ GPa^{-1}. The deformed Mg2 octahedra bond compressibility's are $\beta_{Mg2\text{-}O3} = 39.7(6) \times 10^{-3}$, $\beta_{Mg1\text{-}O2} = 11.7(8) \times 10^{-3}$, $\beta_{Mg1\text{-}O1} = 11(1) \times 10^{-3}$ GPa^{-1}. The high compressibility of the M2 octahedra, specifically the soft Mg2-O3 bond, accommodates much of the volume reduction over the observed pressure range. The compressed Mg octahedra, relative to the Si1 tetrahedra, allow for the rotation of Si tetrahedra from S-rotated to O-rotated chains during the LPCEN to HPCEN phase transition, occurring between 6.5 and 7.1 GPa (Jacobsen et al. 2010, Angel et al. 1992). As pressure continues to increase the Mg octahedra continue to compress, further accommodating the overall volume reduction.

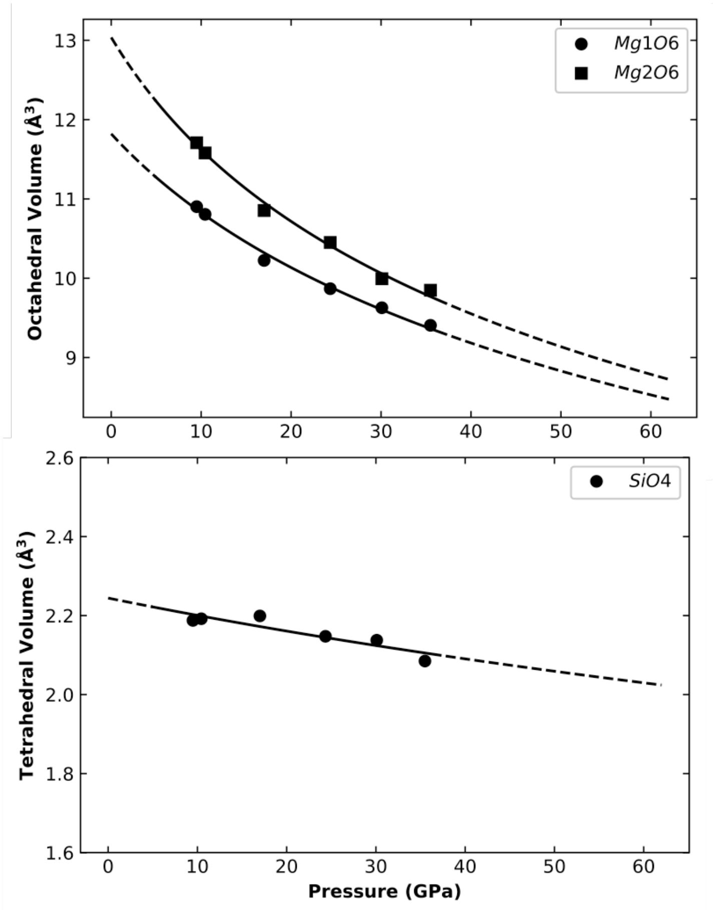

Figure 3.8: Pressure-volume trends of octahedral (Mg) and tetrahedral (Si) sites in HPCEN in *C2/c*. Solid lines represent the second-order Birch-Murnaghan EoS fits.

The Si1 tetrahedra are far less compressible than the M octahedral, with a bulk modulus five times that of the M1 octahedra. The softest bond in the Si1 tetrahedra has a compressibility $\beta_{Si1\text{-}O1} = 3.4(4) \times 10^{-3}$ GPa^{-1} and the least compressible bond is the Si1-O2 bond with a compressibility of $\beta_{Si1\text{-}O1} = 0.6(2) \times 10^{-3}$ GPa^{-1}. Given the stiffness of the Si1 tetrahedra, the majority of the deformation in the tetrahedral chain is absorbed by the shrinking O3-O3-O3 bond angle. Overall compression of the HPCEN-*C2/c* unit-cell with pressure can then be summarized as being governed by the compression of Mg octahedra, primarily on the M2 site, and rotation of Si1 tetrahedra decreasing the O3-O3-O3 bond angle.

Unlike in the orthopyroxene system, we do not find a significant increase in stiffness with increasing Ca^{2+} substitution into the M2 octahedral site. Hugh-Jones and Angel (1997) observed an increase in K_{T0} of 14% with the substitution of very small amounts of Ca^{2+} into the M2 site. However, in comparison with the results of Tribaudino et al. (2000) who examined the high-pressure behavior of Ca-rich HPCEN up to 35.5 GPa, we only notice a difference of 2.7% in K_{T0} between the two end members. This promotes the validity of the use of pure end-member $MgSiO_3$ as a representative pyroxene in the Earth's upper mantle, within the diopside-enstatite solid solution.

The stability of the *C2/c* phase may become significant when considering slab mineralogy and morphology. Our in situ X-ray diffraction experiment shows that anhydrous low-Ca HPCEN has a high level of stability at room temperature to pressures corresponding to a depth of approximately 1050 km. Similarly, the diopside end member of the diopside-enstatite solid solution displays a continuous compression trend up to 45.6 GPa (Plonka et al. 2012, Tribaudino et al. 2000). At 1650 °C, nearly all clinopyroxenes transform to garnet by 20 GPa (Gasparik 1989). However, it has recently been shown that the pyroxene-garnet transformation can be significantly inhibited at low temperature (<1550°C) (Nishi et al. 2008). Pyroxenes subducted into the mantle by cold downwelling slabs could potentially be kept below temperatures of 1500 °C down to depths of ~1200 km (Bina et al. 2001). Further studies will be needed to constrain the transformation temperatures of HPCEN at high pressure as well as the implications of maintaining this metastable mineralogy to the respective depth.

3.6 HPCEN-*C2/c* to HPCEN2-$P2_1/c$ phase transition

After 35.5 GPa HPCEN undergoes a second first-order phase transition to a HPCEN-$P2_1/c$ phase. Data quality from our single pressure point is too low to report a structure refinement. However, in strong agreement with our observations, our DFT calculations predict a phase transition to a $P2_1/c$ phase at 35 GPa (Figure 9). Lattice parameters from our DFT calculations are compared to observations in Table 3.3.

Table 3.3: Coefficients obtained from fitting a Birch-Murnaghan EoS.

	LPCEN - DFT	HPCEN - exp.a	HPCEN- DFT	HPCEN2 - exp.b	HPCEN2 - DFT
	$P2_1/c$	*C2/c*	*C2/c*	$P2_1/c$	$P2_1/c$
a_0 (Å)	9.7271	9.4389	9.5082	-	9.4665
a_{50}	9.0531	8.5831	8.7533	8.688(2)	8.7605
b_0 (Å)	8.9233	8.8450	8.9345	-	8.4573
b_{50}	8.0766	8.0519	8.1040	7.828(1)	7.9189
c_0 (Å)	5.2224	4.9739	5.0535	-	4.9209
c_{50}	4.8182	4.6336	4.6982	4.5840(9)	4.6096
β_0 (°)	108.46	101.91	102.89	-	98.08
β_{50}	107.65	99.36	99.86	100.46(2)	100.18
V_0 (Å^3)	429.96	406(1)	418.47	-	390.06
V_{50}	335.71	316.92	328.36	306.6(1)	314.74
K_{T0} (GPa)	107(1)	103(8)	106(2)	-	138(1)
K_0' (GPa)	5.1(1)	5.3(7)	5.6(2)	-	4.89(9)
ρ_0 (g/cm^3)	3.102	3.28(1)	3.187	-	3.419
ρ_{50}	3.972	4.208	4.063	4.350	4.237

[a] Parameters from extrapolation of equation of state. $_{50}$ at 50 GPa

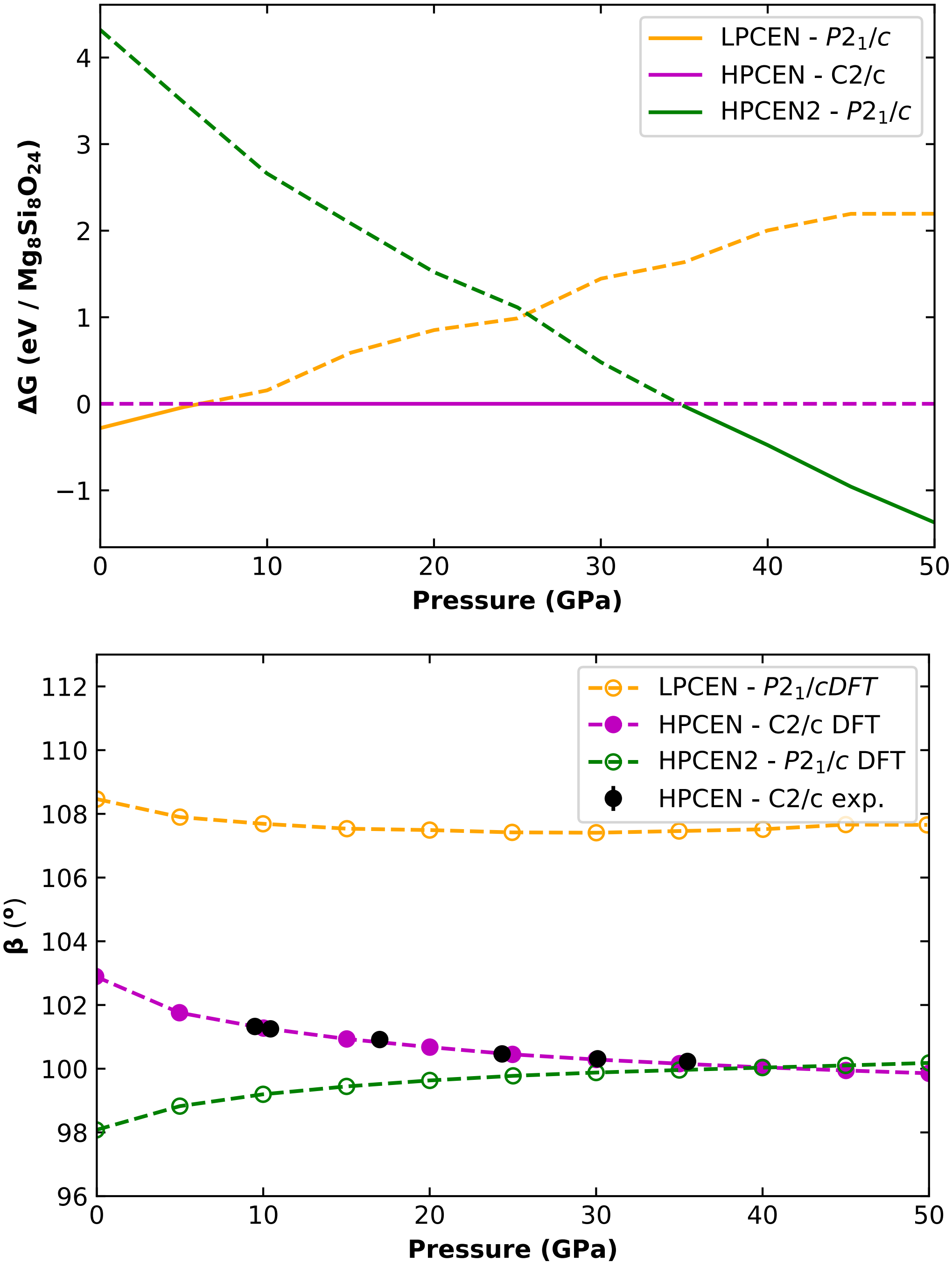

Figure 3.9: Density functional theory (DFT) results for the $Mg_8Si_8O_{24}$ system. (top) Change in Gibbs free energy was calculated to determine phase transition pressures for clinoenstatite. (bottom) Experimental measurements agree well with calculated structure parameters.

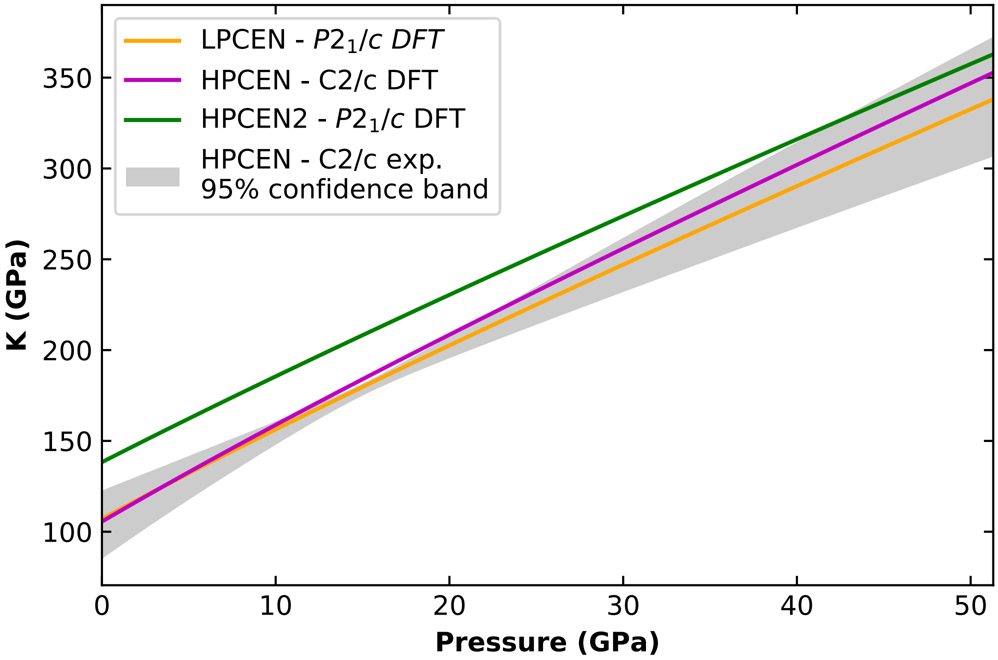

Figure 3.10: Isothermal bulk modulus (K) for high pressure clinoenstatite using refined parameters from this study in Table 2. DFT results agree well with experimentally determined bulk modulus.

Three phases were considered in the DFT calculations: LPCEN, HPCEN and HPCEN2. Starting models for structure optimizations were taken from the crystallographic refinements performed in this study at 0 GPa for LPCEN, 10.4 GPa for HPCEN, and for HPCEN2 we adopted the $P2_1/c$ high pressure clinoferrosilite model reported by (Pakhomova et al. 2017). Structures of all three phases were fully optimized (all unit cell parameters and fractional atomic coordinates) at a set of fixed external pressures from 0 GPa to 50 GPa, with 5 GPa intervals. The GGA approximation is known to overestimate both the unit cell parameters, as well as the phase transition pressures; however, as reported in Table 3.3, we obtained a reasonably good agreement with experimental results.

Our calculations predict that at 0K the HPCEN structure becomes energetically favorable over the LPCEN structure at about 5 GPa, which is consistent with experimental observations. The transformation from HPCEN to HPCEN2 is predicted at approximately 35 GPa, which is a little lower than the experimental observation (45 GPa), but reasonable for the GGA approximation.

3.7 Conclusions

High-pressure clinoenstatite displays a continuous compression trend maintaining its monoclinic *C2/c* symmetry throughout the pressure region 9.5-35.5 GPa. By using *in situ* X-ray diffraction and diamond anvil cells to compress single crystal clinoenstatite up to 50 GPa this study expands the understanding of Ca-poor clinopyroxene compression mechanisms and elasticity. Our EOS extends the pressure range covered by published equations of state by 25 GPa and our refined parameters $V_0 = 406(1)$ Å^3 , $K_{T0} = 103(8)$ GPa, and $K_{T0}' = 5.4(6)$ are in agreement with previously reported results. We have observed a new clinoenstatite phase transition between 41.34 and 45 GPa from a *C2/c* symmetry to $P2_1/c$. Density functional theory supports our structural analysis of this new phase. These results have implications for the potential metastability of clinopyroxenes to depths greater than 1000 km in deep cold subduction zones.

Chapter 4

Optical Properties of Acetaminophen and Assessment of Structure-Property Effects of Impurities by Refractometry

This chapter is being prepared for journal submission as:

Optical properties of Acetaminophen and Assemssment of Structure-Property Effects of Impurities by Refractometry

John D. Lazarz[1], Cindy A. Bolme[2], Steven D. Jacobsen[1], and Kyle J. Ramos[2]

[1]*Northwestern University, Department of Earth and Planetary Sciences, Evanston IL USA*
[2]*Shock and Detonation Physics, Los Alamos National Laboratory, Los Alamos, NM USA 87545*

4.1 Abstract

We report the principal indices of refraction for the biaxial indicatrix of monoclinic acetaminophen or p-hydroxyacetanilide (PHA form I) including chromatic dispersion between 400 and 800 nm. Euhedral crystals measuring up to 1 cm in longest dimension were grown from solvent by evaporation and/or slow cooling of solutions with and without the synthetic impurity p-acetoxyacetanilide (PAA). The indicatrix was determined using the Becke line method on single crystals oriented along the principal optical axes located using a polarization extinction method under orthoscopic examination on a universal stage. For crystals grown from solution without PAA added, the principal indices of refraction at 532 nm are 1.590(1), 1.652(1), and 1.719(1), for n_a, n_b, and n_g, respectively, resulting in a birefringence value of 0.129. The results are identical within error for a crystal grown with 200 mg PHA but are inconclusive because of the limitation of three decimal place precision. Chromatic dispersion between 430 and 740 nm is represented by the following Cauchy constants: for n_a, 1.551(3), 1.055(2), and 0.0002(3); for n_b, 1.609(6), 1.039(4), and 0.0004(5); and for n_g, 1.645(5), 1.998(3), and 0.0002(4). Reflection goniometry was used to determine the optic orientation for PHA form I in the monoclinic-*b* setting, wherein the X-axis of the biaxial indicatrix (n_a) lies along the *b*-crystallographic axis and the indicatrix Z-axis (n_γ) forms an angle of 35.04° with {10-1}.

4.2 Introduction

Acetaminophen, p-hydroxyacetanilide (PHA), also known as paracetamol, is among the most common and prototypical over-the-counter pharmaceuticals used worldwide as an effective analgesic and antipyretic (Anderson, 2008; Toms et al., 2008; Ong et al., 2010). Whereas many physical properties of acetaminophen are well known, its single-crystal elastic properties, which will be useful in modeling multi-phase compression in alternative binders in the tableting process, have not been determined. As a first step towards determining the elastic tensor of acetaminophen from Brillouin scattering, the complete optical indicatrix, or second-rank tensor of principal refractive indices is required.

Jordan (1993) reported principal indices of refraction, n_a, n_b, and n_g, and a qualitative estimation of the angle between optic axes (2V) for acetaminophen using a sodium lamp (~589 nm). Subsequently, Nichols (1998) published the refractive indices of form I (monoclinic) and form II (orthorhombic) acetaminophen, also at 589 nm. The results from Nichols (1998) generally agree with reported refractive indices Jordan (1993); however, the effects of chromatic dispersion on extinction angle were noted without complete characterization. Here we present the principal components of refractive index for acetaminophen form I from 400-800 nm.

Optical properties are sensitive to crystal structure as well as impurities. As a result, polarized microscopy is ideal for rapid sample screening. As noted by Nichols and Frampton (1998), monoclinic acetaminophen displays dispersed extinction while orthorhombic acetaminophen does not. Given a batch of crystals and a polarizing-light microscope, it is possible to quickly separate the two forms. While optical properties are useful for rapid sample screening, they are also a fundamental physical property of any crystal. The index of refraction

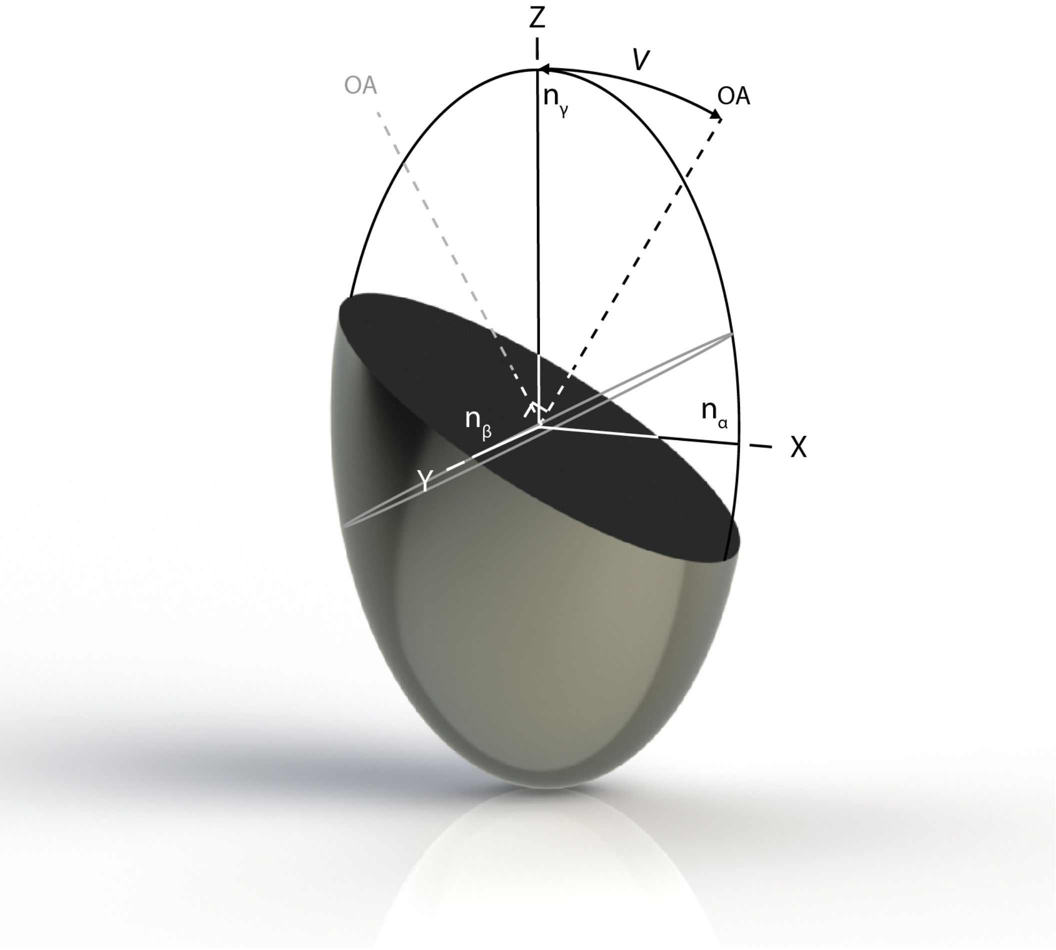

Figure 4.1: Illustration of the biaxial indicatrix where X, Y, and Z are axes of the indicatrix, n_a, n_b, and n_g represent the magnitude of principal indices of refraction, and V is the angle between the optic axis and Z. The optic axes are labeled OA.

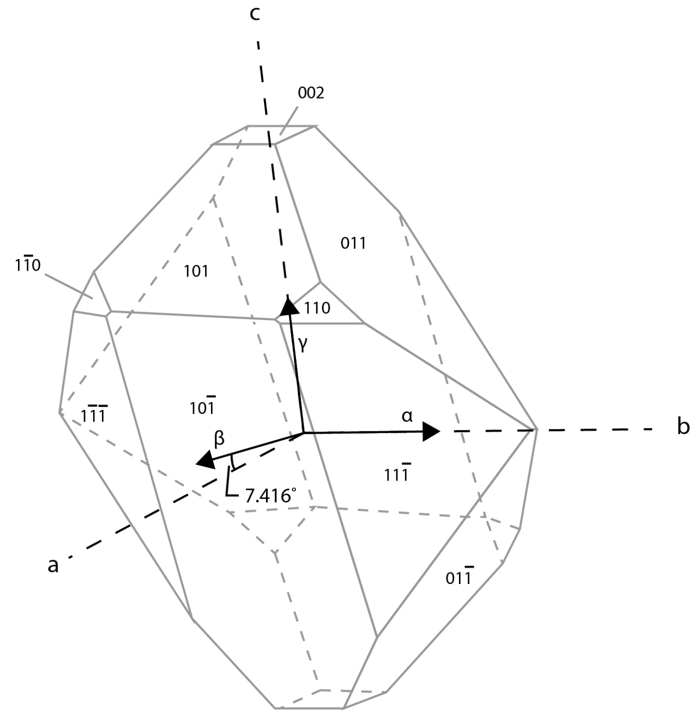

Figure 4.2: Illustration of the monoclinic form acetaminophen morphology and crystallographic axes (a, b, c) with respect to the orientation of the optic axes determined in this study. (figure modified from Nichols (1998))

and polarization of light passing through a monoclinic crystal in any direction is represented by a biaxial ellipsoid, commonly referred to as an optical indicatrix, illustrated in Figure 4.1.

The indicatrix is constructed such that the length of each vector from the origin to the surface of the ellipsoid is equal to the index of refraction. The three orthogonal ellipsoid axes, X, Y, and Z, lie in the directions of the principal indices of refraction: n_α, n_β, n_γ. By convention $n_\alpha < n_\beta < n_\gamma$. The acute angle between the optical axes is referred to as 2V. With knowledge of the three components, n_α, n_β, n_γ, the complete indicatrix can be resolved. Commonly, 2V is calculated using Equation 4.1.

$$\cos^2 V = \frac{n_\alpha^2\left(n_\gamma^2 - n_\beta^2\right)}{n_\beta^2\left(n_\gamma^2 - n_\alpha^2\right)} \qquad [4.1]$$

Optically biaxial materials are defined as those having two optic axes. Each optical axis lies normal to one of the two unique circular cross sections of the indicatrix ellipsoid, which exhibit no birefringence (Figure 4.1). In monoclinic crystals such as acetaminophen form I, following the β-unique convention, one of the indicatrix principal axes coincides with the *b* crystallographic axis while the remaining two form an angle with the *a* and *c* axes.

Ambiguity exists with respect to the the optical indicatrix orientation reported by Nichols (1998). While it is explicitly stated that they found n_α to lie coaxial to the b crystallographic axis, the presented figures are difficult to interpret. For such optically anisotropic materials, when making elasticity measurements knowledge of orientation is critical for accurate elastic tensor determination (Bolme and Ramos, 2014). Sample orientation methods must be chosen carefully in order to prevent the accumulation of large systematic errors. In the particular method, used by Nichols (1998), single crystals on the order of 250 μm in size were placed on slides such that index measurements could be made. Using the technique with loose crystals may result in orientation error. Crystals were balanced on small habit or fracture surfaces where orientation was assumed, whereas a spindle stage was used here to allow for mounted crystals of known orientation to be analyzed.

The intent of this study was to *i)* independently verify the first and only complete optical characterization of acetaminophen (i.e. refractive indices and crystallographic orientation of principal optic axes), *ii)* measure chromatic dispersion of the principal refractive indices, *iii)* define the optic orientation with Euler angles, and *iv)* and assess the effects of impurities on optical properties.

4.3 Experimental

4.3.1 Materials

Acetaminophen crystals were grown by solvent evaporation and/or slow cooling. Details of the solvent composition for each batch number are provided in Table 4.1. Samples were verified as form I acetaminophen via morphology inspection, measurement of interplanar angles by reflection goniometry, X-ray diffraction, as well as analysis of single crystal extinction under crossed polarizers. Monoclinic, form I, acetaminophen tends to display platelet or prismatic morphology while orthorhombic, form II, crystals tend to be elongated along the c-axis. Unlike form II acetaminophen, form I shows incomplete dispersed extinction when viewed along the b-axis (Nichols, 1998). A representative crystal from batch acet-8 is shown in Figure 4.3.

Lattice parameters of acetaminophen crystals from four different batches were determined by single-crystal X-ray diffraction data collected on a custom-built Huber four-circle diffractometer with sealed-tube Mo ka radiation and a crystal-detector distance of about 40 cm.

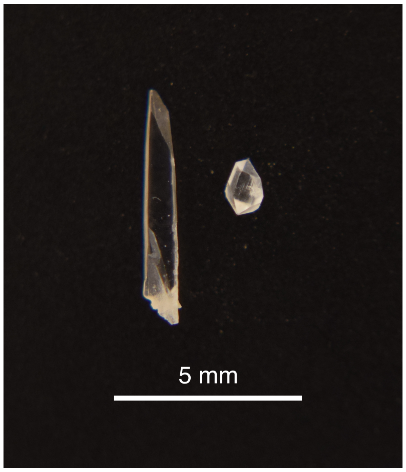

Figure 4.3: Photomicrograph of a euhedral acetaminophen crystals grown in the current study. (left) Single crystal form I acetaminophen grown in 200 mg PHa solution compared to (right) impurity free single crystal form I acetaminophen.

For one crystal from each batch, we centered 47 reflections using the method of 8-position centering (King and Finger, 1979), where every unique *hkl* is centered with rocking curves (w scans) in all four equivalent positions, first in positive 2θ and again at negative 2θ positions, resulting in eight rocking curves for each *hkl*. This method provides very high precision in determined lattice parameters of a few parts in 10^4 by minimizing crystal offsets from the center point of the goniometer and zero-point errors in the 2θ, w, and c axes. Full profile peak fitting was carried out using the program Single (Angel and Finger, 2011), whereby the rocking curves are fitted with pseudo-Voigt function of ka_1 and ka_2 contributions as a function of 2θ.

Cargille refractive index matching fluids Series A and B at 0.002 intervals were used to determine index of refraction. The matching fluids are calibrated, by Cargille, at 25^{O}C and have a standard deviation of 0.0002 with a temperature correction average of 0.0004/^{O}C. Index matching fluids were used at lab temperature (22°C) and working values were adjusted for dispersion using manufacturer calibrated oil index at D, C, and F Fraunhofer lines (589.3 nm, 656.3 nm, and 486.1 nm respectively) fit to a Cauchy relation.

Refractive index measurements were made at five wavelengths: 430 nm, 480 nm, 532 nm, 632.8 nm, and 740 nm using Thorlabs FB430-10-1, Thorlabs 480-10, Newport 10FL10-532, L-632.8-10, and S10-740-F-740G-corion optical filters, respectively.

4.3.2 Equipment

A Meiji MT9900 microscope was modified to study large crystals (up to 1 cm in longest dimension) using spindle stage techniques (Bloss 1981). Use of the modified petrographic microscopes allowed for the observation of samples under standard petrographic conditions such as orthoscopic or conoscopic illumination, polarized or cross-polarized light, or reflected light. Reflected light capabilities allow for precise mounting of crystals using morphological faces as indicator of orientation. Samples were viewed under a range of magnifications from 40x to 1000x.

A precision rotary stage-mounted spindle was added to the microscope in place of the original sample stage. Sample position was precisely determined using 1 arcminute resolution Vernier scales on the rotary and spindle stages. It is often desirable to re-mount crystals, once precise crystal orientation has been determined, in desired orientations. A custom objective turret piece was designed to mount crystals coaxially to the optical axis of the microscope. The larger working distance and modular design allowed for the accommodation of a spindle stage, goniometer head, rotary table with condenser, and an index matching fluid immersion cell. A goniometer mounted immersion cell was designed to allow for complete sample immersion in index matching fluids during rotation. Complete immersion eliminated unwanted surface scattering, increasing accuracy of extinction and index measurements and allowed for Becke line measurements to determine index of refraction.

4.3.3 Methods

Crystals with cross sectional dimensions on the order of 3 mm were mounted to the spindle stage using silicone adhesive, a flexible and non-rigid drying adhesive was used to prevent unnecessary strain generation. Crystals were immersed in index matching fluid with a refractive index approximately equal to n_β, ensuring the wave normal for the light remains unchanged in direction after entry into the crystal. Index matching fluids were of course varied for refractive index measurements.

Determination of the optical indicatrix requires three measurements: orientation of principal vibration axes, indices of refraction along principal vibration axes, and optic orientation. There are a number of methods for doing this either under conoscopic or orthoscopic examination depending upon the motivation (i.e. material identification, structure/composition characterization, indicatrix determination, chromatic dispersion measurement, etc.) and accuracy desired. Here we have primarily used orthoscopic methods for measurements; whereas, conoscopic methods were used to view interference figures for verification.

The optic axes and angles (i.e. the principal vibration axes, optical normal, acute and obtuse bisectrix, and optic axial angle 2V) were determined through the use of extinction curves under orthoscopic examination. Extinction occurs when one of the two orthogonal vibration directions in a crystal is parallel to the lower polarizer. In this orientation all light which passes through the sample is absorbed by the analyzer. By recording and plotting the orientations at which a single crystal entered extinction under crossed polarizers, it was possible to generate extinction curves. These curves were measured for extinction angles (Ms) between 0°S and

180°S in 10° steps. The computer program Excalibrw of Gunter et al. (Gunter, 2005) was used to numerically solve for the spindle stage coordinates of the optical axes from which the other optic directions and angles could be calculated.

Excalibrw is based on Joel's equation by which a pair of equivibration directions (i.e. two different vibration directions exhibiting the same refractive index *p* and q) with unit vectors, **p** and **q** respectively, are related by their orientations relative to $\mathbf{a_1}$ and $\mathbf{a_2}$, the corresponding unit vectors of the optic axes a_1 and a_2. Specifically the product of the cosines of the angles **p** and **q** formed relative to a1 and a2 will be equal.

$$(\mathbf{q} \cdot \mathbf{a_1})(\mathbf{q} \cdot \mathbf{a_2}) = (\mathbf{p} \cdot \mathbf{a_1})(\mathbf{p} \cdot \mathbf{a_2}) \qquad [2]$$

Unit vector **q** is defined as parallel to the spindle axis and **p** as the unit vector (0,1,0). The geometric derivation of Joel's equation from Bloss (1981) is presented in Appendix A. The computer program Excalibrw (Gunter, 2005) numerically solves for $\mathbf{a_1}$ and $\mathbf{a_2}$ given measured coordinates of **q**. A minimum of four measured extinction positions, (Ms, S) describing q orientation, is required to solve for the six unknown $\mathbf{a_1}$ and $\mathbf{a_2}$ coordinates.

Once the optic directions were known, the indices of refraction were measured along principal axes (i.e. n_α, n_β, and n_γ). The crystal was submerged in index matching fluid using the immersion cell, and the Becke line method, as described by Bloss (1981), was used to match sample index of refraction with index matching fluids under orthoscopic examination. Initially the sample was placed above the microscope focal plane. As the stage was lowered, Becke line motion was observed and recorded using the microscope camera. Long microscope camera exposure times were often required for chromatic dispersion measurements due to the limited light transmission of optical filters towards the extremes of the visible spectrum. The Becke line moves toward the material with higher refractive index. The higher index material (oil or crystal) was then noted. The procedure was repeated iteratively with different index matching fluids until converging upon a refractive index match.

The optic orientation is specified by a transformation matrix derived from the Euler angles between the principal vibration axes and the crystallographic axes. A Huber optical reflection goniometer was used to measure interfacial angles and index planes by redundant reference to crystal facets. Then a plane expressed in the morphological habit, for example the (002), was precisely oriented normal to the microscope viewing axis using retroreflection of the coaxial light used in reflection imaging. The Becke line method was then used as described previously to determine the index of refraction in the perpendicular directions, for example the b crystallographic axis. Comparing these measured values to those from the indicatrix determined with extinction measurements on the spindle stage provides the Euler angles for specifying the optic orientation.

4.4 Results

The results of lattice parameter determination are presented in Table 4.1 for four different batches of acetaminophen using both unconstrained and monoclinic-constrained least squares fitting. Variation in the volume between the four different batches varies by less than three parts in 10^4, including one batch with 100 mg PHa impurity. Variation in lattice parameters, significantly above the precision of the measurement, correlate with the amount PHa in solution, wherein the a-axis contracts and the b and c-axis expand with impurity. The only outlier is the comparison of the b-axis for the two pure samples, Acet-8 and Acet-200 mg PHa. The batch labeled Acet-8 as well as 200 mg PHa samples were selected for optical properties measurements.

The optical properties of acetaminophen form I are listed in Table 4.2. The Cauchy dispersion relation was used to fit the measured index of refraction values, resulting in visible spectrum dispersion relations, shown in Figure 4.4. Reported errors account for uncertainty in the index of the Cargille oils, which were calibrated with a standard deviation of ±0.0002 at discrete 0.002 intervals. The Becke line method is dependent upon the user's ability to spot the Becke line. The wavelength dependent sensitivity of the human eye results in systematic index matching errors, when matching optically. These errors were minimized through the use of a microscope mounted CCD camera making the error contribution negligible. Exposure time was adjusted until the Becke line was clearly visible. Errors in the dispersion fit can be found in Table 4.2.

Error in indices of refraction found in Table 4.2 result from several contributing factors. Spindle stage orientation in conjunction with computer analysis of extinction data can be expected to result in an orientation within ±2° (Bloss, 1981). High precision extinction data collected using a CCD should result in an error no greater than 2° if not significantly less. Measurements performed from extinction data, as well as orientation from retroreflection agreed within index matching oil error in our experience. Using the curvature of the ellipsoid it is possible to estimate the error in principal refractive indices with a given misorientation. As birefringence increases so will index error for a given degree of misorientation. This results from the increased curvature of the ellipsoid of high birefringence materials. For a material with the birefringence of acetaminophen (0.129), an error in orientation of 2° can result in errors in principal refractive indices of 0.00016 for γ and 0.00013 for α (Bloss, 1981). Both the visual

Table 4.1: Lattice parameters of monoclinic acetaminophen from several batches in this study.

Acetaminophen (unconstrained least squares)

Batch No.	*a* (Å)	*b* (Å)	*c* (Å)	a (deg)	b (deg)	g (deg)	Vol (Å^3)
Acet-8	7.1015(2)	9.3818(2)	11.7103(2)	90.006(2)	97.416(2)	89.998(2)	773.68(3)
Acet-11	7.1014(1)	9.3804(3)	11.7098(4)	90.007(3)	97.419(3)	90.000(3)	773.51(4)
Acet-00 mg PHa	7.0989(6)	9.3838(4)	11.7122(6)	89.997(4)	97.413(6)	89.996(6)	773.68(9)
Acet-100 mg PHa	7.1009(2)	9.3821(1)	11.7108(2)	90.001(2)	97.415(2)	90.002(2)	773.67(3)

Acetaminophen (monoclinic constraints, b-unique)

Batch No.	*a* (Å)	*b* (Å)	*c* (Å)	a (deg)	b (deg)	g (deg)	Vol (Å^3)
Acet-8	7.1015(2)	9.3818(2)	11.7103(2)	90.000(0)	97.416(2)	90.000(0)	773.68(4)
Acet-11	7.1014(3)	9.3804(3)	11.7098(3)	90.000(0)	97.419(3)	90.000(0)	773.51(5)
Acet-00 mg PHa	7.0989(6)	9.3838(5)	11.7122(5)	90.000(0)	97.413(6)	90.000(0)	773.68(9)
Acet-100 mg PHa	7.1009(2)	9.3821(2)	11.7108(2)	90.000(0)	97.415(2)	90.000(0)	773.68(3)

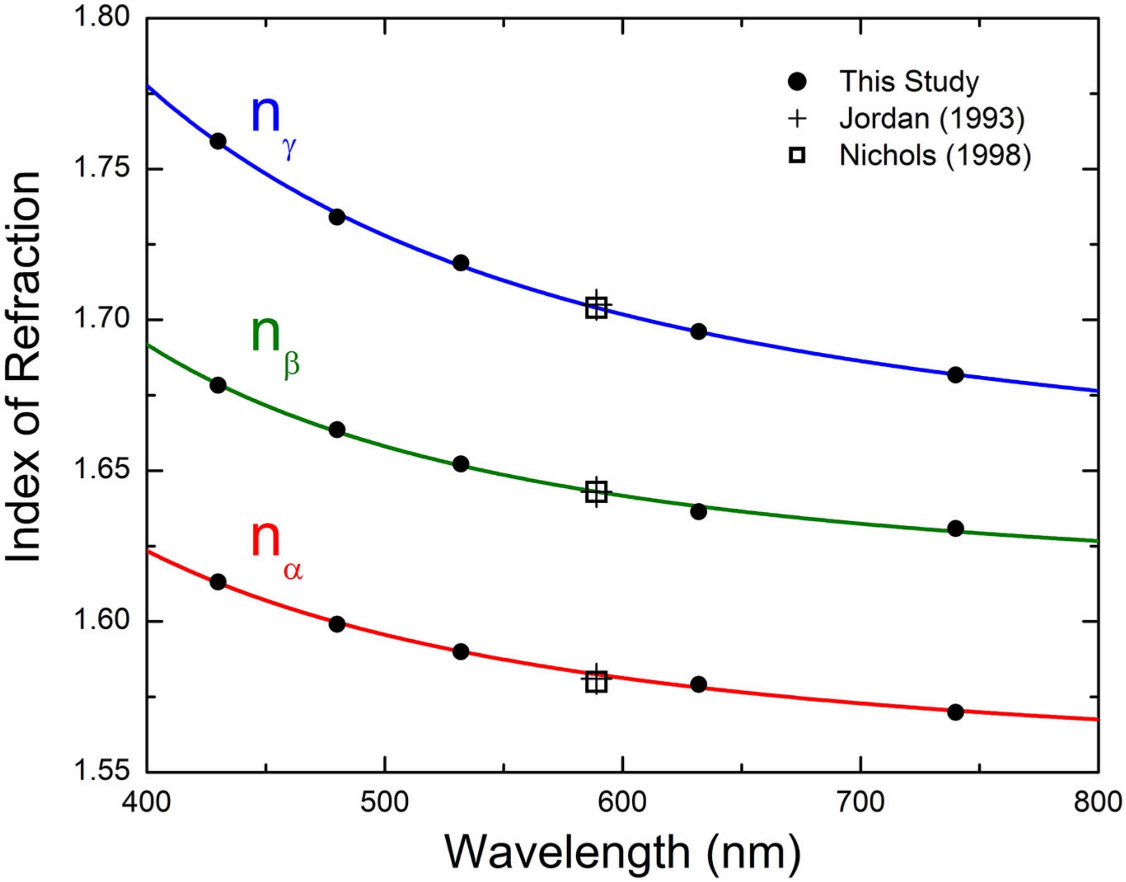

Figure 4.4: Acetaminophen dispersion data for sample Acet-8 (0 mg Pha) (filled circles), fit to the Cauchy relation (solid curves).

Table 4.2: Acetaminophen optical properties.

Refractive Indices (532nm)	**Acet-8 (0 mg Pha)**	**200 mg PHa**	
n_α	1.590(1)	1.587(1)	
n_β	1.652(1)	1.651(1)	
n_γ	1.719(1)	1.715(1)	
Birefringence	0.129	0.128	
Cauchy Constants (Acet-8)	A (μm)	B (μm^2)	C (μm^4)
n_α	1.551(3)	0.01055(2)	0.0002(3)
n_β	1.609(6)	0.01039(4)	0.0004(5)
n_γ	1.645(5)	0.01998(3)	0.0002(4)
Space Group	$P2_1/n$		
a (Å)	7.1015(2)		
b (Å)	9.3818(2)		
c (Å)	11.7103(2)		
β (deg.)	97.416(2)		
Optic Sign	(-)		
Optic Axial Angle (2V)	91(1)°		
Acute Bisectrix	α		
Extinction* (532nm)	35.04°		
Optical Orientation	X = α = b		

* γ ∧ {10-1}

recognition of the Becke line as well as dispersion fitting errors contribute to the precision of the Becke line method. The use of the microscope mounted CCD to locate Becke lines removes the visual error component. The error contribution from dispersion fitting of oils to Fraunhofer lines is also minimal given their calibrated error of ±0.0002. Indicatrix orientation is confirmed via comparison with crystallographic morphology. Misalignment of crystal faces aligned through retroreflection is negligible. Orientation of samples may prove difficult however, if required faces are not expressed in crystal habit. In this case, orientation via X-ray diffraction, providing orientation errors well within 2°, is suggested. All of these errors are insignificant compared to the discrete 0.002 intervals of the Cargille oils, which conservatively sets the uncertainty in the measurement at ±0.001. There is a difference, above uncertainty, for n_a and n_g between the Acet-8 and the Ace 200 mg PHa samples.

The Cauchy dispersion relation was used to fit index of refraction data,

$$n_\lambda = A + \frac{B}{\lambda^2} + \frac{C}{\lambda^4} \quad [3]$$

where index of refraction at a given wavelength, n_λ, can be related to three constant, A, B, and C, as well as wavelength, λ.

The Cauchy relation assumes there is only one absorption band and it is located at a far higher wavelength than that being investigated. While it is true that many molecular crystals have many absorption bands over a wide spectral range (Isbell and Brewster, 1998), the assumption is not unreasonable over the short range of 400 nm for acetaminophen, as can be seen by the quality of the Cauchy fit of the presented data in Figure 4.4. Orientation of the optical indicatrix in relation to crystallographic directions can be seen in Figure 4.2. The orientation appears to be in good agreement with Nichols (1998).

4.5 Discussion

Table 3 compares refractive indices calculated from the determined Cauchy relations at 589 nm with the measurements of Jordan (1993) and Nichols (1998). The values are the same within uncertainty from measurement precision. The optic orientation defined here agrees with the description given in Nichols (1998), that is the optical indicatrix X-axis, corresponding to the

n_α refractive index, lies parallel to the crystallographic *b*-axis and the indicatrix Z-axis refractive index is equal to n_γ and forms an angle of 35.04° with {10-1} (Figure 1,2). This also agrees with symmetry requirements. Acetaminophen form 1 belongs to the monoclinic system, 2/m point symmetry. In this group, the two-fold rotation axis lies along the *b*-crystallographic direction, perpendicular to the mirror plane containing both a and c crystallographic axes. The passage of light through crystals involves the interaction between electromagnetic fields and the electron cloud surrounding the average atomic positions. As a result, variation of index of refraction for different polarization directions follows the point-group symmetry of the crystal. Therefore, one of the primary axes of the indicatrix must parallel the *b*-crystallographic direction, satisfying the mirror plane.

Table 4.3: Comparison of refractive indices at 589nm.

Refractive Indices (589nm)	**Acet-8 * (0 mg Pha)**	**Jordan (1993)**	**Nichols (1998)**
n_α	1.583(1)	1.581(1)	1.580(1)
n_β	1.642(1)	1.643(1)	1.643(1)
n_γ	1.704(1)	1.705(1)	1.704(1)
Birefringence	0.121	0.124	0.124

* Calculated from Cauchy relations and Table 4.1 constants

PAA is one of several structurally related impurities that are present in the synthesis of PHA (Fairbrother 1973). PAA effects on PHA have been extensively studied because of pronounced changes of morphological habit and dissolution kinetics with relatively small compositional additions of PAA. With addition of PAA, PHA crystals change from a tabular to a needlelike morphological habit with elongated {110} faces (Figure 4.3). While there are structurally related substances, such as metacetamol and p-acetoxybenzoic acid, that incorporate into PHA crystal in greater percentages (see segregation coefficients in Hendrikesen 1998), PAA influences the perfection of the crystal lattice (i.e. mosaicity and strain) as quantified by conventional X-ray diffraction (Shekunov 1997) and also topography (Prasad 2002) and nucleation, growth, and dissolution kinetics (Shekunov 1997, Hendriksen 1998, Prasad 2002). The prevailing understanding is that PAA inhibits growth of {110} sectors and becomes incorporated. The molecule of PAA is 1.24 times larger in volume than the PHA molecule (Finnie 1999) and strains the lattice. In fact, at some additive concentration (about 0.5 mol % for the conditions of the experiments in Shekunov 1997), the strain relaxes by forming planar cleavage defects in the {110} growth sectors. One of the potentially more industrially significant consequences is that the induced strain associated with incorporation of PAA influences incorporation of water, or possibly other crystallization solvents, in complicated ways that depend on concentration (Chow 1985). The presence of impurities, particularly water or other growth solvents, may account for certain batch-to-batch variation in the properties of drugs and excipients (Chow 1985).

Incorporation of growth solvents because of lattice strain is not unique to PHA or unforeseen as Cottrell atmospheres in proximity of dislocation cores are a well-known phenomenon, although more so for inorganic crystalline materials than organic molecular crystals. Molecular crystals, such as PHA and other molecular crystals like monoclinic cyclotetramethylene tetranitramine, have a tendency to grow with highly strained and defected regions at the growth sector boundaries between adjacent morphological planes that have large differences in crystal growth velocities. The effects of the spatially heterogeneous, hkl-dependent strains at growth sector boundaries result in solvent inclusion, oftentimes in the form of internal voids (Gross 1970, Halfpenny 1984). To avoid creating voids during crystal growth, low growth rates must be maintained without fluctuations. Anisotropic growth velocities are inherently unavoidable for anisotropic molecular crystals and will result in some strain even at low rates. Klapper (2002) has demonstrated that accelerations or decelerations in growth rate during the crystallization process greatly aggravates the problem and significantly increases defect density. Anisotropic growth velocities can be associated with the inherent anisotropic bonding/surface energies of molecular crystal lattices or effects of impurity, i.e. the case for PHA in the presence of PAA that inhibits growth in the {110} sectors, or external factors such as changes in growth rate that arise from either imprecise control of conditions (evaporation or temperature), the gradient experienced along solubility curves, especially when pushing for increased yields, and/or the width of the metastable zone. Since strains in PHA from PAA inclusion can become sufficient to cause planar cleavage, the incorporation of solvent (Chow 1985) in the form of Cottrell atmospheres or otherwise in {110} growth boundary sectors is not surprising. See Figure 7 in Ramos (2007) and references therein for characterization of these effects in single-crystal monoclinic sucrose.

Characterization of structure-property effects of trace impurities in molecular crystals in the solid state is challenging. In general impurities in materials can be characterized by electron microscopies (energy-dispersive X-ray spectroscopy), x-ray fluorescence, conventional x-ray diffraction or topography or by a number of dissolution/disassociation with detection (e.g. chromatography or secondary ion mass spectrometry). All of these techniques have limitations when applied to molecular crystals and/or determining structure-property relations. Refractometry has long been used for characterizing concentration and impurities in non-solids within chemistry and is the industrial standard in food and beverage, cosmetics, fine chemicals, pharmaceuticals, and oil and gas production. Differences in refractive index with five significant figures can routinely be obtained using a precision Abbe refractometer.

Tables 4.1 and 4.2 list lattice parameters and refractive indices for PHA grown from pure solutions and solutions with PAA intentionally added. There is evidence of a possible correlation between the impurity, crystallographic lattice parameters, and principal refractive indices.

4.6 Conclusions

Here we report the synthesis of large euhedral crystals of monoclinic acetaminophen, which were used to determine the principal indices of refraction and their dispersion across the visible spectrum. Results at 598 nm agree well with previously reported values. Crystals grown from solvents containing 0-200 mg of PHa display identical optical properties and lattice parameters within error. The spindle stage technique employed here removes previous ambiguity in the orientation of the biaxial indicatrix in monoclinic acetaminophen. The results of this study will be used to calculate the sound velocity dispersion curves determined by Brillouin light scattering measurements, currently in progress. Ultimately, knowledge of the single-crystal elastic properties of acetaminophen will facilitate modeling the compression behavior of acetaminophen in various binding media, which has the potential to further optimize the tablet making process.

Chapter 5

Development of 2-D X-ray Diffraction Techniques for Rapid Single-Crystal Analysis

5.1 Northwestern Mineral Physics Laboratory Huber Diffractometer

The Northwestern Mineral Physics Laboratory 4-circle Huber diffractometer is now equipped with a point detector and a 2-D image plate area detector. Point detectors are advantageous in that they can collimate the diffracted beam, reducing background intensities and improving signal-to-noise ratios. The collimation of the diffracted beam allows for precise positional measurement, ideal for determination of unit-cell parameters. The precision of point detectors comes at the sacrifice of speed. Lattice volume measurements performed with a point detector require the precise measurement of many, often up to 50, peaks. Prior to precise *hkl* measurements, sample orientation must be determined in order for theoretical peak positions in laboratory coordinates to be calculated. Orientation can be determined given coordinates for two known *hkl*s. In complex and high background situations, common in diamond anvil cell experiments where diamond and gasket peaks often overlap with sample 2θs, the search for known *hkl*s can take up to 12 hours. After orientation is determined a common procedure involves centering all ~50 reflections using the method of 8-position centering (King and Finger, 1979), where every unique *hkl* is centered with rocking curves (ω scans) in all four equivalent positions, first in positive 2θ and again at negative 2θ positions, resulting in eight rocking curves for each *hkl*. This method provides very high precision in determined lattice parameters of a few parts in 10^4 by minimizing crystal offsets from the center point of the goniometer and zero-point errors in the 2θ, w, and c axes. Full profile peak fitting can be carried out using the program Single (Angel and Finger, 2011), whereby the rocking curves are fitted with pseudo-Voigt function of $k\alpha_1$ and $k\alpha_2$ contributions as a function of 2θ.

The primary advantage of 2-D detectors, for single-crystal applications, is speed. Sample orientation can be rapidly determined using image processing software such ATREX (Dera,

2007) or CrysAlis. Sample orientation is also not prerequisite knowledge for an X-ray experiment using an area detector. Area detectors, however, lack the precision of point detectors with large goniometers with high angular resolution. Sample misalignment and precession, errors in sample to detector distance, pixel size, pixel ghosting, and pixel bleeding can all lead to decreased precision of area detector measurements. A system which takes advantage of area detector speed and point detector precision is therefore desirable.

The Northwestern Mineral Physics Laboratory Huber diffractometer has been equipped with a MAR345 area detector in conjunction with the point detector. The detector is mounted to a linear rail system (Figure 5.1), which allows for easy transition between the point detector mode and area detector operating mode. The combination allows for rapid orientation of single crystals using the area detector and precise measurements to be made using the point detector. The MAR345 345 mm diameter image plate can be brought to within 216 mm of the sample position. Details of the X-ray energies provided by the Huber's sealed tube molybdenum source are found in Table 5.1. Precise X-ray wavelengths produced by the molybdenum source were determined during initial commissioning of the instrument and differ slightly from theoretical wavelengths. The 1% deviation in wavelength becomes important when using the Huber point detector. The sample to point detector distance of 940 mm provides high angular resolution capable of resolving $K\alpha_1$ and $K\alpha_2$ even at low scattering angle. When operating the MAR345 area detector use of $K\alpha_{avg}$ suffices. At the minimum 216 mm sample to image plate distance the MAR345 detectors maximum scattering angle is 38° 2θ.

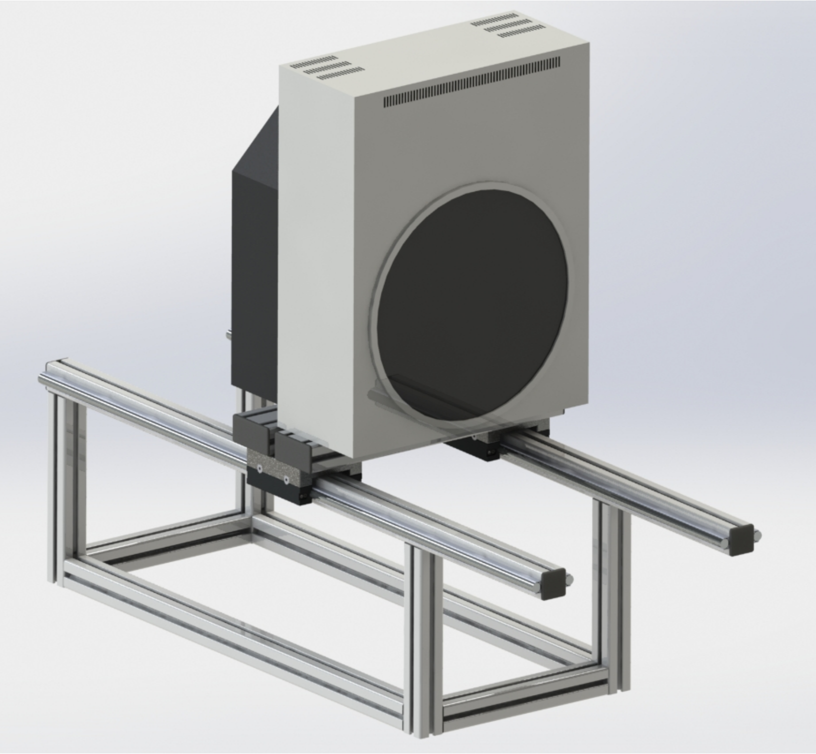

Figure 5.1: CAD rendering of the MAR345 area detector and custom linear rail system.

Table 5.1: Molybdenum X-ray wavelengths.

	Mo (Theoretical)	**Mo (Huber)**
Kα_1 (Å)	0.70932	0.709316
Kα_2 (Å)	0.71354	0.713606
Kα_{avg} (Å)	0.71073	0.710746
Kβ (Å)	0.63225	
β - filter	Zr	

Calibration of the detector to sample geometry is performed by collecting a lanthanum hexaboride (LaB_6) powder pattern, Figure 5.2, and refinement is performed using the Dioptas

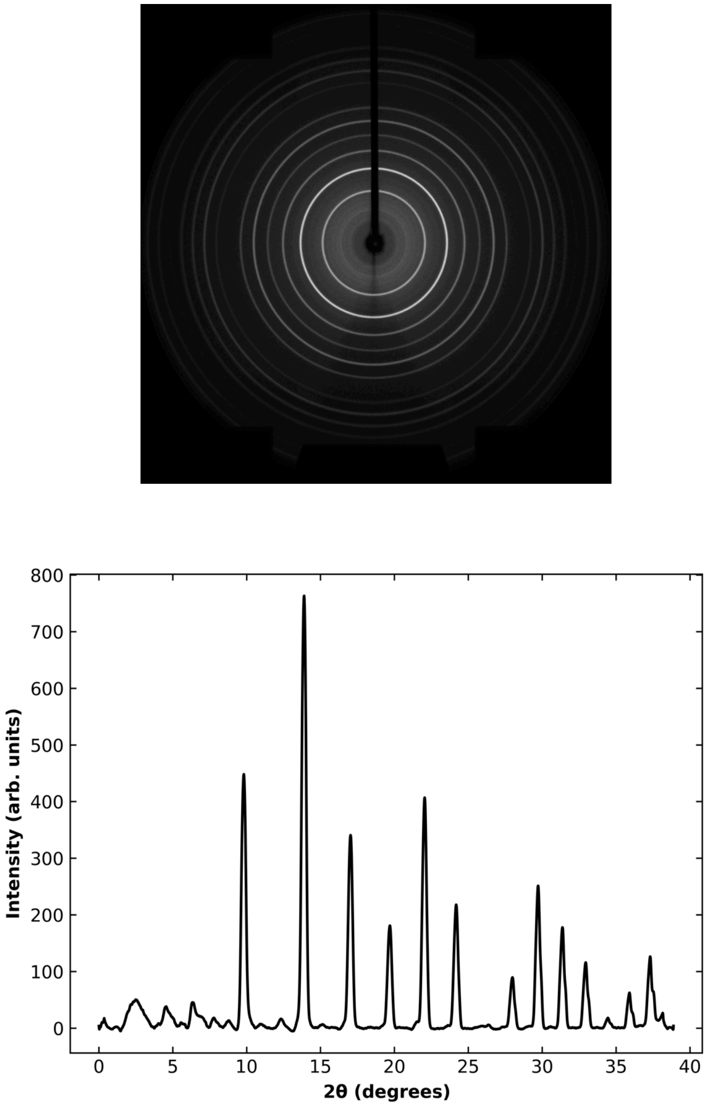

Figure 5.2: Example MAR345 image of LaB_6 calibration standard collected on NU-Huber (top) collected using a 360 degree phi scan and 5 minute collection time. Integrated spectrum from LaB6 image (bottom). Resulting calibration parameters from Dioptas (Prescher et al., 2015): [Distance: 216.8024, Wavelength*: 0.7107, Polarization: 0.99, Center X: 1141.635 px, Center Y: 1154.591 px, Rotation: 148.553725 deg, Tilt: 0.284538 deg, Pixel width*: 150.0 µm, Pixel height*: 150.0 µm]. * fixed during refinement

software package (Prescher et al., 2015). A sample to detector distance of approximately 216.8 +/- 0.3 mm is routinely achievable using the built in detector rail stops. This precision is sufficient for the determination of single crystal orientation matrixes for further refinement using the NU-Huber point detector. When collecting images for data analysis purposes calibrations should be taken at the beginning of every experiment.

The MAR345 detector is controlled with MAR Control (Figure 5.3). MAR Control is a program written to synchronize the MAR345 detector and Huber diffractometer. Several function and collection routines are available through MAR Control including: controlling detector modes, performing single exposure routines, running phi scans, performing automated data collections for single crystal experiments, shutter control, and providing a TCP client to pass commands directly to the Huber Controller.

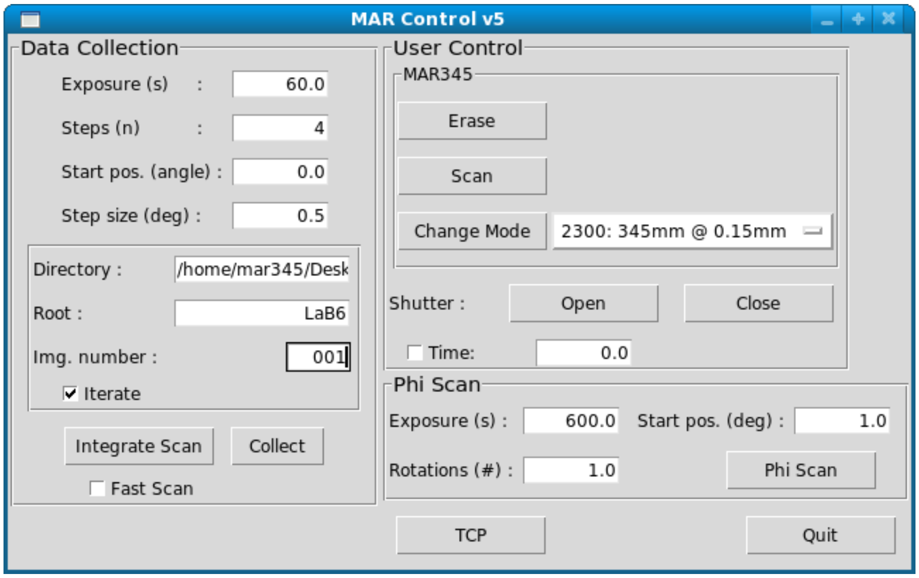

MAR Control v5

Data Collection

Exposure (s) : 60.0

Steps (n) : 4

Start pos. (angle) : 0.0

Step size (deg) : 0.5

Directory : /home/mar345/Desk

Root : LaB6

Img. number : 001

☑ Iterate

☐ Fast Scan

User Control

MAR345

2300: 345mm @ 0.15mm

☐ Time: 0.0

Phi Scan

Exposure (s) : 600.0

Start pos. (deg) : 1.0

Rotations (#) : 1.0

Figure 5.3: MAR Control is used to control the Huber diffractometer and MAR345 detector when operating in the area detector mode.

Descriptions of MAR Control routines can be found in the Huber Diffractometer Manual (Appendix B). In summary, MAR Control allows the user to control the Huber diffractometer axis and shutter and synchronize their motions with the MAR345 detector. One of three primary routines can be used to collect an image or a set of images using the area detector. The first mode "Phi Scan" is primarily used to determine crystallographic orientation. In this mode, the diffractometer spins the φ axis with the shutter open. This mode results in what is known as a "phi scan image" with which position of two peaks can be determined defining the orientation of the sample on the diffractometer. The second mode "Integrate Scan" should be used when collecting multiple images over several angular ranges. An integrate scan starts at the input "Start pos." and scans the φ axis over the given "Step size" exposing the detector over the step size range, integrating the detector image over φ + "Step size". The shutter will then be closed and the image read out. Once the image has been read out, the detector will erase. Following erasing, which takes approximately 30 seconds, the shutter will open and the φ axis will scan for another "Step size." This procedure will repeat for the input number of "Steps." This image format is what is expected by programs such as ATREX (GSE_ADA/RSV) for data analysis. The third mode can be performed with the "Collect" button. In the "Collect" mode an exposure will be collected at every step, with φ stationary, for n "Steps." This mode is primarily for rapid screening. The vast majority of reciprocal space is neglected in this mode and will not be observed in the collected image.

5.2 Sample Orientation

The UB matrix also known as the orientation matrix, a 3x3 matrix product of the U and the B matrix, defines sample orientation relative to a fixed laboratory coordinate system. The B matrix is defined by unit cell parameters:

$$\mathrm{B} = \begin{pmatrix} a^* & b^* \cos\gamma^* & c^* \cos\beta^* \\ 0 & b^* \sin\gamma^* & -c^* \sin\beta^* \cos\alpha \\ 0 & 0 & c^{-1} \end{pmatrix} \qquad [5.1]$$

where * denote reciprocal values. Components of B can be easily calculated through the inversion of metric tensor G:

$$\mathrm{G} = \begin{pmatrix} \mathrm{a}\cdot\mathrm{a} & \mathrm{a}\cdot\mathrm{b} & \mathrm{a}\cdot\mathrm{c} \\ \mathrm{b}\cdot\mathrm{a} & \mathrm{b}\cdot\mathrm{b} & \mathrm{b}\cdot\mathrm{c} \\ \mathrm{c}\cdot\mathrm{a} & \mathrm{c}\cdot\mathrm{b} & \mathrm{c}\cdot\mathrm{c} \end{pmatrix} = \begin{pmatrix} \mathrm{a}^2 & \mathrm{ab}\cos\gamma & \mathrm{ac}\cos\beta \\ \mathrm{ba}\cos\gamma & \mathrm{b}^2 & \mathrm{bc}\cos\alpha \\ \mathrm{ca}\cos\beta & \mathrm{cb}\cos\alpha & \mathrm{c}^2 \end{pmatrix} \qquad [5.2]$$

If D = {a,b,c} and G is the metrical matrix of D then G^{-1} is the metrical matrix of D^*.

The U matrix defines the orientation of the crystal coordinate system to the φ-axis Cartesian coordinate system (Busing and Levy, 1967).

If **h** = (*hkl*) and $\mathbf{h}_\varphi$ denotes the vector **h** in diffractometer coordinates, then the UB matrix transforms **h** into diffractometer coordinates:

$$\mathbf{h}_\varphi = \mathrm{UB}\cdot\mathbf{h} = \frac{1}{\mathbf{d_{hkl}}}\begin{pmatrix} \mathrm{h}_{\boldsymbol{\varphi}\mathbf{1}} \\ \mathrm{h}_{\boldsymbol{\varphi}\mathbf{2}} \\ \mathrm{h}_{\boldsymbol{\varphi}\mathbf{3}} \end{pmatrix} = \frac{2\sin\theta}{\lambda}\begin{pmatrix} \cos\omega\cos\chi\cos\varphi - \sin\omega\sin\varphi \\ \cos\omega\cos\chi\sin\varphi + \sin\omega\cos\varphi \\ \cos\omega\sin\chi \end{pmatrix} \qquad [5.3]$$

Equation 5.3 defines the possible diffractometer setting angles at which diffraction can be obtained from **h** (Angel et al., 2000). When the diffractometer is operating in bisecting mode the ω-angle is set to zero, the motor angles χ and φ can be obtained from $\mathbf{h}_\varphi$:

$$\chi = \arctan\left(\frac{\mathrm{h}_{\boldsymbol{\varphi}\mathbf{3}}}{\sqrt{\mathrm{h}_{\varphi 1}^2+\mathrm{h}_{\varphi 2}^2}}\right) \qquad [5.4]$$

$$\varphi = \arctan\left(\frac{\mathrm{h}_{\boldsymbol{\varphi}\mathbf{2}}}{\mathrm{h}_{\boldsymbol{\varphi}\mathbf{1}}}\right) \qquad [5.5]$$

$$\omega = 0 \qquad [5.6]$$

Equations 5.4-6 only hold for diffractometer geometries where +x is along the diffraction vector and +y follows the right hand rule with vertical +z.

6. References

Agrusta, R., J. Van Hunen, and S. Goes. 2014. “The Effect of Metastable Pyroxene on the Slab Dynamics.” *Geophysical Research Letters* 41 (24): 8800–8808. doi:10.1002/2014GL062159.

Akaogi, M., and S. Akimoto. 1977. “Pyroxene - Garnet Solid-Solution Equilibria in the Systems $Mg_3Si_4O_{12}$-$Mg_3Al_2Si_3O_{12}$ and $Fe_4Si_4O_{12}$-$Fe_3Al_2Si_3O_{12}$ at High Pressures and Temperatures.” *Physics of the Earth and Planetary Interiors* 15: 90–106.

Akashi, A., Y. Nishihara, E. Takahashi, Y. Nakajima, Y. Tange, and K. Funakoshi. 2009. “Orthoenstatite/clinoenstatite Phase Transformation in MgSiO3 at High-Pressure and High-Temperature Determined by in Situ X-Ray Diffraction: Implications for Nature of the X Discontinuity.” *J. Geophys. Res.* 114: B04206.

Anderson, B. J. 2008. “Paracetamol (Acetaminophen): Mechanisms of Action.” *Paediatric Anaesthesia* 18 (10): 915–21. doi:10.1111/j.1460-9592.2008.02764.x.

Angel, R.J., R.T. Downs, and L.W. Finger. 2000. “High-Temperature–High- Pressure Diffractometry,” no. 1992. doi:10.238/rmg.2000.41.16.

Angel, R.J., C. McCammon, and A.B. Woodland. 1998. “Structure, Ordering and Cation Interactions in Ca-Free P2(1)/c Clinopyroxenes.” *Physics and Chemistry of Minerals* 25 (4): 249–58.

Angel, R.J., and D.A. Hugh-Jones. 1994. “Equations of State and Thermodynamic Properties of Enstatite Pyroxenes.” *Journal of Geophysical Research* 99 (B10): 19777–83. doi:10.1029/94JB01750.

Angel, Ross J., A. Chopelas, and N.L L. Ross. 1992. “Stability of High-Density Clinoenstatite at Upper-Mantle Pressures.” *Nature* 355: 322–24. doi:10.1038/355242a0.

Angel, R.J., J. Gonzalez-Platas, and M. Alvaro. 2014. “EosFit7c and a Fortran Module (Library) for Equation of State Calculations.” *Zeitschrift Fur Kristallographie* 229 (5): 405–19. doi:10.1515/zkri-2013-1711.

Angel, R.J., J. M. Jackson, H. J. Reichmann, and S. Speziale. 2009. “Elasticity Measurements on Minerals: A Review.” *European Journal of Mineralogy* 21 (3): 525–50. doi:10.1127/0935-1221/2009/0021-1925.

Bina, C.R., S. Stein, F. C. Marton, and E.M. Van Ark. 2001. “Implications of Slab Mineralogy for Subduction Dynamics.” *Physics of the Earth and Planetary Interiors* 127 (1–4): 51–66. doi:10.1016/S0031-9201(01)00221-7.

Bina, C.R., and B.J. Wood. 1984. “The Eclogite to Garnetite Transition -- Experimental and Thermodynamic Constraints.” *Geophysical Research Letters* 11 (1): 15–17.

Blöchl, P.E. 1994. “Projector Augmented-Wave Method.” *Physical Review B* 50 (24): 17953–79. doi:10.1103/PhysRevB.50.17953.

Bloss, F. Donald. 1981. *The Spindle Stage: Principles and Practice*. Cambridge: Cambridge University Press.

Bolfan-Casanova, N. 2005. “Water in the Earth’s Mantle.” *Mineralogical Magazine* 69 (3): 229–58. doi:10.1180/0026461056930248.

Bolfan-Casanova, N., H. Keppler, and D.C. Rubie. 2000. “Water Partitioning between Nominally Anhydrous Minerals in the MgO-SiO_2-H_2O System up to 24 GPa: Implications for the Distribution of Water in the Earth’s Mantle.” *Earth and Planetary Science Letters* 182 (3–4): 209–21. doi:10.1016/S0012-821X(00)00244-2.

Bolme, C.A., and K.J. Ramos. 2014. “The Elastic Tensor of Single Crystal RDX Determined by Brillouin Spectroscopy.” *Journal of Applied Physics* 116 (18): 183503. doi:10.1063/1.4901461.

Busing, W.R., H.A. Levy. 1967. “Angle Calculations for 3- and 4-Circle X-Ray and Neutron Diffractometers.” *Acta Crystallographica* 1 (4). International Union of Crystallography: 457–64. doi:10.1107/S0365110X67000970.

Chao, E.C.T. 1976. “The Application of Quantitative Interference Microscopy to Mineralogic and Petrologic Investigations.” *American Mineralogist* v. 61 (nos. 3 & 4): 212–28. http://rruff.info/doclib/am/vol61/AM61_212.pdf.

Chopelas, A., and R. Boehler. 1989. “Thermal Expansion Measurements at Very High Pressure, Systematics, and a Case for a Chemically Homogeneous Mantle.” *Geophysical Research Letters* 16 (11): 1347–50.

Cottaar, S., T. Heister, R. Myhill, I. Rose, and C. Unterborn. 2016. “BurnMan v0.9.0,” April. doi:10.5281/ZENODO.546210.

Cottaar, S., Timo H., Ian R., and C. Unterborn. 2014. “BurnMan: A Lower Mantle Mineral Physics Toolkit.” *Geochemistry, Geophysics, Geosystems* 15 (4): 1164–79. doi:10.1002/2013GC005122.

Czyzak, S.J., W.M. Baker, R.C. Crane, and J.B. Howe. 1957. “Refractive Indexes of Single Synthetic Zinc Sulfide and Cadmium Sulfide Crystals.” *Journal of the Optical Society of America* 47 (3): 240. doi:10.1364/JOSA.47.000240.

Dera, P. 2007. “GSE_ADA Data Analysis Program for Monochromatic Single Crystal Diffraction with Area Detector.” Chicago, IL: GSECARS.

Dera, P., K. Zhuravlev, V. Prakapenka, M.L. Rivers, G.J. Finkelstein, O. Grubor-Urosevic, O. Tschauner, S.M. Clark, and R.T. Downs. 2013. "High Pressure Single-Crystal Micro X-Ray Diffraction Analysis with GSE_ADA/RSV Software." *High Pressure Research* 33 (3): 466–84. doi:10.1080/08957959.2013.806504.

Du, W., S.M. Clark, and D. Walker. 2015. "Thermo-Compression of Pyrope-Grossular Garnet Solid Solutions: Non-Linear Compositional Dependence." *American Mineralogist* 100 (1): 215–22. doi:10.2138/am-2015-4752.

Duffy, T.S., and Y. Wang. 1998. "Pressure-Volume-Temperature Equations of State." *Reviews in Mineralogy and Geochemistry* 37 (1). Mineralogical Society of America: 425–57.

Dziewonski, A.M., and D.L. Anderson. 1981. "Preliminary Reference Earth Model." *Physics of the Earth and Planetary Interiors* 25 (4): 297–356. doi:10.1016/0031-9201(81)90046-7.

Erba, A., A. Mahmoud, R. Orlando, and R. Dovesi. 2014. "Elastic Properties of Six Silicate Garnet End Members from Accurate Ab Initio Simulations." *Physics and Chemistry of Minerals* 41 (2): 151–60. doi:10.1007/s00269-013-0630-4.

Fan, D., C. Lu, J. Xu, B. Yan, B. Yang, and J. Chen. 2017. "Effects of Water on P-V-T Equation of State of Pyrope." *Physics of the Earth and Planetary Interiors* 267: 9–18. doi:10.1016/j.pepi.2017.03.005.

Finkelstein, G.J., P.K. Dera, and T.S. Duffy. 2015. "Phase Transitions in Orthopyroxene (En90) to 49GPa from Single-Crystal X-Ray Diffraction." *Physics of the Earth and Planetary Interiors* 244. Elsevier B.V.: 78–86. doi:10.1016/j.pepi.2014.10.009.

Garnero, E.J., and A.K. Mcnamara. 2008. "REVIEW Structure and Dynamics of Earth's Lower Mantle." *Science* 320 (May): 626–28.

Gasparik, T.. 1989. “Transformation of Enstatite - Diopside - Jadeite Pyroxenes to Garnet.” *Contrib Mineral Petrol* 102: 389–405.

Armbruster, C.A. Geiger, and G.A. Lager. 1992. “Single-Crystal X-Ray Structure Study of Synthetic Pyrope Almandine Garnets at 100 and 293 K” 77 (197 l): 512–21.

Grand, S.P. 1994. “Mantle Shear Structure beneath the Americas and Surrounding Oceans.” *Journal of Geophysical Research: Solid Earth* 99 (B6): 11591–621. doi:10.1029/94JB00042.

Gunter, M.E., R.T. Downs, K.L. Bartelmehs, S.H. Evans, C.J.S. Pommier, J.S. Grow, M.S. Sanchez, and F. Donald Bloss. 2005. “Optic Properties of Centimeter-Sized Crystals Determined in Air with the Spindle Stage Using EXCALIBRW.” *American Mineralogist* 90 (10): 1648–54. doi:10.2138/am.2005.1892.

Gunter, M.E., R.T. Downs, K.L. Bartelmehs, S.H. Evans, C.J.S. Pommier, J.S. Grow, M.S. Sanchez, and F. Donald Bloss. 2005. “Optic Properties of Centimeter-Sized Crystals Determined in Air with the Spindle Stage Using EXCALIBRW.” *American Mineralogist* 90 (10): 1648–54. doi:10.2138/am.2005.1892.

Haselton, H.T., and R.C. Newton. 1980. “Thermodynamics of Pyrope-Grossular Garnets and Their Stabilities at High Temperatures and High Pressures.” *Journal of Geophysical Research* 85 (B12): 6973. doi:10.1029/JB085iB12p06973.

He, P., X.Huang, Y.Xu, H. Li, X. Wang, and W. Li. 2016. “Journal of Geophysical Research : Solid Earth,” 1–21. doi:10.1002/2015JB012652.Received.

Hier-Majumder, S., and A. Courtier. 2011. “Seismic Signature of Small Melt Fraction atop the Transition Zone.” *Earth and Planetary Science Letters* 308 (3–4). Elsevier B.V.: 334–42. doi:10.1016/j.epsl.2011.05.055.

Hier-Majumder, S., E.B. Keel, and A.M. Courtier. 2014. “The Influence of Temperature, Bulk Composition, and Melting on the Seismic Signature of the Low-Velocity Layer above the Transition Zone.” *Journal of Geophysical Research: Solid Earth* 119 (2): 971–83. doi:10.1002/2013JB010314.

Hill, R. 1951. “The Elastic Behaviour of a Crystalline Aggregate.” *Proceedings of the Physical Society. Section A*, no. September: 3–8. http://iopscience.iop.org/0370-1298/65/5/307.

Hogrefe, A., D.C. Rubie, T.G. Sharp, and F. Seifert. 1994. “Metastability of Enstatite in Deep Subducting Lithosphere.” *Nature*. doi:10.1038/372351a0.

Hu, Y., P. Dera, and K. Zhuravlev. 2015. “Single-Crystal Diffraction and Raman Spectroscopy of Hedenbergite up to 33 GPa.” *Physics and Chemistry of Minerals* 42 (7): 595–608. doi:10.1007/s00269-015-0747-8.

Hu, Y., B. Kiefer, C.R. Bina, D. Zhang, and P.K. Dera. 2017. “High-Pressure γ-CaMgSi2O6: Does Penta-Coordinated Silicon Exist in the Earth’s Mantle?” *Geophysical Research Letters*, 340–48. doi:10.1002/2017GL075424.

Hu, Y., Z. Wu, P.K. Dera, and C.R. Bina. “Thermodynamic and Elastic Properties of Pyrope at High Pressure and High Temperature by First-Principles Calculations.”

Hugh-Jones, D.A., and R.J. Angel. 1997. “Effect of Ca^{2+} and Fe^{2+} on the Equation of State of $MgSiO_3$ Orthopyroxene.” *Journal of Geophysical Research* 102: 12,333-12,340.

Irifune, T., Y. Higo, T. Inoue, Y. Kono, H. Ohfuji, and K. Funakoshi. 2008. “Sound Velocities of Majorite Garnet and the Composition of the Mantle Transition Region.” *Nature* 451 (7180): 814–17. doi:10.1038/nature06551.

Irifune, T., and A.E. Ringwood. 1993. “Phase Transformations in Subducted Oceanic Crust and Buoyancy Relationships at Depths of 600–800 Km in the Mantle.” *Earth and Planetary Science Letters* 117 (1–2): 101–10. doi:10.1016/0012-821X(93)90120-X.

Irifune, T., J.Susaki, T. Yagi, and H. Sawamoto. 1989. “Phase Transformations in Diopside $CaMgSi_2O_6$ at Pressures up to 25 GPa.” *Geophysical Research Letters* 16 (2): 187–90.

Isbell, R.A., and M.Q. Brewster. 1998. “Optical Properties of Energetic Materials: RDX, HMX, AP, NC/NG, and HTPB.” *Propellants, Explosives, Pyrotechnics* 23 (4): 218–24. doi:10.1002/(SICI)1521-4087(199808)23:4<218::AID-PREP218>3.0.CO;2-A.

Jacobsen, S.D. 2006. “Effect of Water on the Equation of State of Nominally Anhydrous Minerals.” *Reviews in Mineralogy and Geochemistry* 62 (1): 321–42. doi:10.2138/rmg.2006.62.14.

Jacobsen, S.D., Z. Liu, T. Boffa, E.F. Littlefield, L. Ehm, and R.J. Hemley. 2010. “Effect of H_2O on Upper Mantle Phase Transitions in $MgSiO_3$: Is the Depth of the Seismic X-Discontinuity an Indicator of Mantle Water Content ?” *Physics of the Earth and Planetary Interiors* 183 (1–2). Elsevier B.V.: 234–44. doi:10.1016/j.pepi.2010.06.015.

Jeanloz, R. 2007. “Majorite: Vibrational and Compressional Properties of a High-Pressure Phase” 86 (1): 1–9. papers2://publication/uuid/CED50701-5ACD-47C5-A4FD-70CFEA45BC20.

Joel, N. 1965. “Determination of the Optic Axes and 2V: Electronic Computation from Extinction Data.” *Mineralogical Magazine*, 412–17.

Joel, N. 1963. “Determination of 2V from One Extinction Curve and Its Related n0 Curve.” *Mineralogical Magazine*, 679–92.

Jordan, D.D. 1993. “Optical Crystallographic Characteristics of Some USP Drugs.” *Journal of Pharmaceutical Sciences* 82 (12): 1269–71. http://www.ncbi.nlm.nih.gov/pubmed/8308710.

Kanzaki, M. 1987. “Ultrahigh-Pressure Phase Relations in the System $Mg_4Si_4O_{12}$-$Mg_3Al_2Si_3O_{12}$.” *Physics of the Earth and Planetary Interiors* 14: 585–87. doi:10.1007/s10789-005-0281-z.

Katayama, I., K. Hirose, H. Yurimoto, and S. Nakashima. 2003. “Water Solubility in Majoritic Garnet in Subducting Oceanic Crust.” *Geophysical Research Letters* 30 (22): 5–8. doi:10.1029/2003GL018127.

Kato, T., and M. Kumazawa. 1985. “Garnet Phase of $MgSiO_3$ Filling the Pyroxene-Ilmenite Gap at Very High Temperature.” *Nature* 316 (6031): 803–5. doi:10.1038/316803a0.

Kawamoto, T. 1996. “Experimental Evidence for a Hydrous Transition Zone in the Early Earth’s Mantle.” *Earth and Planetary Science Letters* 142 (3–4): 587–92. doi:10.1016/0012-821X(96)00113-6.

Kennett, B.L.N., E.R. Engdah, and R. Buland. 1995. “Constraints on Seismic Velocities in the Earth from Traveltimes.” *Geophys. J. Int.* 122: 108–24.

King, H.E. Jr., and L.W. Finger. 1979. “Diffracted Beam Crystal Centering and Its Application to High-Pressure Crystallography.” *Journal of Applied Crystallography* 12 (Aug): 374–78. doi:10.1107/S0021889879012723.

King, S.D., D.J. Frost, and D.C. Rubie. 2015. “Why Cold Slabs Stagnate in the Transition Zone.” *Geology* 43 (3): 231–34. doi:10.1130/G36320.1.

Kohlstedt, D.L., H. Keppler, and D.C. Rubie. 1996. “Solubility of Water in the Α, β and γ Phases of $(Mg,Fe)_2SiO_4$.” *Contributions to Mineralogy and Petrology* 123 (4): 345–57. doi:10.1007/s004100050161.

Kono, Y., S. Gréaux, Y. Higo, H.Ohfuji, and T. Irifune. 2010. “Pressure and Temperature Dependences of Elastic Properties of Grossular Garnet up to 17 GPa and 1 650 K.” *Journal of Earth Science* 21 (5): 782–91. doi:10.1007/s12583-010-0112-2.

Kung, J., B. Li, T. Uchida, and Y. Wang. 2005. “In-Situ Elasticity Measurement for the Unquenchable High-Pressure Clinopyroxene Phase: Implication for the Upper Mantle.” *Geophysical Research Letters* 32 (1): 1–4. doi:10.1029/2004GL021661.

Kung, J., B. Li, T. Uchida, Y. Wang, D. Neuville, and R.C. Liebermann. 2004. “In Situ Measurements of Sound Velocities and Densities across the Orthopyroxene High-Pressure Clinopyroxene Transition in $MgSiO_3$ at High Pressure.” *Physics of the Earth and Planetary Interiors* 147 (1): 27–44. doi:10.1016/j.pepi.2004.05.008.

Lei, Q., J. Latham, C.Tsang, J. Xiang, and P. Lang. 2015. “Journal of Geophysical Research : Solid Earth,” no. Figure 1: 4784–4807. doi:10.1002/2014JB011736.Received.

Li, B., and D.R. Neuville. 2010. “Elasticity of Diopside to 8GPa and 1073K and Implications for the Upper Mantle.” *Physics of the Earth and Planetary Interiors* 183 (3–4). Elsevier B.V.: 398–403. doi:10.1016/j.pepi.2010.08.009.

Lin, C. 2004. “Pressure-Induced Polymorphism in Enstatite ($MgSiO_3$) at Room Temperature : Clinoenstatite and Orthoenstatite” 65: 913–21. doi:10.1016/j.jpcs.2003.09.028.

Liu, J., G. Chen, G.D. Gwanmesia, and R.C. Liebermann. 2000. “Elastic Wave Velocities of Pyrope – Majorite Garnets ($Py_{62}Mj_{38}$ and $Py_{50}Mj_{50}$) to 9GPa.” *Physics of the Earth and Planetary Interiors* 120: 153–63.

Liu, Z., J. Park, and S.I. Karato. 2016. “Seismological Detection of Low-Velocity Anomalies Surrounding the Mantle Transition Zone in Japan Subduction Zone.” *Geophysical Research Letters* 43 (6): 2480–87. doi:10.1002/2015GL067097.

Liu, Z., J. Park, and S.I. Karato. 2018. “Seismic Evidence for Water Transport out of the Mantle Transition Zone beneath the European Alps.” *Earth and Planetary Science Letters* 482. Elsevier B.V.: 93–104. doi:10.1016/j.epsl.2017.10.054.

Lu, C., Z. Mao, J.F. Lin, K.K. Zhuravlev, S.N. Tkachev, and V.B. Prakapenka. 2013. “Elasticity of Single-Crystal Iron-Bearing Pyrope up to 20GPa and 750K.” *Earth and Planetary Science Letters* 361. Elsevier: 134–42. doi:10.1016/j.epsl.2012.11.041.

Malitson, I.H. 1965. “Interspecimen Comparison of the Refractive Index of Fused Silica.” *Journal of the Optical Society of America* 55 (10): 1205. doi:10.1364/JOSA.55.001205.

Mao, H.K., J. Xu, and P.M. Bell. 1986. “Calibration of the Ruby Pressure Gauge to 800 Kbar under Quasi-Hydrostatic Conditions.” *Journal of Geophysical Research* 91 (B5): 4673–76. doi:10.1029/JB091iB05p04673.

Mao, Z., J. Lin, S.D. Jacobsen, T.S. Duffy, Y. Chang, J.R. Smyth, D.J. Frost, E.H. Hauri, and V.B. Prakapenka. 2012. “Sound Velocities of Hydrous Ringwoodite to 16GPa and 673K.” *Earth and Planetary Science Letters* 331–332 (May). Elsevier B.V.: 112–19. doi:10.1016/j.epsl.2012.03.001.

Marple, D.T.F. 1964. “Refractive Index of ZnSe, ZnTe, and CdTe.” *Journal of Applied Physics* 35 (3): 539. doi:10.1063/1.1713411.

McCammon, C.A., and N.L. Ross. 2003. “Crystal Chemistry of Ferric Iron in (Mg, Fe)(Si,Al)O3 Majorite with Implications for the Transition Zone.” *Phys Chem Minerals* 30: 206–16. doi:10.1007/s00269-003-0309-3.

Milani, S., R.J. Angel, L. Scandolo, M.L. Mazzucchelli, T.B. Ballaran, S. Klemme, M.C. Domeneghetti, et al. 2017. “Thermo-Elastic Behavior of Grossular Garnet at High Pressures and Temperatures.” *American Mineralogist* 102 (4): 851–59. doi:10.2138/am-2017-5855.

Montagner, J.P., and D.L. Anderson. 1989. “Constrained Reference Mantle Model.” *Physics of the Earth and Planetary Interiors* 58 (2–3): 205–27. doi:10.1016/0031-9201(89)90055-1.

Mookherjee, M., and S. Karato. 2010. “Solubility of Water in Pyrope-Rich Garnet at High Pressures and Temperature.” *Geophysical Research Letters* 37 (3): n/a-n/a. doi:10.1029/2009GL041289.

Moore, R.O., and J.J. Gurney. 1985. “Pyroxene Solid Solution in Garnets Included in Diamond.” *Nature* 314: 435–38. doi:10.1038/316507a0.

Morimoto, N., J. Fabries, A.K. Ferguson, I.V. Ginzburg, M. Ross, F.A. Seifeit, and J. Zussman. 1989. “Nomenclature of Pyroxenes.” *Canadian Mineralogist* 2 (5): 198–221.

Murakami, M., S.V. Sinogeikin, K. Litasov, E. Ohtani, and J.D. Bass. 2008. “Single-Crystal Elasticity of Iron-Bearing Majorite to 26 GPa: Implications for Seismic Velocity Structure of the Mantle Transition Zone.” *Earth and Planetary Science Letters* 274 (3–4): 339–45. doi:10.1016/j.epsl.2008.07.045.

Nestola, F., Marcello M., Paolo N., Matteo P., Maya K., A. De Stefano, M. Longo, L. Ziberna, and M. Manghnani. 2012. “In Situ Analysis of Garnet Inclusion in Diamond Using Single-Crystal X-Ray Diffraction and X-Ray Micro-Tomography.” *European Journal of Mineralogy* 24 (4): 599–606. doi:10.1127/0935-1221/2012/0024-2212.

Nestola, F., M. Tribaudino, and T.B. Ballaran. 2004. “High Pressure Behavior, Transformation and Crystal Structure of Synthetic Iron-Free Pigeonite.” *American Mineralogist* 89: 189–96.

Nichols, G., and C.S. Frampton. 1998. “Physicochemical Characterization of the Orthorhombic Polymorph of Paracetamol Crystallized from Solution.” *Journal of Pharmaceutical Sciences* 87 (6): 684–93. doi:10.1021/js970483d.

Nichols, G. 1998. “Optical Properties of Polymorphic Forms I and II of Paracetamol.” *Microscope* 46:3: 117–22.

Nishi, M., T. Kato, T. Kubo, and T. Kikegawa. 2008. “Survival of Pyropic Garnet in Subducting Plates.” *Physics of the Earth and Planetary Interiors* 170 (3–4): 274–80. doi:10.1016/j.pepi.2008.03.013.

Nishihara, Y., I. Aoki, E. Takahashi, K.N. Matsukage, and K.I. Funakoshi. 2005. “Thermal Equation of State of Majorite with MORB Composition.” *Physics of the Earth and Planetary Interiors* 148 (1): 73–84. doi:10.1016/j.pepi.2004.08.003.

Nye, J.F. 1985. *Physical Properties of Crystals: Their Representation by Tensorss and Matrices.* Oxford university press.

Ohtani, E., N. Kagawa, and K. Fujino. 1991. “Stability of Majorite (Mg,Fe)SiO_3 at High Pressures and 1800°C.” *Earth and Planetary Science Letters* 102: 158–66.

Ong, C.K.S., R.A. Seymour, P. Lirk, and A.F. Merry. 2010. “Combining Paracetamol (Acetaminophen) with Nonsteroidal Antiinflammatory Drugs: A Qualitative Systematic Review of Analgesic Efficacy for Acute Postoperative Pain.” *Anesthesia and Analgesia* 110 (4): 1170–79. doi:10.1213/ANE.0b013e3181cf9281.

Pacalo, R.E.G., and D.J. Weidner. 1997. “Elasticity of Majorite , $MgSiO_3$ Tetragonal Garnet.” *Physics of the Earth and Planetary Interiors* 1 (96).

Pakhomova, A., L. Ismailova, E. Bykova, M. Bykov, T.B. Ballaran, and L. Dubrovinsky. 2017. “A New High-Pressure Phase Transition in Clinoferrosilite: In Situ Single-Crystal X-Ray Diffraction Study.” *American Mineralogist* 102 (3): 666–73. doi:10.2138/am-2017-5853.

Pamato, M.G., A. Kurnosov, T.B. Ballaran, D.J. Frost, L. Ziberna, M. Giannini, S. Speziale, S.N. Tkachev, K.K. Zhuravlev, and V.B. Prakapenka. 2016. “Single Crystal Elasticity of Majoritic Garnets: Stagnant Slabs and Thermal Anomalies at the Base of the Transition Zone.” *Earth and Planetary Science Letters* 451. Elsevier B.V.: 114–24. doi:10.1016/j.epsl.2016.07.019.

Pamato, M.G. 2014. “Single Crystal Elasticity of Transition Zone and Lower Mantle Phases.”

Panero, W.R., J.S. Pigott, D.M. Reaman, J.E. Kabbes, and Z. Liu. 2015. “Dry (Mg,Fe)SiO_3 Perovskite in the Earth’s Lower Mantle.” *Journal of Geophysical Research: Solid Earth* 120 (2): 894–908. doi:10.1002/2014JB011397.

Pearson, D.G., F.E. Brenker, F. Nestola, J. McNeill, L. Nasdala, M.T. Hutchison, S. Matveev, et al. 2014. “Hydrous Mantle Transition Zone Indicated by Ringwoodite Included within Diamond.” *Nature* 507 (7491). Nature Publishing Group: 221–24. doi:10.1038/nature13080.

Perdew, J.P., K. Burke, and M. Ernzerhof. 1996. “Generalized Gradient Approximation Made Simple.” *Physical Review Letters* 77 (18): 3865–68. doi:10.1103/PhysRevLett.77.3865.

Pigott, J.S., K. Wright, J.D. Gale, and W.R. Panero. 2015. “Calculation of the Energetics of Water Incorporation in Majorite Garnet.” *American Mineralogist* 100 (5–6): 1065–75. doi:10.2138/am-2015-5063.

Plonka, A.M., P. Dera, P. Irmen, M.L. Rivers, L. Ehm, and J.B. Parise. 2012. “B -Diopside , a New Ultrahigh-Pressure Polymorph of $CaMgSi_2O_6$ with Six-Coordinated Silicon.” *Geophys. Res. Lett.* 39: 2000–2003. doi:10.1029/2012GL054023.

Prescher, C., and V.B. Prakapenka. 2015. “DIOPTAS : A Program for Reduction of Two-Dimensional X-Ray Diffraction Data and Data Exploration High Pressure Research : An.” *High Pressure Research* 35 (November): 223–30. doi:10.1080/08957959.2015.1059835.

Qin, F., X. Wu, D. Zhang, S. Qin, and S.D. Jacobsen. 2017. “Thermal Equation of State of Natural Ti-Bearing Clinohumite.” *Journal of Geophysical Research: Solid Earth* 122 (11): 8943–51. doi:10.1002/2017JB014827.

Reuss, A. 1929. “A. Reuss, Z. Angew. Math. Mech. 9, 49 (1929).” *Z. Angew. Math. Mech.* 9: 49.

Ringwood, A.E. 1967. “The Pyroxene-Garnet Transformation in the Earth’s Mantle” 2: 255–63.

Ringwood, A.E, and A. Major. 1971. “Synthesis of Majorite and Other High Pressure Garnets and Perovskites.” *Earth and Planetary Science Letters* 12: 411–18.

Ringwood, A.E. 1976. “Phase Transformations in Descending Plates and Implications for Mantle Dynamics.” *Tectonophysics* 32 (1–2): 129–43. doi:10.1016/0040-1951(76)90089-5.

Rivers, M.L, V.B. Prakapenka, A. Kubo, C. Pullins, C.M. Hall, S.D. Jacobsen, C. Holl, and S.D .Jacobsen. 2008. “The COMPRES/GSECARS Gas Loading System for Diamond Anvil Cells at the Advanced Photon Source.” *High Pressure Research* 28 (3): 273–92. doi:10.1080/08957950802333593.

Rodney, W.S., and R.J. Spindler. 1954. “Index of Refraction of Fused Quartz Glass for Ultraviolet, Visible, and Infrared Wavelengths.” *Journal of the Optical Society of America* 44 (9): 677. doi:10.1364/JOSA.44.000677.

Ross, N.L, and B. Reynard. 1999. “The Effect of Iron on the $P2_1/c$ to $C2/c$ Transition in $(Mg,Fe)SiO_3$ Clinopyroxenes.” *European Journal of Mineralogy* 11 (3): 585–89.

Rossman, G.R., and R.D. Aines. 1991. “The Hydrous Components in Garnets: Grossular-Hydrogrossular.” *American Mineralogist* 76 (7–8): 1153–64.

Saal, A.E., E.H. Hauri, C.H. Langmuir, and M.R. Perfit. 2002. “Vapour Undersaturation in Primitive Mid-Ocean Ridge Basalt and the Volatile Content of the Earth's Upper Mantle.” *Nature* 419 (October): 451–55.

Saylor, C.P. 1935. “Accuracy of Microscopical Methods for Determining Refractive Index by Immersion.” *Journal of Research of the National Bureau of Standards* 15: 277–94.

Schmandt, B., S.D. Jacobsen, T.W. Becker, Z. Liu, and K.G. Dueker. 2014. “Dehydration Melting at the Top of the Lower Mantle.” *Science* 344 (6189): 1265–68. doi:10.1126/science.1249850.

Shearer, P.M. 1990. “Seismic Imaging of the Upper Mantle Structure with New Evidence for a 520-Km Discontinuity.” *Nature* 344: 121–26. doi:10.1038/346183a0.

Sheldrick, G.M. 2008. “A Short History of SHELX.” *Acta Cryst* A64: 112–22.

Shinmei, T., N. Tomioka, K. Fujino, K.Kuroda, and T. Irifune. 1999. “In Situ X-Ray Diffraction Study of Enstatite up to 12 GPa and 1473 K and Equations of State.” *Amer. Mineral.* 84 (10): 1588–94.

Shiraki, K., N. Kuroda, H. Urano, and S. Maruyama. 1980. “Clinoenstatite in Boninites from the Bonin Islands, Japan.” *Nature* 285: 31–32.

Sinogeikin, S.V., and J.D. Bass. 2000. “Single-Crystal Elasticity of Pyrope and MgO to 20 GPa by Brillouin Scattering in the Diamond Cell.” *Physics of the Earth and Planetary Interiors* 120 (1–2): 43–62. doi:10.1016/S0031-9201(00)00143-6.

Sinogeikin, S.V., and J.D. Bass. 2002. “Elasticity of Majorite and a Majorite-Pyrope Solid Solution to High Pressure: Implications for the Transition Zone.” *Geophysical Research Letters* 29 (2): 1017. doi:10.1029/2001GL013937.

Sinogeikin, S.V., and J.D. Bass. 2002. “Elasticity of Pyrope and Majorite-Pyrope Solid Solutions to High Temperatures.” *Earth and Planetary Science Letters* 203: 549–55.

Skinner, B.J. 1956. “Physical Properties of End-Members of the Garnet Group.” *American Mineralogist* 41 (360): 428–36.

Smith, J.V., and B. Mason. 1970. “Pyroxene-Garnet Transformation in Coorara Meteorite.” *Science, New Series* 168 (3933): 832–33.

Smyth, J.R. 1987. “B-Mg_2SiO_4: A Potential Host for Water in the Mantle?” *American Mineralogist* 72: 1051–55.

Stixrude, L., and C. Lithgow-Bertelloni. 2011. “Thermodynamics of Mantle Minerals - II. Phase Equilibria.” *Geophysical Journal International* 184 (3): 1180–1213. doi:10.1111/j.1365-246X.2010.04890.x.

Stixrude, L., and C. Lithgow-Bertelloni. 2005. “Thermodynamics of Mantle Minerals - I. Physical Properties.” *Geophysical Journal International* 162 (2): 610–32. doi:10.1111/j.1365-246X.2005.02642.x.

Suzuki, I., and O.L. Anderson. 1983. “Elasticity and Thermal Expansion of a Natural Garnet up to 1,000 K.” *Journal of Physics of the Earth* 31 (2): 125–38. doi:10.4294/jpe1952.31.125.

Thomas, SM, K. Wilson, M. Koch-Muller, E.H. Hauri, C. McCammon, S.D. Jacobsen, J.D. Lazarz, et al. 2015. “Quantification of Water in Majoritic Garnet †.” *American* 100: 1084–92.

Toby, B.H., and R.B. Von Dreele. 2013. “GSAS-II: The Genesis of a Modern Open-Source All Purpose Crystallography Software Package.” *Journal of Applied Crystallography* 46 (2). International Union of Crystallography: 544–49. doi:10.1107/S0021889813003531.

Toms, L., H.J. McQuay, S. Derry, R.A. Moore. 2008. “Single Dose Oral Paracetamol (Acetaminophen) for Postoperative Pain in Adults.” *Cochrane Database of Systematic Reviews*, no. 4: CD004602. doi:10.1002/14651858.CD004602.pub2.

Tribaudino, M., F. Nestola, C. Meneghini, and G.D. Bromiley. 2003. “The High-Temperature P2/C1-C2/c Phase Transition in Fe-Free Ca-Rich P21/c Clinopyroxenes.” *Physics and Chemistry of Minerals* 30 (9): 527–35. doi:10.1007/s00269-003-0338-y.

Tribaudino, M., M. Prencipe, M. Bruno, and D. Levy. 2000. “High-Pressure Behaviour of Ca-Rich C2/c Clinopyroxenes along the Join Diopside-Enstatite ($CaMgSi_2O_6$-$Mg_2Si_2O_6$).” *Physics and Chemistry of Minerals* 27 (9): 656–64. doi:10.1007/s002690000106.

Tribaudino, M., M. Prencipe, F. Nestola, and M. Hanfland. 2001. “A P21/c-C2/c High-Pressure Phase Transition in $Ca_{0.5}Mg_{1.5}Si_2O_6$ Clinopyroxene.” *American Mineralogist* 86 (7–8): 807–13.

Ulmer, P., and R. Stalder. 2001. “The $Mg(Fe)SiO_3$ Orthoenstatite-Clinoenstatite Transitions at High Pressures and Temperatures Determined by Raman-Spectroscopy on Quenched Samples.” *American Mineralogist* 86 (10): 1267–74. http://www.intl-ammin.geoscienceworld.org/content/86/10/1267.short.

Van Mierlo, W.L., F. Langenhorst, D.J. Frost, and D.C. Rubie. 2013. “Stagnation of Subducting Slabs in the Transition Zone due to Slow Diffusion in Majoritic Garnet.” *Nature Geoscience* 6 (5). Nature Publishing Group: 400–403. doi:10.1038/ngeo1772.

Voigt, W. 1928. “Handbook of Crystal Physics.” *Teubner, Leipzig.*

Wang, Yanbin, Donald J Weidner, Jianzhong Zhang, Gabriel D Gwanrnesia, and Robert C Liebermann. 1998. “Thermal Equation of State of Garnets along the Pyrope-Majorite Join.” *Physics of the Earth and Planetary Interiors* 105: 59–71.

Wange, F., M. Barklage, X. Lou, S. van der Lee, C.R. Bina, and S.D. Jacobsen. n.d. “HyMaTZ: A Python Program for Modelling Seismic Velocities in Hydrous Regions of the Mantle Transition Zone.” *(In Prep)*.

Webb, S.L., and I. Jackson. 1990. “Polyhedral Rationalization of Variation among the Single-Crystal Elastic Moduli for the Upper-Mantle Silicates Garnet, Olivine, and Orthopyroxene.” *American Mineralogist* 75 (7–8): 731–38.

Wood, B.J., and D.C. Rubie. 1996. “The Effect of Alumina on Phase Transformations at the 660-Kilometer Discontinuity from Fe-Mg Partitioning Experiments.” *Science (New York, N.Y.)* 273 (September): 1522–24. doi:10.1126/science.273.5281.1522.

Xu, W., C. Lithgow-Bertelloni, L. Stixrude, and J. Ritsema. 2008. “The Effect of Bulk Composition and Temperature on Mantle Seismic Structure.” *Earth and Planet. Sci. Lett.* 275: 70–79.

Xu, W., C. Lithgow-Bertelloni, L. Stixrude, and J. Ritsema. 2008. “The Effect of Bulk Composition and Temperature on Mantle Seismic Structure.” *Earth and Planetary Science Letters* 275 (1–2): 70–79. doi:10.1016/j.epsl.2008.08.012.

Yagi, T., M. Akaogi, O. Shimomura, H. Tamai, and S. Akimoto. 1987. “High Pressure and High Temperature Equations of State of Majorite.” *High-Pressure Research in Mineral Physics*, 141–47. http://www.mhtl.uwaterloo.ca/courses/me354/lectures/pdffiles/ch2.pdf.

Yanbin W., T. Gasparik, and R.C. Liebermann. 1993. “Modulated Microstructure in Synthetic Majorite.” *American Mineralogist* 78 (11–12): 1165–73.

Yoshino, T., Yu Nishihara, and S.I Karato. 2007. “Complete Wetting of Olivine Grain Boundaries by a Hydrous Melt near the Mantle Transition Zone.” *Earth and Planetary Science Letters* 256 (3–4): 466–72. doi:10.1016/j.epsl.2007.02.002.

Yu, Y.G., and R.M. Wentzcovitch. 2009. “Low-Pressure Clino- to High-Pressure Clinoenstatite Phase Transition: A Phonon-Related Mechanism.” *American Mineralogist* 94 (4): 461–66. doi:10.2138/am.2009.3071.

Zhang, L., H. Ahsbahs, and A. Kutoglu. 1998. “Hydrostatic Compression and Crystal Structure of Pyrope to 33 GPa.” *Physics and Chemistry of Minerals* 25 (4): 301–7. doi:10.1007/s002690050118.

Zhang, L., H. Ahsbahs, S.S. Hafner, and A. Kutoglu. 1997. “Single-Crystal Compression and Crystal Structure of Clinopyroxene up to 10 GPa.” *American Mineralogist* 82 (3–4): 245–58. doi:10.2138/am-1997-3-402.

Zhang, Z., K.G. Dueker, and H.H. Huang. 2018. “Ps Mantle Transition Zone Imaging beneath the Colorado Rocky Mountains: Evidence for an Upwelling Hydrous Mantle.” *Earth and Planetary Science Letters* 492. Elsevier B.V.: 197–205. doi:10.1016/j.epsl.2018.03.044.

Zou, Y., S. Gréaux, T. Irifune, M.L. Whitaker, T. Shinmei, and Y. Higo. 2012. “Thermal Equation of State of $Mg_3Al_2Si_3O_{12}$ pyrope Garnet up to 19 GPa and 1,700 K.” *Physics and Chemistry of Minerals* 39 (7): 589–98. doi:10.1007/s00269-012-0514-z.

7. Appendices

Appendix A

Derivation of Joel's equation from Bloss (1981).

Given a biaxial indicatrix with origin O and semiaxes OX, OY, and OZ:

$$|\overline{OX}| = \alpha \qquad [a.1a]$$

$$|\overline{OY}| = \beta \qquad [a.1b]$$

$$|\overline{OZ}| = \gamma \qquad [a.1c]$$

Let x,y,z represent rectangular coordinates of any point on the surface of an ellipsoid.

The equation for the ellipsoid that is then:

$$\frac{x^2}{\alpha^2} + \frac{y^2}{\beta^2} + \frac{z^2}{\gamma^2} = 1 \qquad [a.2]$$

Let **v** represent an arbitrary vibration direction with direction cosines r,s,t relative to X,Y,Z.

$$cos\theta_x = r \qquad [a.3a]$$

$$cos\theta_y = s \qquad [a.3b]$$

$$cos\theta_z = t \qquad [a.3c]$$

For light vibrating parallel to **v** :

$$|\boldsymbol{v}| = n \qquad [a.4]$$

Where *n* is the crystal's refractive index for light vibrating parallel to **v**. Rectangular coordinates for the point, *v*, where **v** intersects the ellipsoid relative to X,Y,Z must equal nr, ns, nt in order for equations a.3a-3c to hold true.

Substituting coordinates nr,ns, and nt for x,y,z in equation a.2:

$$\frac{r^2}{\alpha^2} + \frac{s^2}{\beta^2} + \frac{t^2}{\gamma^2} = \frac{1}{n^2} \qquad [a.5]$$

Relative to X,Y, and Z, if a biaxial (+) crystal's optic axis a_l has direction cosines (r_l,0,t_l), then its second optic axis, a_2, will have direction cosines (-r_l,0,t_l). Let line C_l lie perpendicular to a_l and be in the XZ plane. C_l will then have direction cosines (-t_l,0,r_l). Line C_l then, being perpendicular to optical axis a_l, lies in the circular cross section and has length β. Substituting the values of C_l into equation a.5:

$$\frac{(-t_1)^2}{\alpha^2} + \frac{{r_1}^2}{\gamma^2} = \frac{1}{\beta^2} \qquad [a.6]$$

Direction cosines of a line relative to an orthogonal basis fulfill:

$$r^2 + s^2 + t^2 = 1 \qquad [a.7]$$

Following equation a.7 for C_l:

$$(-t_1)^2 + {r_1}^2 = 1 \qquad [a.8]$$

Combining equations a.6 and a.8:

$${t_1}^2\alpha^{-2} + (1 - {t_1}^2)\gamma^{-2} = \beta^{-2} \qquad [a.9]$$

After solving for t_l^2:

$${t_1}^2 = \frac{\beta^{-2}-\gamma^{-2}}{\alpha^{-2}-\gamma^{-2}} \qquad [a.10a]$$

Solving for r_l^2 using equations a.8 and a.10a:

$${r_1}^2 = 1 - {t_1}^2 = \frac{\alpha^{-2}-\beta^{-2}}{\alpha^{-2}-\gamma^{-2}} \qquad [a.10b]$$

Equation a.10a and a.10b relate the direction cosines for the optic axes to the refractive indices α, β, and γ.

Let a random vibration direction *v*, with direction cosines r,s,t, be at an angle ρ_1 to optic axis a_1, with direction cosines r_1, 0, t_1, and at ρ_2 to optic axis a_2, direction cosines $-r_1$, 0, t_1. The cosine of the angle between two lines is the sum of the products of their comparable direction cosines:

$$\cos\rho_1 = rr_1 + tt_1 \tag{a.11a}$$

$$\cos\rho_2 = -rr_1 + tt_1 \tag{a.11b}$$

$$\cos\rho_1 \cos\rho_2 = -r^2{r_1}^2 + t^2{t_1}^2 \tag{a.11c}$$

Substituting equations a.10a and a.10b into equation a.11c:

$$(\alpha^{-2} - \gamma^{-2})\cos\rho_1 \cos\rho_2 = -r^2\alpha^{-2} + (r^2 + t^2)\beta^{-2} - t^2\gamma^{-2} \tag{a.12}$$

Following equation 7, $r^2 + t^2 = 1 - s^2$, equation a.12 can be simplified:

$$(\alpha^{-2} - \gamma^{-2})\cos\rho_1 \cos\rho_2 = \beta^{-2} - (r^2\alpha^{-2} + s^2\beta^{-2} + t^2\gamma^{-2}) \tag{a.13}$$

Substituting n^{-2} into equation a.13 using equation a.5:

$$\cos\rho_1 \cos\rho_2 = \frac{\beta^{-2} - n^{-2}}{\alpha^{-2} - \gamma^{-2}} \tag{a.14}$$

Given an equivibration pair p and q, two different vibration directions for which the crystal will exhibit the same refractive index n_1. Let their angles to optic axes a_1 and a_2 be ρ_{p1} and ρ_{p2} as well as ρ_{q1} and ρ_{q2}. Following equation a.14:

$$\cos\rho_{p1}\cos\rho_{p2} = \frac{\beta^{-2} - n^{-2}}{\alpha^{-2} - \gamma^{-2}}$$

$$\cos\rho_{q1}\cos\rho_{q2} = \frac{\beta^{-2} - n^{-2}}{\alpha^{-2} - \gamma^{-2}}$$

Therefore:

$$\cos\rho_{p1}\cos\rho_{p2} = \cos\rho_{q1}\cos\rho_{q2} \qquad [a.15]$$

Performing the vector dot product results in Joel's equation:

$$(\mathbf{q}\cdot\mathbf{a_1})(\mathbf{q}\cdot\mathbf{a_2}) = (\mathbf{p}\cdot\mathbf{a_1})(\mathbf{p}\cdot\mathbf{a_2}) \qquad [a.16]$$

Where $\mathbf{a_1}$ and $\mathbf{a_2}$ are unit vectors along the two optic axes and **p** and **q** are unit vectors parallel to p and q.

According to equation 16, for any two equivibration directions the product of the cosines of their respective angles relative to the optical axes will be equal.

Appendix B

Standard Operating Procedures for Huber Diffractometer

Entering the Hutch


Hutch exterior light

Interlock System

- Check status of hutch exterior shutter light.
    - Light **ON** : X-ray shutter currently open. Do **NOT** enter! Experiment in progress.
    - Light **OFF** : X-ray shutter disabled. Entry permitted. (Possible experiment in progress. Check before entering.)

- Check status of interior post shutter light.
    - **RED ON** : X-rays inside hutch. Do **NOT** enter!
    - **GREEN ON** : Interlock enabled. Safety system monitoring hutch.
    - Red off : Safe to enter.

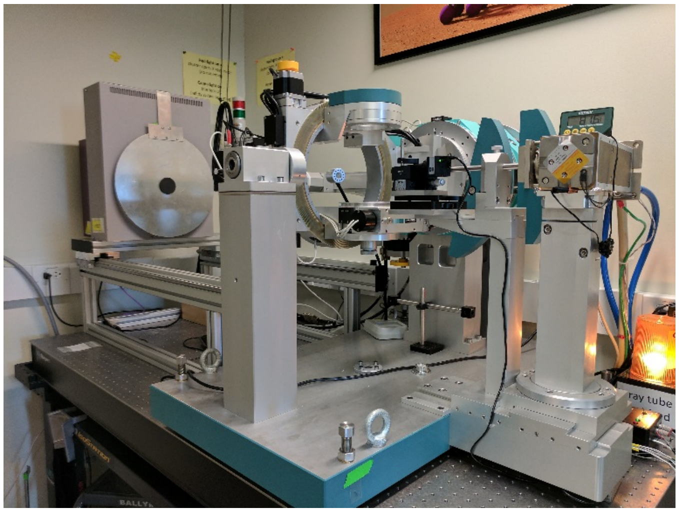


Interior post shutter light

The interlock system minimizes the risk of personal X-ray exposure. It works by preventing the X-ray shutter from opening unless the door is shut and the room is empty. The status of the door is monitored by switches, but the system has no way of detecting whether people are inside the room; it relies on us manually checking that the room is empty. There is a large red button outside the room and to the left of the door. This is used to tell the system that the room is empty. **You must only press this button when you are certain that there is nobody in the room.** If the door is not shut when you press the button, it will not do anything, and the X-ray shutter will remain locked. If the door is shut, the interlock will become active when you press the button, and the X-ray shutter will no longer be locked shut. A green light will appear in the far corner to signal that the shutter can now be opened by the controller when needed. Just above this light is a red light. This only lights up when the X-ray shutter is open. **If this red light is on when you are inside the room then you must leave the room immediately and close the door**.

Startup Procedure

Water chiller

- Turn water chiller on by turning power key to the right.

    A green ready light will illuminate when it is running properly. If the chiller does not turn on, check that the service disconnect on the wall near the chiller is on.

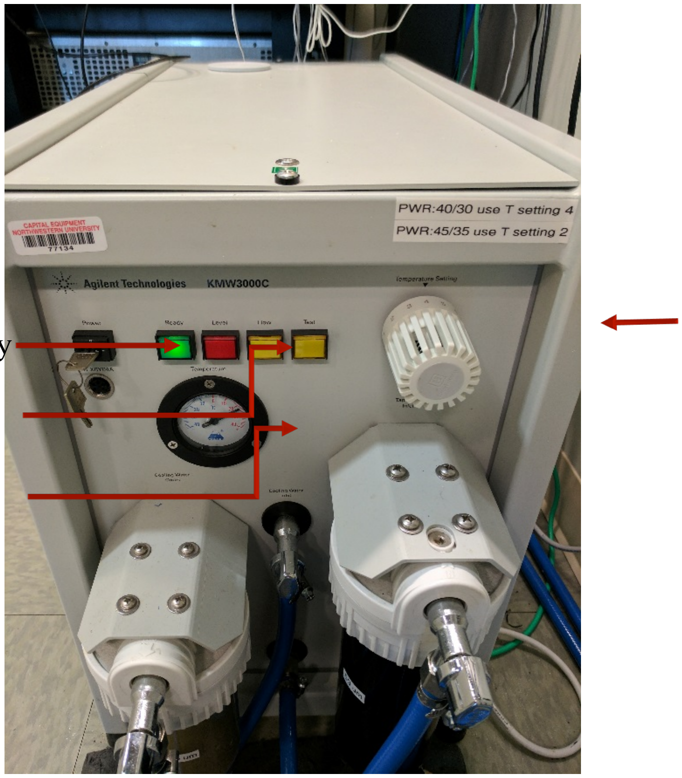

Power key

Ready light

Temperature readout

Water chiller temperature dial

- If running power supply at 40kV/30mA set chiller temperature to 4.
- If running power supply at 45kV/35mA set chiller temperature to 2.

Temperature readout should be around 22°C for optimal performance.

Note: 2 is colder than 4.

- Check that flow meter is spinning to be sure water is flowing through chiller.

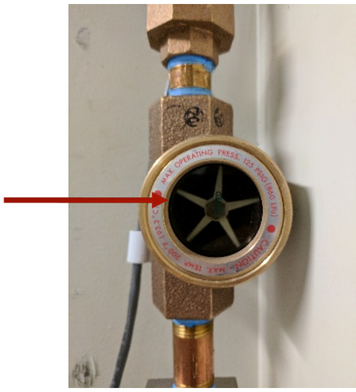

Flow

Shutter controller

The shutter control box power switch should be in the "On" position, switch set to "External/Digital". On the shutter relay box, be sure the power is "On" and the switch is set to "Huber".

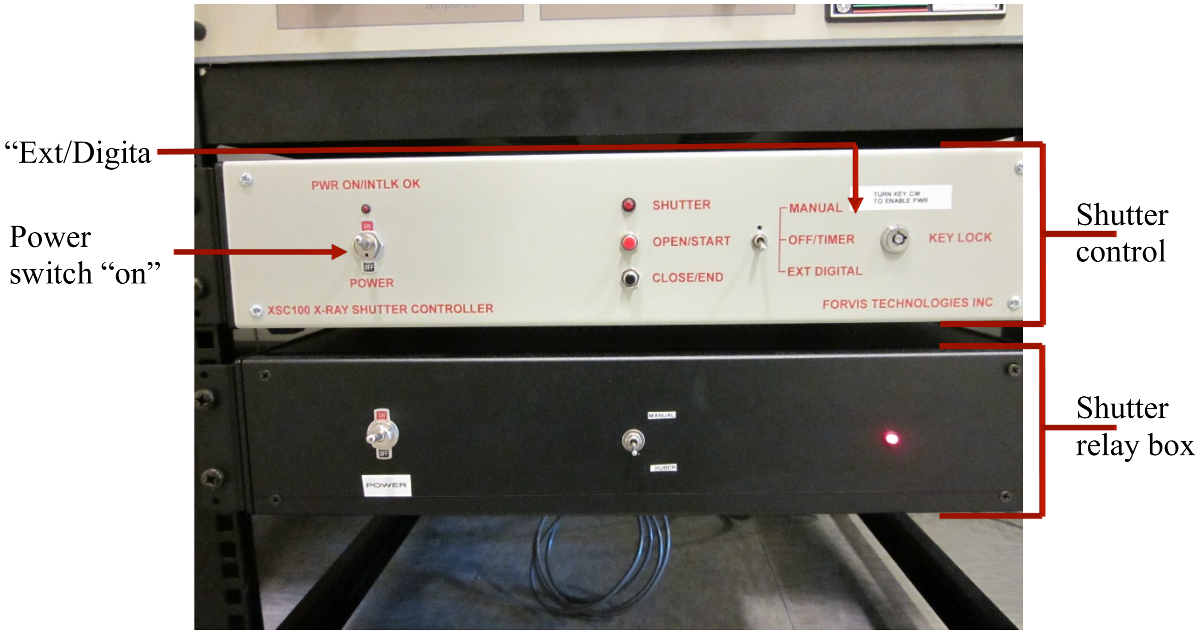

Power up the X-ray tube power supply.

- Press the "X-ray On" button on the X-Ray tube power supply (key must be turned to on).

To check the setting the generator will power up to press and hold the X-ray off button. The generator normally will power up to 15keV/8mA. Let the tube sit for 5-10 minutes at this setting. If there has been a power outage, then the generator would ramp to power it was at before the power outage. See trouble shooting section for further instructions on what to do in this situation.

Note: at each step, always increase kV first, then mA.

Reaching standard operating power:

-Raise voltage to 20 kV, then raise current to 10 mA, and wait a few minutes.

-Raise the voltage to 30 kV and current to 20 mA, and wait a few minutes.

-Raise the voltage to 40 kV and then current to 30 mA.

(Note: if needed, you may go up to 45kV/40mA, that's 1.8kW, but that is maximum).

Powering down:

-Do the reverse, bringing down mA first, then kV.

-30kV/20mA.

-20kV/10mA.

-15kV/8mA (let generator run for 5-10 minutes before shutting off the generator).

-Let water continue to run for 5-10 min before shutting off the water.

The intensity of the X-rays emitted from the X-ray tube is controlled by adjusting the current and voltage applied by the generator. The generator controls are located underneath the main bench, and allow for the manual control of both the current (mA) and voltage (kV) by turning the dials on the front panel. When the X-ray tube is not being used, the values should be at 8 mA and 15 kV. These are the **resting** state values. Typical **operating** values are 30 mA and 40 kV. Special care must be taken when ramping up from resting to operating values, and likewise when ramping down. There is a danger of the tungsten filament at the cathode overheating and melting if the current running through it becomes too high. The large voltage works to strip electrons from the filament, but if the current is too high relative to the voltage then this process may not be efficient, and could result in a buildup of electrons on the filament. To ensure that this situation is avoided, always remember to increase voltage first when ramping up, and to decrease current first when ramping down. It is also good practice to increase/decrease in increments when warming up from resting (*e.g.* 8–15, 10–20, 20–30, 30–40), with a few minutes of rest in between each increment.

<u>Interlock monitor</u>

Interlock monitor box displays status of chiller and thermal monitors. When all green, water is flowing and x-ray source temperature is within safe limits; power supply is functional. X-ray source temperature should not exceed 95° F.

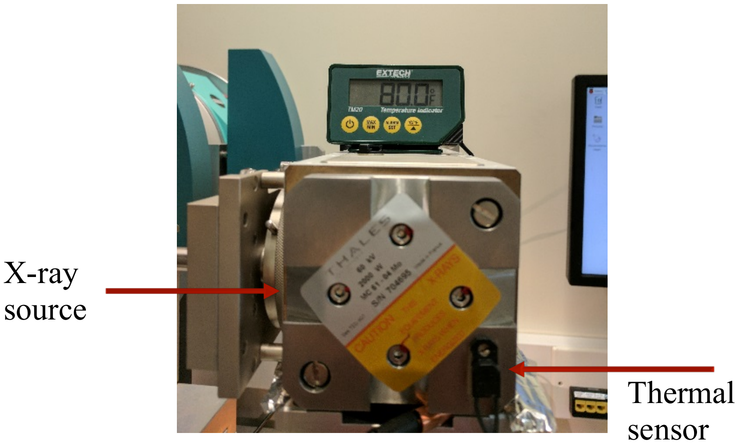

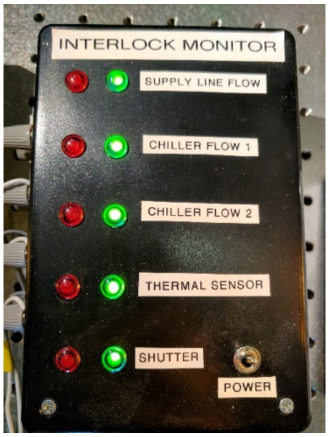

Experiment

Single

- Open Single2014 (26Oct2015) on Huber PC desktop.
    - Select “Real Diffractometer”
- Select appropriate .mat file for experiment.
    - If no appropriate .mat file exists create new .mat file by copying and re-naming an old one.

Sample Alignment

- Mount goniometer, with sample, onto Huber.
- Micrometer camera positions:
    - Air : 2.82
    - DAC : 3.32
    - How to read micrometer:

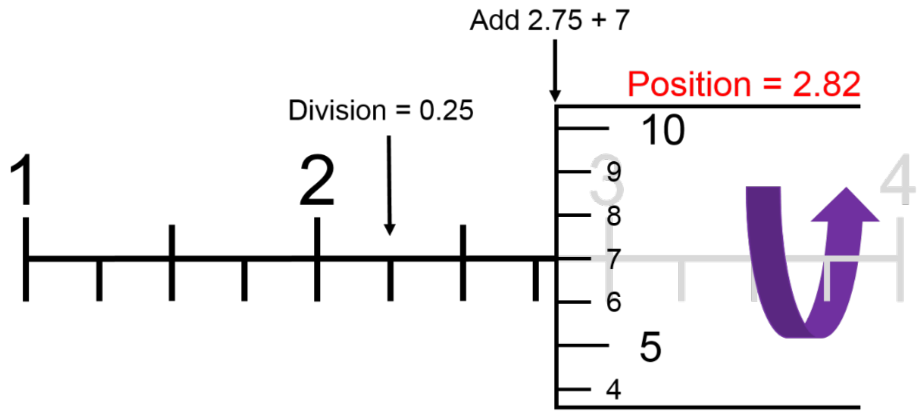

- Using Single, type: "view"
    - Sample is now aligned with camera.
        - Phi is at 20°
- After turning on viewing lamp, open camera software in hutch.
    - Open "Camera Software".
    - Select "Execute".
    - Double click camera in camera list.

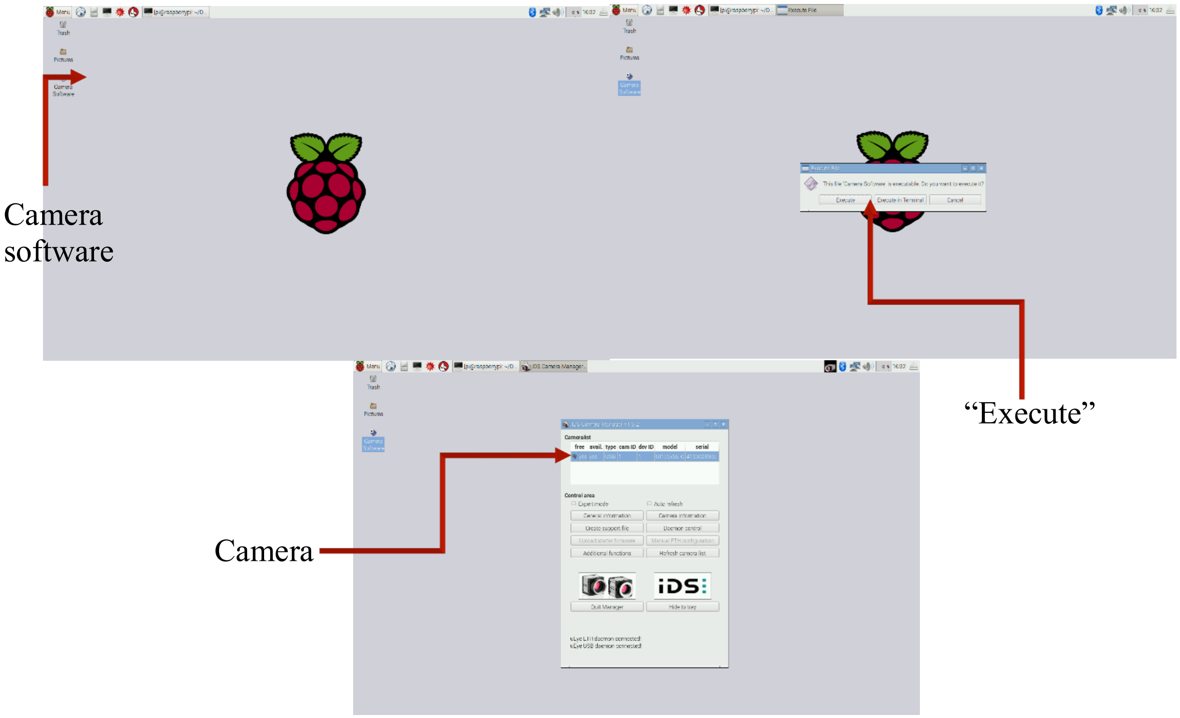

This file 'Camera Software' is executable. Do you want to execute it?

free	avail.	type	cam ID	dev ID	model	serial
yes	yes	USB	1	1	[illegible]	[illegible]

uEye ETH daemon connected!
uEye USB daemon connected!

- Adjust field of view by selecting 1:1 view ratio and scrolling all the way down on image.

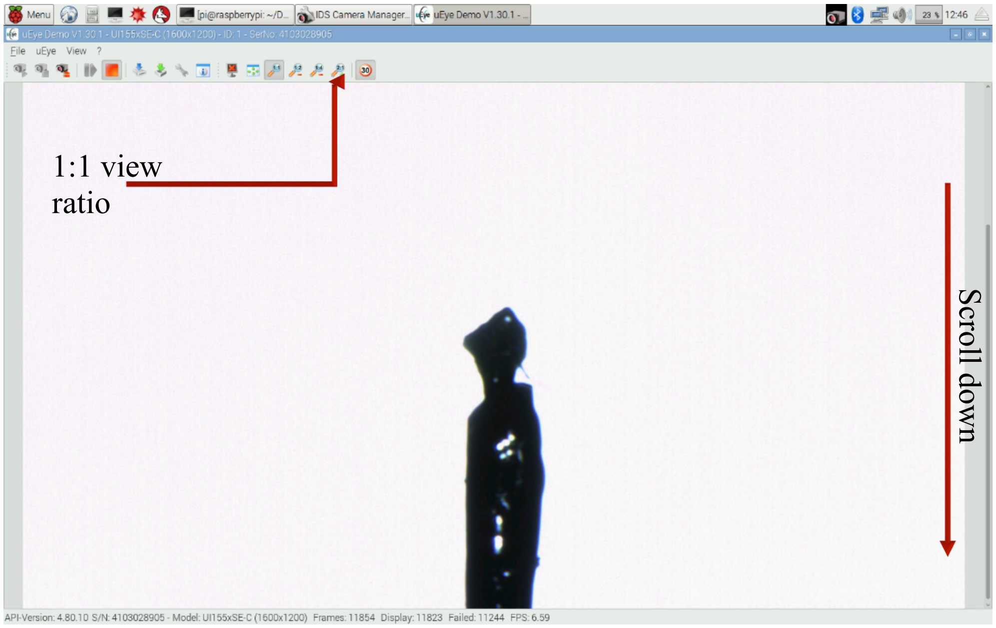

```
API-Version: 4.80.10 S/N: 4103028905 - Model: UI155xSE-C (1600x1200)  Frames: 11854  Display: 11823  Failed: 11244  FPS: 6.59
```

1:1 view ratio

Scroll down

- Using goniometer, move sample onto transparency central circle.
- In air sample:
    - Camera micrometer should read: 2.511

      (little notches are 0.001 increments)
    - Using Single hit enter to move to view position 2.
    - Using goniometer, center sample.
    - Repeat until sample no longer precesses.
- DAC sample:
    - Camera micrometer should read: 3.257
    - Using Single hit enter twice to rotate DAC 180°.
    - Make sure sample is still in focus. If not, move sample into focus using goniometer.
    - Repeat hitting enter twice and viewing until sample is always in focus and centered.
- Check that appropriate X-ray attenuation filter is in place.

  - Remove Zr filter for point detector measurements (Huber). Put the Zr filter in for area detector measurements (MAR).

- In Single, exit view mode.

<u>Exiting the hutch</u>

- If not using MAR345 make sure area detector cover is on.

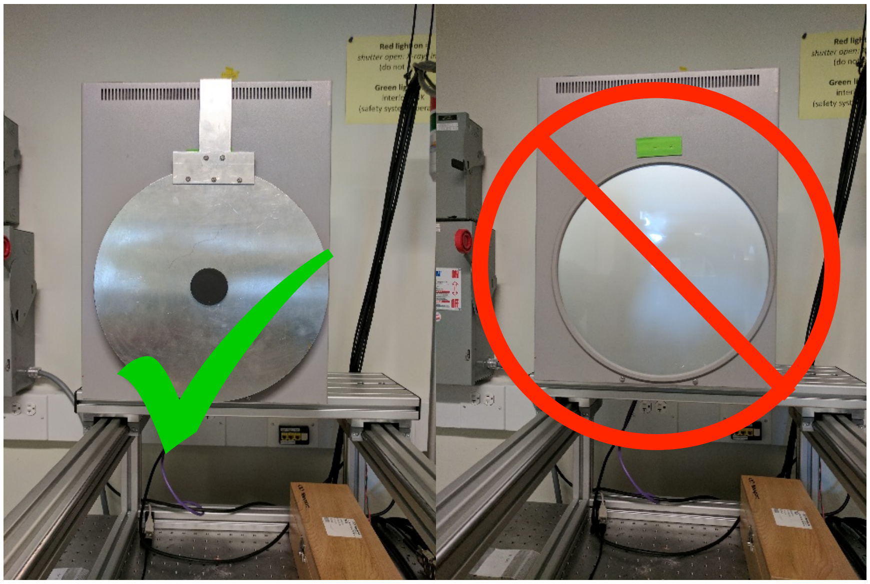

- Make sure MAR345 is pushed all the way towards the wall. For safety reasons there is a limit switch that if not engaged the Huber will not operate. To move the MAR loosen (DON”T unscrew) the black nob behind MAR and slide it down the rail.

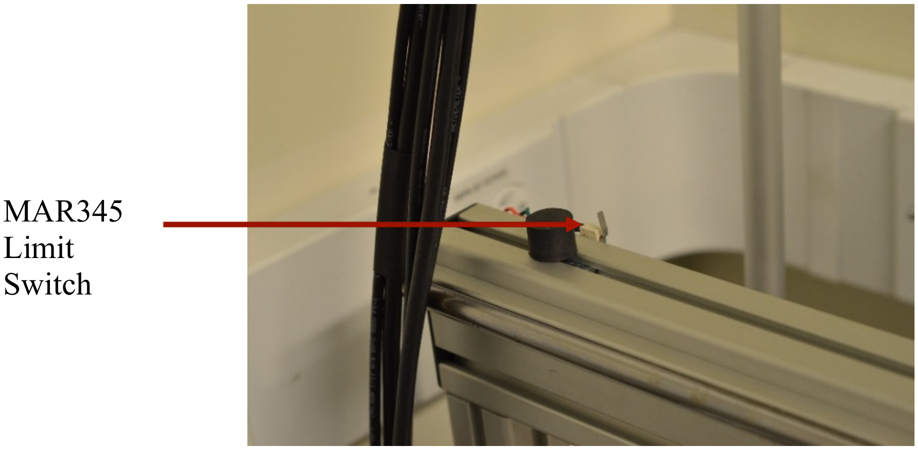

- Clear the hutch.

- Close the door.

- Enable interlocks by pressing red button. Only enable interlocks if hutch is clear (no people).

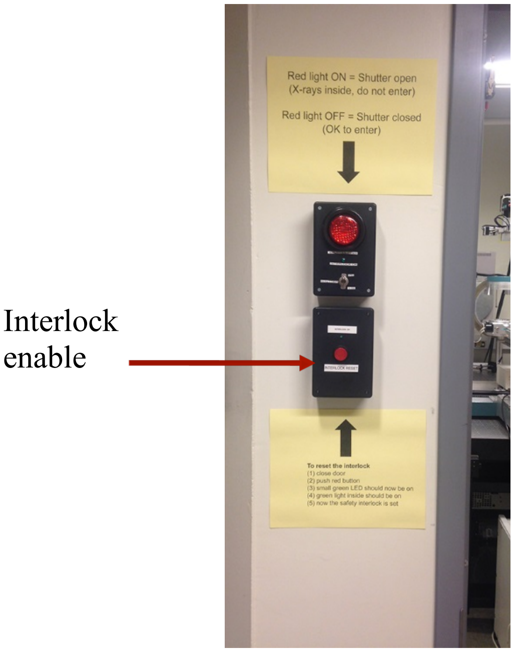

Single Zref

With camera mounted DO NOT drive omega past +30 and -25 degrees! Omega should also not be lower than 8 degrees as this is too close to the direct beam.

- In air :
    - Perform search using "srch" command.
        - Detector apertures: 9.0 9.0
        - Initial and final 2-theta: corresponds to a 2-theta of predicted peak.
        - Initial and final chi: 0 180
        - Initial and final phi and stepsize: 0 180 3
        - Count time per step and sig. level: 0.5 8
- In DAC:
    - Make sure Single is in DAC mode using "set dev".

  - Set psi to opening angle of DAC.
- Input found peaks into list using “inl”.
- Perform 2 position centering on found peaks using “cntr”.
  - For 1 position centering use “cent”.
- Once at least 2 peaks are centers compute orientation matrix using “com”.
- Using new orientation matrix insert desired peaks into list.
  - Insert individual hkl’s using “inh”.
  - Insert Laue families using “inl”.
- Perform zref (8-position centering) using command “zref”.
  - Continue with parameters: Y
  - Centering on calc positions or list angles: C
  - Chi order of measurement to be optimized: N
  - Do you want centering to continue after failures: Y
- Make required crystal offset corrections.
  - When making offset corrections move crystal in opposite direction (+/-) of what Single says.
  - Be sure camera software viewing ratio and position are correct.
  - Example:
    - Single: Xtal 0.006 -0.015 0.055
    - Move sample -0.006 x-direction +0.015 y-direction -0.055 z-direction.

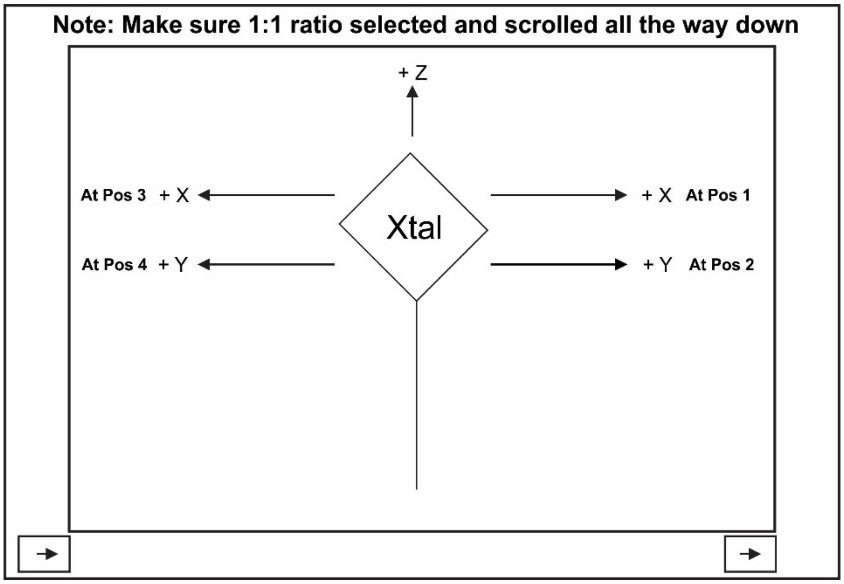

Data collections

- Manually enter UB matrix using single command “om”
- Set experiment title using “set title”.
- Create data file using “set datfile”.
- Set data collection parameters using “set data”.
    - Scan width: 0.6+0.35tan(theta)
    - Steps: 30
    - Step size: 0.02
    - Time: 1 sec./step
    - Only use omega scans
    - Single precision
    - Hemisphere to 45>theta

  - R(int) should be ~2%

    (parameters taken from Ross Angel email)

- Begin data collection using “dc s”.

MAR345 Procedure

MAR345 is an image plate detector with maximum scan radius of 345 mm. Images are read by spinning the phosphorous plate at high rpm which can be quite loud, do not be alarmed. The user will know that the readout process is complete when they hear the sound of a ping pong ball dropping. This is the solenoid locking the image plate into place. The image is erased via exposure to intense internal lights. In some cases if peak intensity is too high or collection time is too long the image may not erase immediately; erase multiple times. Do not erase detector while unit cover is off, lights are very bright! The front surface of the unit cover is made of very thin plastic do NOT touch! When MAR345 is not in use it is critical to cover the detector with lead shield! MAR345 along with MARIP PC are on loan from Mark Rivers, GSECARS.

Setup

- Bring 2theta to vertical (90°) position.
- Remove MAR345 cover.
- Install Zr filter.
- Mount beam-stop to chi ring.

Beam-stop

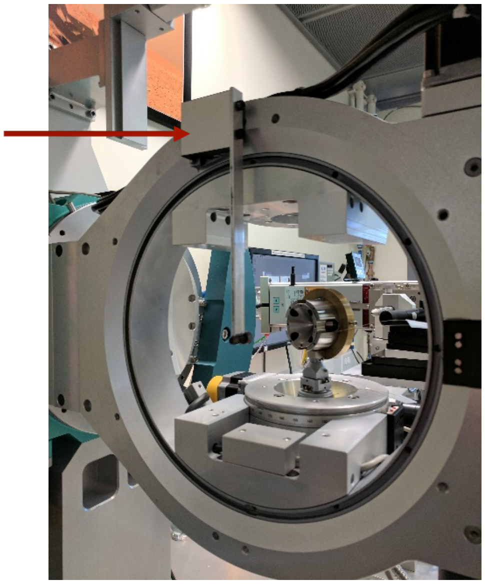

- Move MAR345 to appropriate distance.
    - Bring rubber backstop, furthest from wall, up behind the MAR carriage to lock carriage in place.

- Turn MAR345 on, if needed, using green button on back of detector.
- Make sure Huber controller is set to “network” communication mode.

  - On controller screen, press “t”.
  - Press “configure interface”.
  - Press interface button until it reads “network”.
    - “TCP port” should read “1234”.
- Secure and exit the hutch.

MAR345 control program

MAR Control is a program written to synchronize the MAR345 and Huber diffractometer. Its capabilities include: controlling detector modes, performing single exposure routines, performing automated data collections for single crystal experiments, shutter control, and providing a TCP client to pass commands directly to the Huber Controller.

- Using MARIP computer, open terminal.
    - User = MAR345
    - Pw: mar345

    Note: Use blue KVM switch to alternate between Huber and MARIP computers.
- Type (without quotes): “go1”
    - Press enter.
- Open a second terminal.
    - Type (without quotes): “go2”
        - Press enter.

    Note: The order in which go1 and go2 commands are executed matters.

        In order to stop a collection, hit ctrl c

Below is a list of various options and commands in MAR Control:

Change Mode

Mode selects the resolution to be used. The diameter of our detector is 345 mm, and so there are multiple options available (ex.: 345mm @ 0.10mm, and 345mm @ 0.15mm). The second value defines the pixel size of the scan, 0.10 mm would be higher resolution (3450 × 3450) than 0.15 mm (2300 × 2300). May want to use 2300. Lower resolutions can be useful when the intensity of diffraction is low, but normally we use the highest resolution, 345mm @ 0.10mm. Once you have selected the resolution, press the Change Mode button to send the command to the detector. The same command will be sent again when you first perform a scan at the new resolution. This is normal behavior.

Directory

This field defines where the scanned images will be saved. This directory must already exist, so be sure to create a new folder somewhere in the data directory before changing this entry.

Erase

This button sends a command to the MAR345 to erase the image on the plate. This should generally be run before each new exposure, even if the detector has been turned off for a long time. However, it won't damage the detector if this step is skipped.

Fast scan

Fast scan only applies to Integrate scan. If selected a single image will be captured which covers the entire phi range from data collection input parameters.

Img. number

This field defines the filename suffix, so that multiple scans can be carried out on the same sample without overwriting data. By default the iterate box is checked.

Integrate scan

For data collection this mode is preferable as it collects over a larger portion of reciprocal space than the collect mode. Images are collected over a phi range in this mode instead of at a single phi.

Iterate

Iterates image number as collection progresses so that images are not overwritten.

Open/Close

These buttons will open and close the X-ray shutter manually. The interlock system (see above) must be active for this to work.

Root

This field defines the prefix for the image filenames. Use something sensible like the date and sample code.

Scan

This button initiates a scan of the current exposure. It typically takes around a minute to scan the full image, during which time the motor inside the MAR345 will spin at an increasing rate. Once the scan is complete, a sound very much like a ping pong ball dropping will be heard.

TCP

Should **only** be used for trouble shooting. A TCP communication line is opened between MARIP computer and SMC9300 controller. Commands can be input in terminal window. If this TCP client is in use command buttons on GUI window will not work appropriately.

Time

If selected the shutter will remain open for entered time period in seconds. If not selected shutter will remain open until close button is pressed.

Calibrations

- Make sure the calibrant capillary has been mounted (LaB_6).
- Using MAR Control select the appropriate detector mode (resolution) from dropdown menu.
    a. Most likely: 3450 or 2300
- Press “Change Mode”.

Note: It is important to change mode at the beginning of every experiment.

- Erase the detector by pressing “Erase”.
- With the “Time” box checked, enter an exposure time. (240 seconds is recommended for LaB6)
- Press “Open” to begin exposure.
- Once exposure is complete enter the appropriate directory and image name.
- Press “Scan” to read out image.
- Process image using GSEADA or Dioptas on HuberPC.

Note: A new calibration should be taken every time the detector is moved.

Data collection

- Using MAR Control select the appropriate detector mode (resolution) from dropdown menu.
- Press “Change Mode”.
- In Data collection box:
    - Enter exposure time in seconds.
    - Enter the number of steps to take.
    - Enter phi starting position.
    - Enter step size to take in degrees.

  - Enter desired directory.
  - Enter sample name in “Root: ”.
  - Enter initial image number.

Note 1: When performing an integrated scan, if step size is too large for the input exposure time (required motor velocity is too high) the collection will still be performed. However, the motor steps will not be correct and shutter will not open at appropriate times. The SMC will not drive the motor too quickly.

Note 2: Image numbers must be in 3 digit format. Example: 001. Not: 1. The total number of images collected will be the initial image plus the number of steps. Also, GSEADA program requires the first image to not be image 000.

Note 3: Entered collection parameters are saved in “parameters.txt” file located in selected directory.

- Make sure “Iterate” is selected if desired.
- Press “Integrate Scan”.
- Process image using GSEADA or Dioptas on HuberPC.

Electronics

Computer rack

The computer rack holds:

- Huber PC
- MARIP PC
- Huber Power Pack

- SMC9300 programmable motor controller (Huber motor controller)
- Ratemeter

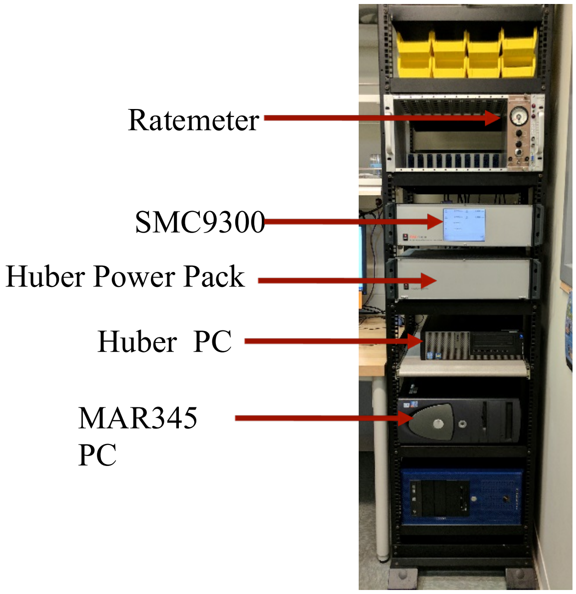

Powering up controller

ONLY USE the following procedure if the computer rack is powered down. This is sometimes is done during building maintenance to prevent damage.

- Turn on power pack.
- Turn on SMC9300
- Wait for controller to boot and load motor control GUI
- Check communication mode: serial/network
- Check motor zeros

If power is lost with motors out of park position when SMC9300 is restarted all current motor positions will be defined as zero degrees except for motors 5 and 6 which will read 2 and 9 respectively. To fix home all motors keeping the following notes in mind.

Note: If homing motors always home in the positive direction (negative to positive), except for Chi which should be in the negative direction.

Note: The Huber home position for chi is vertical (90 degrees). After being restarted this vertical is redefined as 0 degrees. This needs to be redefined so that Single will work properly. Do this by setting horizontal 2-theta to be 0 degrees. Re-initialize 2-theta to be called zero in the horizontal position. Using the SMC9300 controller, drive 2-theta to -90 (minus 90) degrees. This should be horizontal. Press the “zero” button under “t”, this will call the current position zero.

- Mot1, mot 2, and mot 3 will be in 3 decimal precision instead of the required 4. This can be fixed two different ways.
    - First method:
        - Using Single type DCOM
        - Input string:
            - dcpl1:4
            - dcpl2:4
            - dcpl3:4
        - Type exit dcom
        - Ldmt [Mot#] [Pos] to redefine chi

        - Ex. ldmt 3 90
  - Second method
    - Change the communication mode from Serial to Network by pressing "t", then "config interface", then press the interface button to toggle between serial, network, and none. Change it from serial to network and press "ok".
    - Use a TCP client to open a communication command line.
    - Click "connect" and issue the following commands:
      - dcpl1:4
      - dcpl2:4
      - dcpl3:4
    - Change the communication mode back to serial.

Note: why did we do this? Because mot1-3 have 400 steps per degree (that's 0.0025 degrees per step).

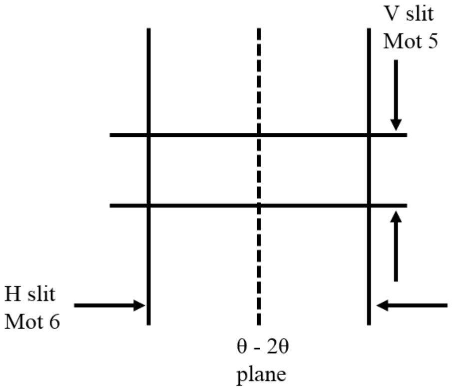

- Park position:
  - 2-Theta (mot 1): 0
  - Omega (mot 2): 0
  - Chi (mot 3): 90
  - Phi (mot 4): 0
  - V slit: 2
  - H slit: 9

Analysis

Dioptas

- Open Dioptas located on Huber PC desktop.
- Click load file.
- Select MAR345 calibration image.
- Make sure rings look smooth, circular and concentric.
- Start values:
  - Distance: 200.0 mm (this will be refined)
  - Wavelength: 0.71073 A (Moly)
  - Polarization: 0.990

- Pixel width/height: MAR345 square pixel size depends upon selected detector mode (resolution):

File Type	**Image diameter (mm)**	**Pixel size (µm)**
2300	345	150
2000	300	150
1600	240	150
1200	180	150
3450	345	100
3000	300	100
2400	240	100
1800	180	100

- Calibrant: LaB_6

- Deselect automatic increase.
- Select single peak search.
- Click on multiple points (~ 8) around the rings beginning with the central ring and working outwards.
- Be sure to increase current ring number as you move from ring to ring.
- Select a minimum of 5 rings.
- Leave other settings as default.
- Click calibrate.

- Make sure lines in cake image are straight. If they are wavy calibration failed. Try to recalibrate selecting more points on the rings.
- When image is good click save calibration and record calibrated parameters!!
- Refined detector distance should be approximately 215 mm. Give or a take a few millimeters.
- Saved file will have extension .poni

GSEADA

GSEADA is used to analyze single crystal images. Note: Do not use while Single is running. No multitasking!

- Open GSEADA on Huber PC desktop.
- Select MAR345 images.
- Open the first image of the collected set.
- Open "Calibration" tab.
- Enter calibration parameters from Dioptas.
- Calculate XYZ and DetXY.
- Save the calibration.
- Select "Show rings" to make sure calibration is appropriate. Then deselect "Show rings".
- On "Scan" tab, enter scan parameters used for collection.
- Select "Merge step images".
- On "File" tab save merged image.
- On "Search" tab, select "PS" (peak search).

Note: Threshold may have to be adjusted but never use a number < 1.00. Box size may also have to be adjusted, 10 is good.

- Add necessary peaks manually.
    - Right click on image to zoom into area.
    - On “Zoom” tab right click to add peaks.
- Right click on image and select “Selections off”
- On “Peaks” tab select “Peak fit”
- Look through list of peaks, adjusting peaks that need to be adjusted and deleting peaks that cannot be fit.
- On “Peaks” tab save peak list.
- On “File” tab open the first image.
- On “Scan” tab select “Compute prof. from scan”.
- On “Peaks” tab save peak list.
- Open RSV.

RSV

RSV (Reciprocal Space Viewer) is used to refine lattice parameters from GSEADA output.

- Open RSV on Huber PC desktop.
- Open saved file from GSEADA.
- For hand rotation:
    - Click view tab.
        - Hand rotation.

    - Click to make anchor.
    - Right click to undo.
    - “0” button to go back to the origin.
- If points appear to outline the surface of a sphere (even if just a partial sphere) upon hand rotation then the calibration is most like bad.
- Click index tab.
- Click transform tab.
- Click Cellnow.
- Type: xxx.p4p, in terminal window then press enter
- Accept questions until “minimum and maximum allowed values for cell edge:”. Enter appropriate values.
- Accept the appropriate cell dimensions and save the .p4p file.
- Close Cellnow.
- Click index tab at top.
- Click file tab.
- Click Read from p4p
- Select .p4p file that was created using Cellnow.
- Click Select w/ UB.
- Click view tab.
- Click Delete selected.
- Click index tab at top.
- Click lower index tab.

- Click Recalc. UB.
- Click Reindex.
- Repeat clicking Recalc. UB and Reindex a few times.
- Record UB matrix as well as unit cell parameters.

Troubleshooting

Huber

- Power supply won't turn on :
    - Check orange X-ray caution light bulb has not burnt out.
    - Check power supply front button (Control Power On, X-ray On, X-ray Off) lights are not burnt out.
    - Double check interlock flow meters.
    - Double check key is turned.

- Power suddenly is lost while X-rays are powered up :
    - Before turning X-rays back on press and hold X-ray off button on power supply to view set current and voltage. Adjust current and voltage back down to 8.0 mA and 15 kV before pressing X-ray on.
- Shutter will not open :
    - Double check door is closed.
    - Double check interlocks are enabled.
- SMC controller

  - In rare occasions one may need to lookup commands for the smc unit. There is a bookmark in Fire Fox but in general go to www.pp-electronic.de/files/smc/doc-html/index.htm. Login credentials: name: user pw: smc, No capitals!

MAR Control

- Shutter does not open when button is clicked :
  - Double check interlocks are enabled.
  - Double check a TCP dialogue has not been opened in the terminal.
  - Make sure SMC9300 is in network mode.
  - Make sure interlocks are set to "Huber" and not "Manual"
  - Computer may need a moment.
- Communications error mot 4 took too long :
  - Make sure SMC9300 is in network mode.
  - MAR Control only allows approximately 10 seconds for phi to reach its destination. This ensures the controller will not continue to drive phi if it jams on its travel. Sometimes the SMC9300 decides to take phi the long way around and takes too long for MAR Control. Simply restart collection.
- MAR IP cannot connect to detector or internet :
  - Periodically, if MAR IP is rebooted it fails to load the ethernet ports correctly resulting in a failure to communicate with the MAR345 and the internet. Restart the computer. This may take several attempts (the hardware is old).

Water Chiller

- If high pitched noise, higher than usual, is heard emanating from the hutch check the temperature of the water chiller. If temperature is higher than ~25°C the water supply is most likely too warm due to a main chiller failure or shutdown. Immediately begin to shut down the X-rays. Notify F.M. and Steve, this is a plumbing emergency.

Miscellaneous

- LX-57B radiation shielding lead glass tends to tarnish more readily than ordinary window glass. Note the following points:
    - Wipe off smudges on the LX-57B with a dry clean cloth (ex. Gauze).
    - Wipe fingerprints off the LX-57B immediately with a dry, clean cloth.
    - Smudges not removed by wiping with a dry cloth should be cleaned with alcohol.
    - Window must be completely dry.

- Diffractometer axes:

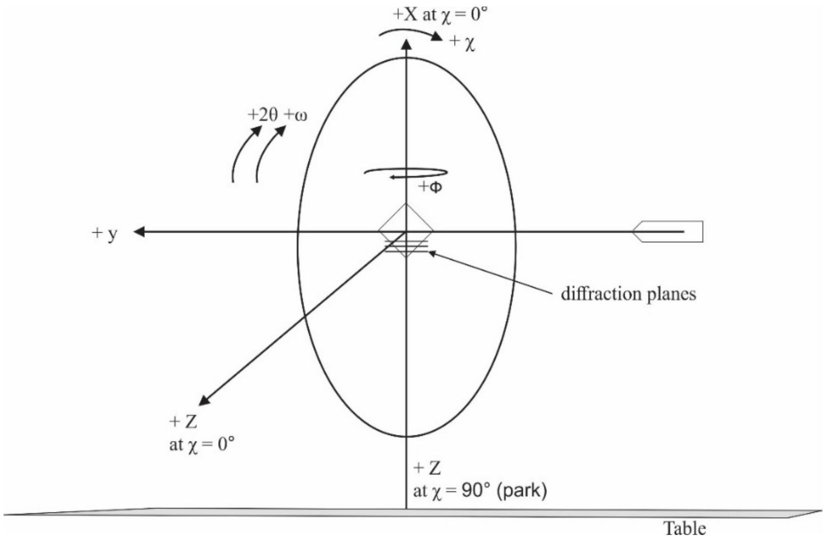

- This standard operating procedure electronic version is on the Huber desktop in the desktop icon labeled box sync. File location is Box Sync/X-Ray/Manuals/Huber-SOP-most current date (format of date is year, month, day). Note there is also a link in Google Chrome to that Box drive.

Appendix C

Table c.1: Bill of materials for MAR345 linear rail system. Product numbers from Item USA, all parts in metric units.

Part	Quantity
Linear Guide Carriage Unit 8 D14 120x40 // Product No.: 0.0.629.19	2
Profile 8 40x40x270, natural // Product No.: 0.0.026.03	4
Profile 8 40x40x279, natural // Product No.: 0.0.026.03	3
Profile 8 40x40x1065, natural // Product No.: 0.0.026.03	2
Profile 8 40x40x985, natural // Product No.: 0.0.026.03	2
Profile 8 80x40x359, natural // Product No.: 0.0.026.04	1
Shaft-Clamp Profile 8 D14x1065, natural // Product No.: 0.0.294.34	2
Shaft D14x1065, bright // Product No.: 0.0.294.01	2
Cap 8 40x40, black // Product No.: 0.0.026.01	4
Cap 8 80x40, black // Product No.: 0.0.026.02	2
MAR345 Adapter Plate	1
M4x10 Socket Head Cap Screw	4

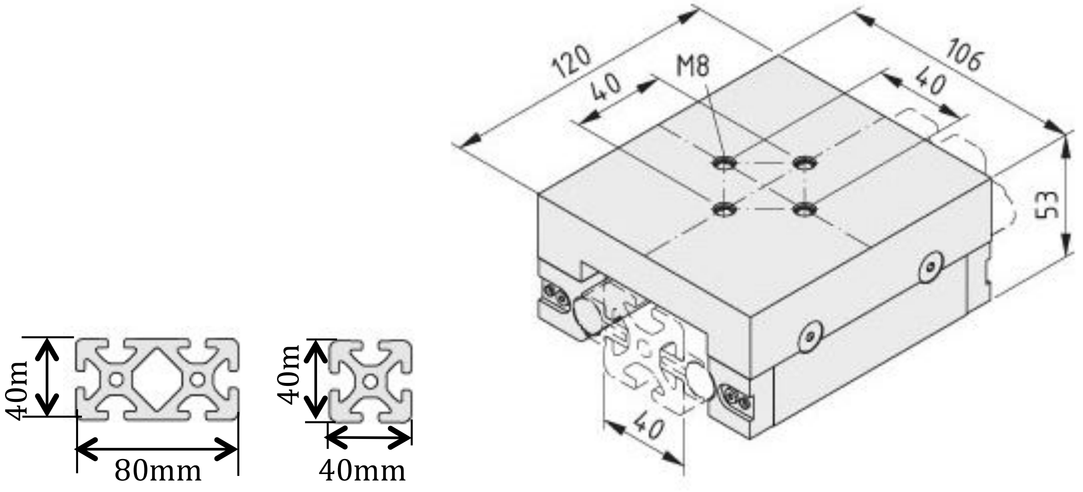

Figure c.1: Diagrams of MAR345 linear rail system rails and linear slides. All units in millimeters.